TECHNISCHE UNIVERSITÄT WIEN
Vienna | Austria

DIPLOMA THESIS

Experimental Investigations of Thermo-Catalytic Methane Pyrolysis in a Fluidised Bed Reactor

carried out for the purpose of obtaining the degree of Dipl.Ing.,
submitted at TU Wien, Faculty of Mechanical and Industrial Engineering, by

Martin Jakob Hauser
Mat.Nr. 01526813
[redacted]

under the direction of
Univ.Prof.i.R. Dipl.-Ing. Dr.techn. Hermann Hofbauer
under the supervision of
Projektass. Dipl.-Ing. Dr.techn. Josef Fuchs

Institute of Chemical, Environmental and Bioscience Engineering

Vienna, 24.01.2022

I confirm, that going to press of this thesis needs the confirmation of the examination committee.

Affidavit

I declare in lieu of oath, that I wrote this thesis and performed the associated research myself, using only literature cited in this volume. If text passages from sources are used literally, they are marked as such.

I confirm that this work is original and has not been submitted elsewhere for any examination, nor is it currently under consideration for a thesis elsewhere.

I acknowledge that the submitted work will be checked electronically-technically using suitable and state-of-the-art means (plagiarism detection software). On the one hand, this ensures that the submitted work was prepared according to the high-quality standards within the applicable rules to ensure good scientific practice "Code of Conduct" at the TU Wien. On the other hand, a comparison with other student theses avoids violations of my personal copyright.

Vienna, 24.01.2022

Martin Hauser

Acknowledgements

First and foremost, I have to thank my main advisor Univ.Prof.i.R. Dipl.-Ing. Dr.techn. Hermann Hofbauer for making this thesis possible. Special appreciation is given to my co-advisor Projektass. Dipl.-Ing. Dr.techn. Josef Fuchs for his assistance and dedicated involvement in planning, structuring, and organising every step throughout the process. Thank you very much for your professional support.

I would like to give particular gratitude to Martin Kutter, MA, for his valuable input and proofreading of this thesis. The way you offered your help can be taken all but granted. Your personal encouragement and professional assistance have been invaluable. Thank you.

Writing this thesis required assistance from a lot of people. In this manner I want to give a special thank you to Dr. Annette Schnettelker and Dipl.-Ing. Valentin Hanser who always had an open ear when I had doubts or questions.

Coming so far, I must express my gratitude to so many more. Especially to my fellow students and dear friends with whom I have spent days and nights the past years. You made the long hours of studying so much more enjoyable and you are the reason for countless memorable evenings. Thank you for an incredible time.

Finally, my upmost gratefulness goes to my family. Your unconditional support and continuous encouragement throughout my studies were priceless. This accomplishment would not have been possible without your help. Thank you, a lot, for everything.

Abstract

Current state of the art hydrogen production is performed by steam methane reforming. This process emits vast amounts of climate damaging carbon dioxide and is therefore not suitable for future applications, or – at the least – necessitates the use of a carbon capture and storage unit. Electrolysis as a renewable way for hydrogen production requires renewable electricity and is not yet ready for the production of hydrogen in large-scale. Decomposition of methane or natural gas is an alternative form of hydrogen production without emission of carbon dioxide and without massive energy requirements. After presenting a theoretical overview of the subject, this thesis studies the catalytic decomposition of methane in a small-scale fluidised bed reactor. Various bed materials were employed: Limestone, Activated carbon, Ilmenite, and Iron. Deactivation of the bed material showed to be problematic especially using limestone and activated carbon. Activated carbon was treated with CO_2 and steam, respectively, to regain its activity. The downsides were additional energy requirements and carbon emissions. Carbon deposits on iron exhibited self-catalytic properties and high conversion rates. Thus, iron can be seen as most promising candidate for the thermo-catalytic decomposition of methane.

Kurzfassung

Der überwiegende Teil des heutzutage industriell eingesetzten Wasserstoffs wird über die Methandampfreformierung erzeugt. Bei diesem Verfahren werden große Mengen an klimaschädlichem Kohlendioxid freigesetzt, sodass es für künftige Anwendungen ungeeignet ist oder zumindest eine Anlage zur Abscheidung und Speicherung von Kohlendioxid erforderlich macht. Die Elektrolyse als erneuerbare Methode zur Wasserstofferzeugung erfordert große Mengen an Energie, die derzeit nicht vollständig erneuerbar erzeugt werden können. Die Zersetzung von Methan oder Erdgas ist eine alternative Form der Wasserstofferzeugung ohne Emission von Kohlendioxid und ohne massiven Energiebedarf. Nach einem theoretischen Überblick über die Thematik wird in dieser Arbeit die katalytische Zersetzung von Methan in einem Wirbelschichtreaktor in kleinem Maßstab untersucht. Es wurden verschiedene Bettmaterialien verwendet: Kalkstein, Aktivkohle, Ilmenit und Eisen. Die Deaktivierung des Bettmaterials erwies sich insbesondere bei Kalkstein und Aktivkohle als problematisch. Aktivkohle wurde mit CO_2 bzw. Dampf behandelt, um ihre Aktivität wiederzuerlangen. Nachteilig waren der zusätzliche Energiebedarf und die Kohlenstoffemissionen. Kohlenstoffablagerungen auf Eisen wiesen selbstkatalytische Eigenschaften und hohe Methanumsätze auf. Zusammenfassend kann gesagt werden, dass Eisen als Katalysator somit die vielversprechendsten Eigenschaften aufweist.

Table of contents

1 Introduction

1.1 Motivation

Currently, most of the world's primary energy consumption comes from fossil fuels and the demand is further increasing. Fossil fuels emit vast amounts of carbon dioxide which boost the climate crisis. It is therefore absolutely necessary to shift to a carbon neutral energy system in the medium run. Hydrogen can substitute the combustion of fossil fuels in industry, transport, and other sectors. Buzz words and initiatives such as 'hydrogen economy' and the 'European Green Deal' demonstrate that hydrogen production, storage, and utilisation have received increasing attention over the past years.

There are several methods to produce hydrogen. Most of these processes use fossil feedstock. A relative majority of 48% of hydrogen is produced from natural gas (NG), 30% from petroleum and 18% from coal. The remaining 4% come from electrolysis of water (Ashik, Wan Daud, & Abbas, 2015). Steam reforming of methane is the most common production method, followed by partial oxidation and coal gasification. All of them emit substantial amounts of CO_2 and should thus be substituted with cleaner technologies in the near future. These alternative approaches and methods include – among others – electrolysis and methane pyrolysis. Water electrolysis is a very energy consuming process requiring lots of electricity from renewable sources to guarantee carbon-emission free hydrogen production. Methane pyrolysis, on the other hand, has comparable energy requirements to existing technologies and uses a readily available, albeit non-renewable, feedstock. Therefore, it appears to be the best solution in the medium run.

The motivation for this thesis is thus the to explore the substitution of CO_2 emitting hydrogen production technologies with a process with a significantly improved carbon balance. Methane pyrolysis uses a readily available feedstock, has a comparable energy input, and can be implemented at industrial scale in the medium term.

1.2 Aim & Scope

The practical work in this thesis is part of a pre-project for methane decomposition and subsequent utilisation of carbon. The results contribute to the decision-making process for upcoming development paths of large-scale R&D projects on national levels.

Utilising existing university infrastructure, thermo-catalytic decomposition of methane (TCD) is carried out in a laboratory-scale fluidised bed reactor. Various bed materials are examined with the ambition of creating a scalable process that can operate in a stable manner, has a reduced CO_2 footprint or is even carbon neutral, is economically feasible, produces allotropes of carbon that can be further utilised and enables the development of innovative applications of the produced carbon. Producing non-marketable

carbon for sequestration only is undesirable. Promising catalysts are identified and proposed for further investigation. The produced carbon is then characterised to gather information on possible carbon applications.

Summing up, the aim of this thesis is the process evaluation and development, and production and characterization of carbon samples.

1.3 Methodology of Thesis

The theoretical part of the thesis evaluates the science behind TCD as a whole. Methane pyrolysis is defined at first and different technologies to achieve the decomposition reaction are elucidated. A special focus is put on TCD in fluidised bed systems. Methane pyrolysis is scrutinised based on previous work by several authors, existing process technologies are examined and the benefits and disadvantages of using fluidised bed systems for TCD are analysed.

The practical part deals with the implementation of TCD in an existing small-scale fluidised bed system. Preparation of the reactor involved the removal of deposits that accumulated inside the reactor tube during previous experiments, verification of tightness, and fitting of heating shells and thermal insulation onto external surfaces. Catalysts were selected based on their global abundancy and results described in current research. The catalysts were classified, and the minimum fluidisation velocity was checked for the appropriate particle diameter range. The test run temperature was determined based on results in scientific sources.

Depending on catalysts characteristics and the number of test runs for said catalyst, the experiments were carried out with fixed parameters or with parameter variations. Variation of parameter variation was somewhat limited due to the minimum fluidisation velocity, sintering at high temperatures, overall temperature resistance of the system, and others, but included the variation of fluidisation velocity, reaction temperature and method of catalyst regeneration.

The composition of the flue gas, temperatures at various points of the system and the pressure loss was measured continuously. The recorded data was processed and is plotted and thoroughly discussed herein. Carbon samples were retrieved and weighed. The physical mass is compared to theoretically expected values. At the end, the results are evaluated, and a short outlook is given.

2 Methane Pyrolysis Reaction

Pyrolysis is generally defined as the thermal decomposition of substances into its constituents at elevated temperatures in an inert atmosphere. Accordingly, methane decomposes into a solid phase of elemental carbon and a gaseous phase of elemental hydrogen as in (i).

$$CH_4(g) \rightarrow C(s) + 2H_2(g) \qquad \Delta H_R^0 = +74{,}9\ kJ/mol \qquad (i)$$

It is proposed as an alternative route to produce hydrogen from NG without the emissions of carbon dioxide. The reaction is endothermic and starts at temperatures of 700 °C (Steinberg, 1999), with a complete conversion expected above 1350 °C (Abánades, Ruiz, Ferruelo, Hernández, Cabanillas, Martínez-Val, et al., 2011). A reasonable yield can be expected at temperatures above 1200 °C (Dagle, Dagle, Bearden, Holladay, Krause, & Ahmed, 2017). The high heat required for this process is a consequence of the strong C–H bonds (440 kJ/mol), making methane one of the most stable organic molecules (Muradov & Vezirolu, 2005). Comparably, lignocellulosic biomass pyrolyses in a temperature range of 160 – 900 °C, with the cellulosic constituents degrading below 400 °C (Yang, Yan, Chen, Lee, & Zheng, 2007). Longer residence times and higher temperatures favour a high methane conversion (Dunker, Kumar, & Mulawa, 2006).

The pyrolysis reaction is favoured by high temperatures and reduced pressures. I.e., the equilibrium of the reaction is further on the side of hydrogen and carbon in a hot and low-pressure environment. The influence of these two parameters is represented in Figure 1. One must consider that the equilibrium is hardly achievable without a catalyst or excessive residence times.

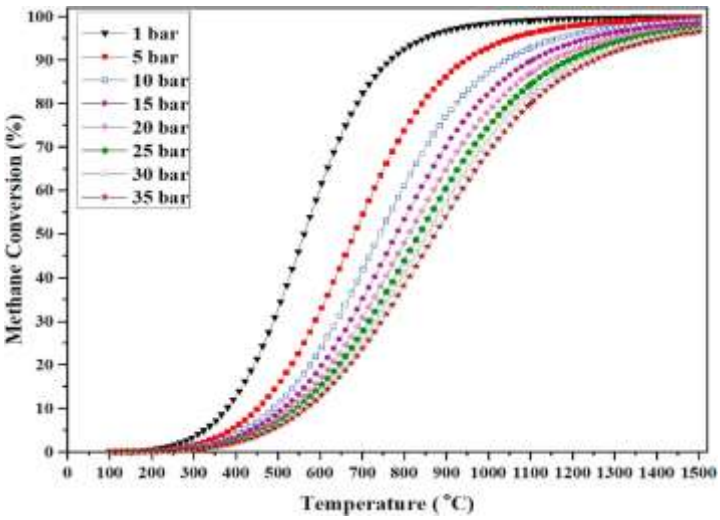

Figure 1: Equilibrium conversion of methane with temperature and pressure in Aspen Plus® v10. (Leal Pérez, Medrano Jiménez, Bhardwaj, Goetheer, van Sint Annaland, & Gallucci, 2021)

In economic studies, methane pyrolysis must compete with steam methane reforming, the current state of the art for hydrogen production from NG. In this endothermic process, steam is mixed with natural gas in a ratio of 2,5–3 and reformed at a temperature of 850–920 °C and a pressure of 25–35 bar

(Medrano, Palo, & Gallucci, 2020). In a first step, methane is transformed to syngas (a mixture of CO and H_2) according to (ii). Further hydrogen is subsequently produced via the water-gas shift reaction (iii). The combined reaction is then represented by (iv).

$$CH_4 + H_2O \rightleftharpoons CO + 3H_2 \qquad \Delta H_R^0 = +206{,}3\ kJ/mol \qquad (ii)$$

$$CO + H_2O \rightleftharpoons CO_2 + H_2 \qquad \Delta H_R^0 = -41{,}2\ kJ/mol \qquad (iii)$$

$$CH_4 + H_2O \rightarrow CO_2 + 4H_2 \qquad \Delta H_R^0 = +165{,}1\ kJ/mol \qquad (iv)$$

In the steam methane reforming process, each molecule of methane produces four molecules of hydrogen. Methane pyrolysis produces only half the amount of hydrogen for each molecule of methane. The theoretical energy input needed for the process is related to the reaction enthalpy. For steam methane reforming, that is 41,3 kJ/mol H_2, or 63 kJ/mol H_2 when considering the energy necessary to vaporise water. The environmentally friendly approach of water electrolysis exhibits a reaction enthalpy of 235 kJ/mol H_2, while the one for TCD is only 37,5 kJ/mol H_2 (Dagle et al., 2017). An energetic advantage is already apparent from this viewpoint, further expanding when taking into account additional energy requirements for carbon capture and storage in steam methane reforming processes, which will be imperative in a carbon neutral future. It is important to note that this quick analysis does not consider additional energy requirements in TCD systems, such as, among others, carbon separation or downstream hydrogen purification. Regarding the latter, Dagle et al. (2017) suggests that processing of the off-gas stream in TCD may be easier and less energy-intensive since no CO or CO_2 are present and the overall hydrogen concentration is higher.

This assessment does, however, have constraints. For the methane pyrolysis process, it does only examine the main reaction path, whereas further saturated and unsaturated hydrocarbon by-products are not considered. Moreover, steam methane reforming is operated at elevated pressures, while methane pyrolysis is predominantly carried out at atmospheric pressure (Schneider, Bajohr, Graf, & Kolb, 2020), thus requiring compression of the hydrogen. Process-specific losses of heat are also ignored. Therefore, and as an overall mature technology, steam methane reforming has a high energy efficiency and can produce hydrogen at a low cost.

The major drawback of steam methane reforming are the CO_2 emissions of the process. Methane pyrolysis does not have these emissions, provided the produced carbon is not burned in subsequent processes. There is also further potential to reduce capital and operating costs, as the off gas incorporates a considerably higher portion of hydrogen compared to steam methane reforming (Dagle et al., 2017). CO and CO_2 are not present altogether. Purification of the off-stream to produce commercial-grade H_2 should therefore require less effort (Dagle et al., 2017). Marketing of the carbon by-product can further reduce the cost. Putting a price on CO_2 – as is already done e.g. via the EU Emissions Trading System

– can make the methane pyrolysis process more economically feasible in competition with steam methane reforming.

Methane pyrolysis first emerged in the 1920s for the production of carbon black (Wang, Gray, Reznek, Mahmud, & Kutsovsky, 2003). In large-scale applications, it has thus far only been used in the carbon black industry to produce selected grades of carbon for tire and electrical component manufacturing, while hydrogen was only seen as a by-product (Dagle et al., 2017). The hydrogen was burned to generate the required process heat or used on adjacent facilities and sites. The first development towards hydrogen production was started in 1963 with the HYPRO process (Schneider et al., 2020). A laboratory scale unit was implemented with a CH_4 throughput of 7 m^3/h, but development was stopped. Moreover, the carbon was burned to generate the process heat, nullifying the potential benefit of generating a carbon-emission free hydrogen product.

2.1 Thermo-Catalytic Reaction

Non-catalytic methane pyrolysis requires high temperatures to be able to break the four C–H bonds. TCD significantly reduces the necessary temperature while maintaining a high yield and is thus an economic way to produce hydrogen. Ermakova, Ermakov, & Kuvshinov (2000) found that catalytic cracking can be performed at temperatures as low as 500 °C when using a nickel-based catalyst. The temperature at which TCD performs best depends heavily on the specific catalyst. Typical catalysts used in TCD include metal-based – both supported and non-supported – and carbonaceous materials, which will subsequently be discussed.

Many kinetic studies of carbon formation by TCD have been done in the past (Snoeck, Froment, & Fowles, 1997; Zadeh & Smith, 1998; Zavarukhin & Kuvshinov, 2004; Zhang & Smith, 2005) Through those, it is now generally agreed that the mechanism follows five steps (Ashik et al., 2015; Sánchez-Bastardo, Schlögl, & Ruland, 2020; Suelves, Pinilla, Lázaro, Moliner, & Palacios, 2009; Zavarukhin & Kuvshinov, 2004; Zhang & Smith, 2005):

1) Chemisorption of methane on the surface of the catalyst
2) Dissociation of the chemisorbed methane into a methyl-radical and a hydrogen atom

$$CH_4 \cdot \rightarrow CH_3 \cdot + H \cdot \qquad (v)$$

Followed by the progressive breaking of the remaining C–H bonds to create elemental carbon and hydrogen

$$CH_3 \cdot \rightarrow CH_2 \cdot + H \cdot \qquad (vi)$$

$$CH_2 \cdot \rightarrow CH \cdot + H \cdot \qquad (vii)$$

$$CH \cdot \rightarrow C \cdot + H \cdot \qquad (viii)$$

3) Aggregation of the atomic hydrogen into molecules and gas phase emission

$$2H \cdot \rightarrow H_2 \qquad (ix)$$

4) Aggregation of atomic carbon into encapsulated carbon, causing progressive deactivation of the catalyst; or atomic carbon diffusion through the catalyst, driven by the concentration and/or temperature gradient
5) Nucleation of carbon followed by formation and growth of carbon deposits in the trailing face of the catalyst particles

The major problem in TCD is the deactivation of the catalyst, which usually necessitates a regeneration step that can – depending on the process – lead to CO_x emissions (Ashik et al., 2015). Another challenge is unreacted methane and other components in the off stream, that thus requires purification.

2.1.1 Metal Catalysts

Numerous metals exhibit catalytic activities in methane pyrolysis, with transition metals having shown the most promising results (Msheik, Rodat, & Abanades, 2021). Metals can be applied in their unsupported state or on catalyst supports and promoters. These artifacts can influence the activity and longevity of the catalyst as well as the structure and morphology of the formed carbon (Ashik et al., 2015).

Non-supported Metals

Nickel, cobalt, and iron were studied extensively due to their relative abundance and lower cost compared to noble metals (Msheik et al., 2021). It was found that in their non-supported state, the activity of these metals was in the order of Ni > Co > Fe (Avdeeva, Reshetenko, Ismagilov, & Likholobov, 2002). These metals exhibit the best performance of all transition metals since their 3d orbitals are only partially filled, enabling them to accept electrons, and thus promoting the dissociation of the hydrocarbons (Ashik et al., 2015; Chen, Qi, Zhang, Su, & Somorjai, 2020; Msheik et al., 2021; Sánchez-Bastardo et al., 2020).

Nickel-based catalysts deactivate rapidly at temperatures above 600 °C due to carbon encapsulating active sites (Chesnokov & Chichkan, 2009). I.e. at this temperature, the speed of carbon deposition on the catalyst surface exceeds the diffusion rate through the bulk metal, resulting in excessive carbon precipitating on the leading face (Amin, Croiset, & Epling, 2011; Msheik et al., 2021). Ermakova et al. (2000) found that stable operation of nickel catalysts with an acceptable hydrogen yield can only be observed between 500 and 550 °C. Below that temperature, the conversion rate is significantly reduced through the thermodynamic equilibrium being far on the educt side.

Cobalt and nickel both have toxicity issues, exacerbating the marketing of the – contaminated – carbon by-product (Sánchez-Bastardo et al., 2020). It also aggravates the permanent storage of the so-formed carbon (Msheik et al., 2021). The high cost of these materials compared to iron reduces their attractiveness further (Amin et al., 2011; Qian, Chen, Enakonda, Da Liu, Basset, & Zhou, 2020). Thus, the focus in recent years was on safer and cheaper catalysts, such as iron-based materials (Sánchez-Bastardo et al., 2020).

Apart from the aforementioned benefits, iron-based catalysts offer a higher resilience against deactivation and a better stability at high temperatures (Msheik et al., 2021). The authors attribute that to low carbon solubility in iron and the high diffusion of carbon through the bulk metal. Methane pyrolysis performed on iron catalysts form an Fe_3C (cementite) intermediate, which – being unstable at elevated temperatures (Ermakova, Ermakov, Chuvilin, & Kuvshinov, 2001) – further decomposes to filamentous graphitised carbon and α-iron (Ahmed, Aitani, Rahman, Al-Dawood, & Al-Muhaish, 2009; Pinilla, Utrilla, Lázaro, Moliner, Suelves, & García, 2011). The α-iron exhibits catalytic activity for hydrocarbon cracking.

Supported and Promoted Metals

Metal supports gained a lot of attention in past research as they can significantly increase the activity and longevity of the catalyst (Msheik et al., 2021). The most common supports that were employed are metal oxides such as Al_2O_3, NiO_2, SiO_2, TiO_2, MgO, among others. A strong metal–support interaction is crucial to increase dispersion of the metal particles on the support, obviating the risk of agglomeration or sintering of the metal particles (Sánchez-Bastardo et al., 2020). Nevertheless, a very strong interaction can lead to the formation of hardly-reducible metal–support species, and therefore negatively affect the performance of the catalyst by hindering the formation of metallic active sites.

Transition metals can be promoted by other metals – e.g. Pt, Rh, Pd, Cu – to improve their thermal stability and their capability to accumulate carbon (Ahmed et al., 2009). Usually, the catalyst and metal dopant form an alloy, offering a higher surface area and providing more active sites (Msheik et al., 2021). Hence, catalyst promoters enhance the access and diffusion of the carbon by-product through the bulk metal. Consequently, the formation of encapsulating carbon on the active sites is avoided and the lifetime of the catalyst is prolonged (Sánchez-Bastardo et al., 2020). Metal promoters can also improve the dispersion of the catalyst on the catalyst support and increase reducibility of the metal–support species.

Carbon Nanotube and Nanofiber Formation

Transition metals as catalysts in both their supported and unsupported state are ideal for carbon nanotube or carbon nanofiber formation via a metal carbide intermediate (Ahmed et al., 2009; Msheik et al., 2021). The nanotube formation process was described in detail by Ermakova et al. (2001) as depicted in

Figure 2 in the case of an iron catalyst: The decomposition of the iron carbide is followed by the supersaturation of the catalyst particle with carbon. This results in the formation of a nucleus at the trailing face of the particle (Figure 2a), or – in the case of supported catalysts – at the metal–support interface (Amin et al., 2011; Kock, De Bokx, Boellaard, Klop, & Geus, 1985). Ermakova et al. (2001) describe that other graphite crystals congregate around this nucleus (b). The alternative way of forming further nuclei is not favourable due to the high activation barrier it must overcome. The continuous loading of the catalyst particle with iron carbide through methane decomposition leads to the repetition of this "carbide cycle" (c). Once the attachment of multiple carbon layers in parallel to the particle surface has taken place (d), the particle extends its tail (e), disorienting the graphite layers into a hollow structure (f) – eventually forming a carbon nanotube. Further growth of the nanotube leads to a narrowing area at the part in contact with the particle (g). The tail of the catalyst particle is often pulled inside the graphitic capsule and cut off from the bulk through further narrowing of the neck of the nanotube (h). At this stage, the contact area between particle and carbon becomes too small to precipitate graphite at the same rate as carbon is dissolved in the metal, leading to deposition of the extra carbon at adjacent sites around the neck, ultimately forming the next nanotube.

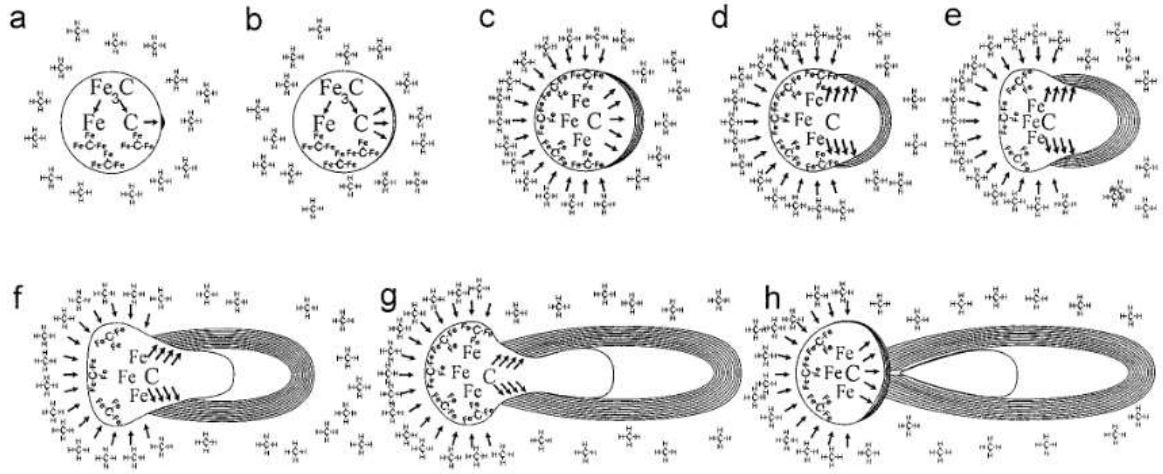

Figure 2: Stages of nucleation and growth of carbon filaments on iron catalysts (Ermakova et al., 2001)

In the case of supported catalysts, the catalytically active metal detaches from the support after nucleation (Amin et al., 2011). It is also stated that at this point, the support can no longer act as a heat sink. Consequently, the temperature of the particle increases moderately, determining a faster growth rate.

Metal Catalyst Deactivation

The biggest challenge in TCD processes is the deactivation of the catalyst. There are many mechanisms that negatively influence the performance of metal catalysts, such as coking, poisoning, mechanical degradation, and sintering (Ashik et al., 2015). It is commonly agreed that the primary reason for deactivation of catalysts in TCD is coking (Amin et al., 2011), i.e. carbon formation and deposition on

the catalyst's active sites. Amin et al. (2011) have identified several aspects that affect the catalytic activity either individually or in combination. The carbon can deactivate the catalyst by: (i) strongly adsorbing on the active phase surrounding and blocking access to the active sites; (ii) encapsulating the active metal particle; (iii) plugging the micro- and mesopores, thus inhibiting access to the active sites inside the pores; (iv) accumulating as strong carbon filaments leading to the disintegration of catalyst pellets; and (v) physically blocking the reactor in extreme cases.

For any given catalyst exists an equilibrium between carbon production rate and carbon solubility and diffusion through the bulk metal (Msheik et al., 2021). If the reaction rate exceeds this point, diffusion cannot keep up and deactivation of the catalyst follows. Either way this is the case for a rise of the reaction temperature as well as of the flow rate. Zhang, Ge, & Xu (2011), Suelves et al. (2009) and Ermakova et al. (2000) used nickel-based catalysts to study the influence of temperature on the deactivation rate, showing that the catalyst deactivated more rapidly at elevated temperatures. The results by Ermakova et al. (2000) are represented in Figure 3. Zhang et al. (2011) state that under these conditions, the carbon nucleation rate is too high and diffusion through the bulk cannot keep up, ultimately causing carbon deposition on and around active sites. With carbon depositing on the catalyst interface, the heat transfer to the bulk metal decreases, slowing down the diffusion through the catalyst (Baker, 1972). This further boosts the catalyst deactivation. Suelves et al. (2009) further studied the influence of an increasing methane flow rate and found two clear effects: the hydrogen concentration in the off-gas diminishes, and the deactivation rate of the catalyst surges. They further state that although the overall higher flow rate reduces the hydrogen concentration in the outlet gas, the initial reaction rate still increases significantly. This fact can be well observed in Figure 4, where the hydrogen production rates in mmol per minute and gram catalyst are plotted against time. The total amount of carbon deposited per gram of catalyst, however, was still highest at the highest flow rate. In an earlier study by the same author (Suelves, Lazaro, Moliner, Corbella, & Palacios, 2005) they exposed 0,3 g of a nickel-based catalyst to methane at flow rates of 20 ml/min, 50 ml/min and 100 ml/min at a temperature of 700 °C and found that the amount of deposited carbon was highest in the 50 ml/min trial and lowest in the 100 ml/min trial. This indicates that at the highest flow rate, the diffusion of produced carbon could not keep up with the carbon nucleation rate and active sites were quickly blocked.

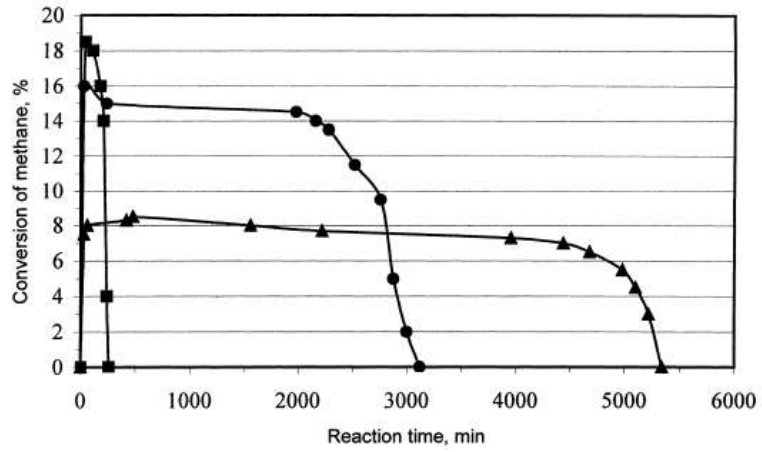

Figure 3: The global kinetics of methane decomposition over Sample 1 at 600 °C (squares), 550 °C (circles) and 500 °C (triangles) (Ermakova et al., 2000)

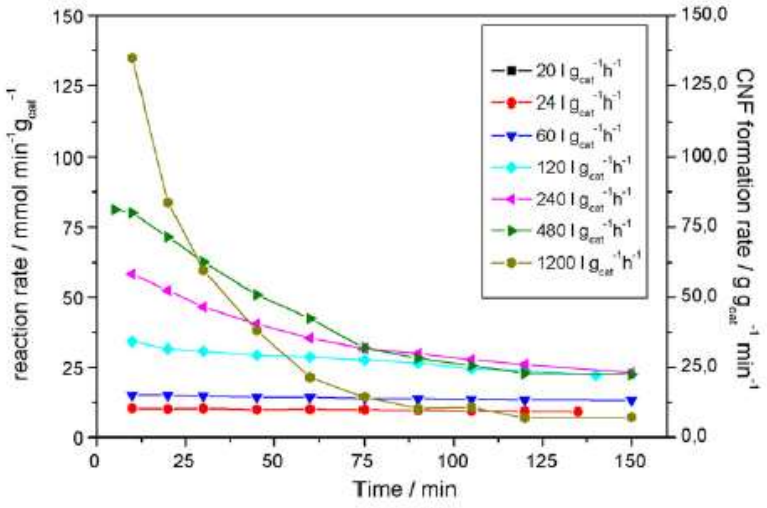

Figure 4: Influence of space velocity in the evolution of methane decomposition rate and carbon formation rate. T=700◦C (Suelves et al., 2009)

Metal Catalyst Regeneration

A major challenge when using metal catalysts for TCD is that, eventually, they deactivate (Amin et al., 2011). Regeneration is essential to recover most of their initial activity. Typically, carbon is removed by treatment with air (x), carbon dioxide (xi), or steam (xii)–(xiv), with air and steam being the most common techniques. The chemical reactions during treatment are as follows:

$$C + O_2 \rightarrow CO_2 \qquad \Delta H_R^0 = -393{,}7\ kJ/mol \qquad (x)$$

$$C + CO_2 \rightarrow 2CO \qquad \Delta H_R^0 = +172{,}5\ kJ/mol \qquad (xi)$$

$$C + H_2O \rightarrow CO + H_2 \qquad \Delta H_R^0 = +131{,}3\ kJ/mol \qquad (xii)$$

$$C + 2H_2O \rightarrow CO_2 + 2H_2 \qquad \Delta H_R^0 = +90{,}1\ kJ/mol \qquad (xiii)$$

$$CO + H_2O \rightarrow CO_2 + H_2 \qquad \Delta H_R^0 = -41{,}2\ kJ/mol \qquad (xiv)$$

From an energetic standpoint, using air is the most beneficial, requiring no external energy since the reaction is exothermal. Another thing to consider is the time it takes to regenerate the catalyst. Regeneration with air is typically the fastest, albeit the high temperatures generated during combustion have been reported to disintegrate the catalyst into a powder (Rahman, Croiset, & Hudgins, 2006; Zhang & Amiridis, 1998). This might be a result of carbon filaments growing inside the pores of the catalyst in the previous TCD cycle. To obviate the risk of disintegration, Rahman et al. (2006) proposed a partial gasification of the carbon. The theory they put forward says that: (i) the disintegration happens during filament growth, therefore complete oxidation will always lead to powder; and (ii) the deactivation is mainly due to encapsulating carbon; therefore, it is only necessary to oxidise this part of the carbon. As for the latter, it is said that encapsulating carbon has a different structure compared to the carbon forming the filament and is therefore the anterior portion to oxidise. Another problem that has been reported due to the high temperature generated in oxygen treatment is sintering of the metal and consequently the loss of activity (Villacampa, Royo, Romeo, Montoya, Del Angel, & Monzón, 2003).

Albeit requiring additional energy, using steam to regenerate the catalyst may be beneficial as it generates a more valuable product: hydrogen and carbon monoxide. Those can either be utilised the same way as syngas, or the additional hydrogen can be separated to improve the overall hydrogen output per amount of methane used. The former, however, has constraints as considerable amounts of CO_2 are generated as well (Amin et al., 2011). Zhang & Amiridis (1998) reported that in contrast to regeneration with air, steam gasification does not change the morphology of the catalyst, while still being able to recover most of the catalyst activity.

Despite their ability to restore catalyst activity almost completely, all methods have the drawback of producing substantial amounts of CO or CO_2. In the case of regeneration with air, the amount of CO_2 produced is almost comparable to that of steam reforming (Muradov, 2002). Therefore, regeneration of the catalyst by removal of the carbon through attrition has gained some attention (Abbas & Daud, 2010). However, attrition can only remove carbon on the external surface of the catalyst particles as depicted in Figure 5, which represents only a fraction of the total deposited carbon. In a study conducted by Jang & Cha (2007) they used an iron-based catalyst in a fluidised bed reactor and reported that the activity was maintained by attrition of the by-product carbon from the surface of the iron catalyst.

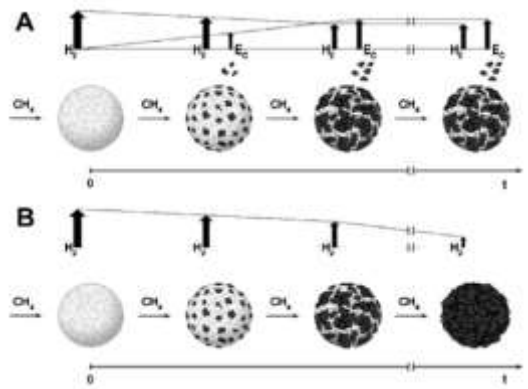

Figure 5: TCD on a catalyst particle. (A) Presence of attrition; (B) absence of attrition (Abbas & Daud, 2010).

2.1.2 Carbonaceous Catalysts

Carbon-based catalysts can be employed in the form of carbon black, activated carbon (AC), char and others. Depending on the kind used, several advantages showed: Citing Msheik et al. (2021) and Abbas & Daud (2010), these include low cost, resistance against elevated temperatures, safe storage, tolerance against impurities of sulphur, a contamination-free carbon by-product, self-catalytic effects of the produced carbon, little need for regeneration and avoidance of carbon dioxide emissions. Some authors, however, report a more limited range of advantages including only low cost, fuel flexibility, no sulphur poisoning and utility of the formed carbon as a catalyst precursor (Abbas & Daud, 2010).

Ashik et al. (2015) contemplate that the activity of carbonaceous catalyst is influenced by crystallinity, structural disorders, pore-size distribution, surface area and polar surface groups among others. Carbons with ordered structures such as graphite are catalytically less active than those with disordered structures such as AC, and carbon black (Muradov, 2001a). The activity of carbons ranks in the order of: amorphous > turbostratic > graphite (Muradov, Smith, & T-Raissi, 2005b). Carbon-based materials are influenced by surface properties such as defects, dislocations, vacancies, and low-coordination sites, all leading to high-energy sites which provide high catalytic activities (Msheik et al., 2021). Microporous AC has a low stability due to pore blocking as carbon deposits in the micro pores first (Ashik et al., 2015). Mesoporous AC with high surface area thus provides a better stability (Moliner, Suelves, Lazaro, & Moreno, 2005). It is generally agreed that a high surface area is beneficial for TCD (Lázaro, Pinilla, Suelves, & Moliner, 2008; Msheik et al., 2021; Muradov, Chen, & Smith, 2005a). The deactivation of carbonaceous catalysts can also mainly be attributed to a loss of surface area resulting from the filling of pores (Msheik et al., 2021; Muradov et al., 2005a). The presence of surface-active groups does slightly affect the activity of carbonaceous catalysts. Muradov et al. (2005b) studied the influence of oxygenated surface groups and concluded that they only marginally foster methane decomposition in the initial stages, while they dramatically increase the CO concentration in the effluent gas.

Carbon Catalyst Deactivation

Most studies focus on AC and carbon black as catalysts due to their higher activity and better stability. With comparable surface area, ACs generally offer a higher initial activity than carbon blacks, however, deactivation of ACs is rapid while carbon blacks are more stable (Muradov et al., 2005a).

The fast deactivation of AC can generally be attributed to pore blocking and the resulting loss of surface area (Ashik et al., 2015). I.e. a porous fresh catalyst is slowly transformed into a non-porous one. Suelves, Pinilla, Lázaro, & Moliner (2008) found a linear correlation between initial pore volume and quantity of carbon deposited. That means the pore volume determines the maximum carbon load of the catalyst before its deactivation and determines the amount of hydrogen produced per mass of catalyst. A study by Moliner et al. (2005) does not conform to this idea, however. The authors state that the catalyst deactivation mechanism does not only depend on the amount of carbon deposited but also on the experimental conditions. This conclusion was drawn when two experiments conducted with AC at 850 °C and 950 °C, respectively, revealed that deactivation at the lower temperature happens sooner. Hypothetically, this could mean the deposited carbon is more active in the latter case. They do, however, reject this hypothesis claiming that the convergence of methane conversion curves towards the end of their experiment does not support it. Instead, they could identify two other effects: a molecular sieve effect being associated with pore mouth blocking, where a decreasing size of the pore mouth makes the inner pore face inaccessible for methane adsorption; and an activated diffusion effect, in which higher temperatures lead to higher diffusion rates towards the pores and enhance carbon deposition on their surface.

Ashik et al. (2015) additionally propose that the deactivation might be a result of less active carbon depositing on the ACs and carbon blacks active sites. They state that the carbon by-product has a more well-ordered structure with a lower surface area due to carbon crystallite growth being energetically beneficial compared to carbon nuclei formation. The size of carbon crystallites depends on the reaction temperature (Muradov, 2002): high temperatures lead to small crystallites and vice versa, as elevated temperatures aid carbon nuclei formation. Also confirming carbonaceous catalysts deactivate slower at elevated temperatures. The fast growth of the crystallite leads to a pseudo-ordered (turbostratic) carbon and a loss of catalytic activity. These results conform to findings by Muradov et al. (2005b), in which the interlayer spacing of amorphous carbon and graphite was compared to the one of methane treated carbon black. Amorphous carbon exhibits an interlayer spacing of around 3,6 Å, graphite of 3,354 Å. The original carbon black does not have a stacked arrangement, but randomly oriented plates in respect to each other. After exposure to methane, an ordered stacking has evolved with an interlayer spacing of 3,4948 Å, a value between amorphous carbon and graphite, which is characteristic for turbostratic carbon.

Carbon Catalyst Regeneration

The low cost of carbon catalysts allows to omit regeneration altogether. However, it might still be beneficial in some cases. Activating agents such as CO_2, H_2O, air or O_2 can be used to regenerate carbonaceous catalysts (Abbas & Daud, 2010). The corresponding reactions are the same as in 2.1.

Muradov (2002) regenerated samples of AC that were used for TCD of methane at 850 °C over the course of 6 hours. The regeneration was carried out at 950 °C using air, CO_2, H_2O and a mixture of 50 vol% CO_2 and 50 vol% H_2O. Their findings are shown in Figure 6. Air exhibited a relatively low carbon activating activity, while an exposure to steam or a steam/CO_2 mixture significantly increased methane decomposition after regeneration.

In a similar study Muradov et al. (2005a) regenerated deactivated carbon catalysts using steam, CO_2 or a mixture of the two as activating agents. After exposing the catalyst to methane for one hour, it was regenerated over the course of 30 minutes. It showed that treatment of the catalyst could fully restore its original activity while gasifying only a fraction (15–20%) of the produced carbon.

Abbas & Daud (2009) carried out similar experiments where they exclusively used CO_2 to regenerate AC. A decomposition process for 30 min at 950 °C or 60 min at 850 °C was followed by gasification with CO_2 at 900 °C, 950 °C and 1000 °C, respectively, until the weight of the catalyst decreased to its previous level. They found the initial activity as well as the mass gain of the catalyst after each cycle decreased. They also reported the activity loss to be lower when the regeneration was carried out at higher temperatures.

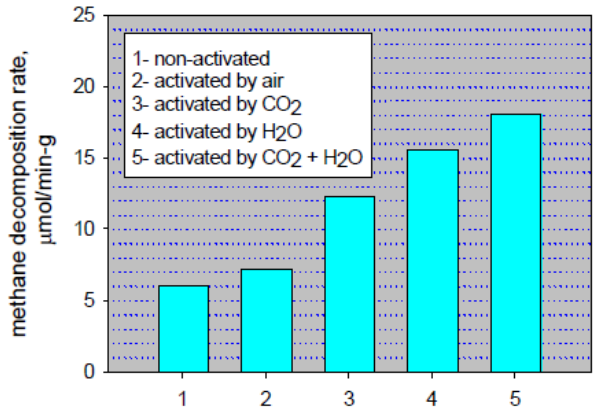

Figure 6: Effect of Carbon Catalyst Activation by Different Activating Agents on the Methane Decomposition Rate at 850 °C. Activation Temperature 950 °C (Muradov, 2002)

2.2 Reaction in Molten Media

The major challenge when using solid catalysts is their rapid deactivation. Employing molten media can avoid this problem (Chen et al., 2020; Fan, Weng, Zhou, Gu, & Xiao, 2021). Molten media can be employed as molten metals, molten metal alloys, and molten salts (Sánchez-Bastardo et al., 2020). Using

molten metals for TCD was first described in a patent by Tyrer (1931), where hydrogen was produced from methane in molten iron at temperatures of 1200 – 1300 °C. Generally, the decomposition reaction takes place inside – or rather, at the gas–liquid interface (Palmer, Tarazkar, Kristoffersen, Gelinas, Gordon, McFarland, et al., 2019) – of the formed bubbles which are injected at the bottom of the reactor and rising to the top (Geißler, Abánades, Heinzel, Mehravaran, Müller, Rathnam, et al., 2016; Sánchez-Bastardo et al., 2020). At the upper interface of the melt, they open up and release the carbon, hydrogen and remaining methane and intermediates. Carbon dissolving in the melt will reach saturation and subsequently precipitate at the top of the bath (Palmer et al., 2019). This way, every bubble will meet a clean liquid interface that is not affected by carbon deposition or encapsulation. Further advantages include: (near) zero carbon deposition on reactor walls (Geißler et al., 2016), an excellent heat transfer through the high heat capacity of molten metals and an enhanced residence time as a result of the liquid viscosity (Msheik et al., 2021). The low-density solid carbon floats atop the melt and can be removed continuously, allowing an uninterrupted operation of the whole process.

2.2.1 Molten Metals

Numerous metals and metal alloys were used in molten metal pyrolysis. Among them, Pt, Ti, Pb, Sn, as pure metals, and Ni-Bi, Cu-Bi, as alloys (Sánchez-Bastardo et al., 2020). Some metals – such as Pt, Pd, Ni – are active catalysts while other metals – such as Sn, Pb, Bi – do hardly influence the reaction (Upham, Agarwal, Khechfe, Snodgrass, Gordon, Metiu, et al., 2017). The active metals have a high melting point of over 1000 °C, while inert metals melt at much lower temperatures in the range of 200–700 °C (Msheik et al., 2021).

Metal contamination of the carbon by-product has shown to be problematic (Rahimi, Kang, Gelinas, Menon, Gordon, Metiu, et al., 2019). Marketing of a contaminated carbon by-product is difficult, purification is expensive and energy intensive, and some metals create issues due to their toxicity even for carbon storage (Msheik et al., 2021). Two sources of contamination were described in research papers. Msheik et al. (2021) ascribes the phenomenon to the high vapour pressure of some metals. At high temperatures, some of the metal will evaporate and accumulate in the headspace of the reactor. Upon saturation, the metal vapour will condensate in the pores of the carbon by-product and lead to contamination. Rahimi et al. (2019) on the other hand states that a metal film forms around the gas bubble. This film remains intact until the bubble reaches the surface and collapses. The resulting metal droplets contaminate the carbon as depicted in Figure 7(a).

2.2.2 Molten Salts

The contamination of the carbon by-product when using molten metals has led to increased attention of systems utilising molten salts. Different salts have been investigated, among them KBr, NaBr, NaCl, NaF, $MnCl_2$, KCl, or their mixtures (Kang, Rahimi, Gordon, Metiu, & McFarland, 2019; Sánchez-Bastardo et al., 2020). Albeit not necessarily creating contamination-free carbon, the post-processing is

much easier due to the high solubility of salts in water (Kang et al., 2019). Salts also exhibit a lower vapour pressure (Msheik et al., 2021). The densities of salts are similar to the one of solid carbon. Hence, depending on the exact system, the carbon will accumulate on the top or the bottom of the melt or be dispersed inside the liquid media (Kang et al., 2019). Another key property for the carbon–salt separation is the wettability (Rahimi et al., 2019). The wettability is determined by the contact angle at the three-phase boundary of the liquid, solid and gas. It is linked to the surface tension of the molten salt and the adhesion energy between solid carbon and molten salt. It can be described by the Young-Dupre equation (Cahn, Eustathopoulos, Nicholas, & Drevet, 1999). A high wettability hampers the separation of carbon from the salt melt. Experiments conducted by Rahimi et al. (2019) showed that molten NaBr with a wettability of 61 mJ/m² and a density of ~2,0–2,2 g/cm³ could achieve sufficient separation while the carbon stayed partially dispersed in molten KBr due to its higher wettability of 113 mJ/m² and lower density of ~1,9 g/cm³.

2.2.3 Combination of Molten Metals and Molten Salts

Opposed to molten salts, molten metals have the advantage of offering a much higher density than black carbon, allowing the carbon produced from TCD to float on top of the metal bath (Abánades, Rubbia, & Salmieri, 2013). On the other hand, contamination of the carbon product when using molten metals alone has shown to be problematic (Figure 7a) (Rahimi et al., 2019). Rahimi et al. (2019) combined various molten salts and metal ($Ni_{0,27}Bi_{0,73}$) with the salt floating atop the metallic melt. The experiment was conducted at a temperature of 1000 °C and different lengths of the salt phase were tested. The combination showed various advantages: the metal vapour in the headspace was reduced as metal vapour condenses inside the salt phase and sinks back to the metal melt; the carbon by-product was significantly purified through the salt phase. The level of remaining contamination varied depending on the height of the salt bath, with a higher salt melt reducing the number of contaminants. Less than 5% of metal in the carbon could be achieved in the two-phase system compared to 83% in the system with metal alone. With subsequent purification, metal contamination could be further reduced to undetectable levels.

The removal of contaminants by the two-phase system was described by Rahimi et al. (2019) to work as follows and as depicted in Figure 7b. The gas bubbles encompassing the hydrocarbon gas and pyrolysis products, a carbon diffusion layer, and a liquid metal film rise to the metal–salt interface. The metal film ruptures in the salt phase and metal droplets return to the metallic melt. Condensed carbon stripped from the bubble disperses in the salt phase. Ideally, the density of the carbon particles is smaller than the density of the salt, which can therefore rise to the top. The carbon within the bubble that was contaminated in the metal bath can evaporate off metal. The metal vapour condenses on the salt wall and sinks back to the metal melt.

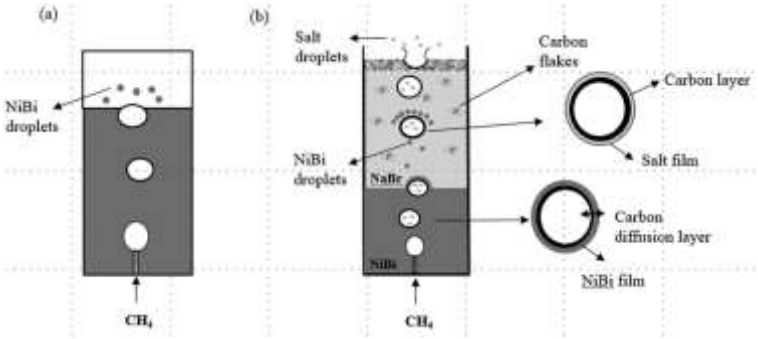

Figure 7: Schematic diagrams of bubbles passing through molten NiBi and NiBi/NaBr bubble columns. (a) Bottom-flow CH4 without a salt cap, and (b) bottom-flow CH4 with the NaBr salt cap (Rahimi et al., 2019)

2.3 Reaction in Plasma

Exposure to an electrical discharge is able to decompose hydrocarbons into its constituents. Plasma technologies have attracted increasing attention as they offer several advantages (Bromberg, Cohn, Rabinovich, O'Brie, & Hochgreb, 1998; Chaubey, Sahu, James, & Maity, 2013): the process is flexible regarding the hydrocarbon feedstock and is not limited to NG alone; it is a compact and light-weight system as a result of the high energy density; response time is quick, amounting to a fraction of second; high conversion efficiencies can be achieved; no catalyst is required, thus problems with catalyst deactivation are avoided; the capital costs are low considering simple carbon or metallic electrodes and simple power supplies can be used.

Plasma reforming requires near atmospheric pressures. It is difficult to operate at elevated pressures as it facilitates electrode erosion and shorten their lifetime (Bromberg et al., 1998). The method can be applied in a wide temperature range from below 700 °C as non-thermal plasma (Dagle et al., 2017), and up to 10.000 °C as thermal plasma (Muradov, 2017).

2.3.1 Thermal Plasma

In thermal plasma systems, a temperature higher than 700 °C is required (Dagle et al., 2017). Most of the time, these systems are operated at temperatures up to 2000 °C (Schneider et al., 2020), although temperatures as high as 10.000 °C are easily achievable (Ahmed et al., 2009). The activation energy is supplied through arc or inductively coupled discharges (Ahmed et al., 2009). The decomposition reaction is both electron-induced and a thermo-chemical reaction, controlled by the equilibrium condition (Lee, 2015; Tao, Bai, Li, Long, Shang, Yin, et al., 2011). Contrary to non-thermal plasma, the particles are of uniform temperature since the neutral species and the electrons interact longer than microseconds (Ahmed et al., 2009). Using external electric power to heat the feedstock and maintain this high temperature makes the process very energy intensive. Thermal losses further decrease the energy efficiency compared to other hydrogen production technologies (Dagle et al., 2017). An example is given in 2.4: the Seaport-plant by Monolith Materials that works similar to the Kvaerner process has an electrical energy input of 0,85 MW for an NG feed of 144 m³/h to achieve a methane conversion of

94% at a temperature of 2100 °C (Schneider et al., 2020). That means the process requires 526,7 kJ/mol NG, or 263,35 kJ/mol H_2. The high heat further necessitates the cooling of the electrodes to increase their durability and reduce thermal evaporation and ion-impact erosion (Ahmed et al., 2009).

2.3.2 Non-Thermal Plasma

Non-thermal plasma accelerates the decomposition process at low temperatures through the generation of active species (electrons, radicals, ions) by high-energy electrons (Ahmed et al., 2009; Lee, 2015). The active species initiates chemical reactions at a much lower temperature compared to thermal plasma. Consequently, the energy-input is much lower in this case. The temperature of the particles in non-thermal plasma varies and a low density of high-energy electrons in the system prevails (Lee, 2015).

The yield of H_2 has been said to be lower compared to thermal plasma systems due to the inhomogeneous discharge and the resulting limited reaction area (Dagle et al., 2017; Tao et al., 2011). Hence, some authors studied the combination of the non-thermal plasma process with a catalyst. The catalyst bed can be placed upstream or downstream the plasma zone; the catalyst can also be coated directly onto the electrodes or constructed within the discharge region (Chaubey et al., 2013).

Bromberg, Cohn, Rabinovich, & Alexeev (2001) performed methane decomposition in a low current plasmatron and found that non-thermal plasma could attain comparable yields to thermal plasma when combining the process with a metallic catalyst. Cho, Lee, Ju, Baek, & Lee (2004) reported a significantly increased hydrogen yield using catalysts. The authors employed a microwave plasma system with a honeycomb catalyst from Pd and Pt placed in the middle of the reactor. The plasma power was 3 kW, and the flow rate was set to 3 l/min at a pressure of 300 Torr (0,4 bar). The conversion efficiency increased from <10% in the case of no catalyst to 40% with a Pd-catalyst and >55% with a Pt-catalyst. It was further reported that increasing the Pt-loading could additionally boost the hydrogen yield.

Reports by other authors found that catalysts do not necessarily foster the decomposition in non-thermal plasma. Wang & Xu (2003) carried out a cold plasma reaction catalysed by LaBaO, ZnO, $La_{0,8}Sr_{0,2}CrO_3$, MoO_3/ZSM-5 (Zeolite Socony Mobil-5, an aluminosilicate zeolite), and V_2O_5, respectively. They found that only V_2O_5 could slightly catalyse the reaction, while the others had no or even a negative effect. Konno, Onoe, Takiguchi, & Yamaguchi (2013) treated methane in a microwave plasma environment with and without a Fe/Si-catalyst. The methane conversion slightly increased with the catalyst, but the difference was – at 3 pp – minor.

It can be concluded that the influence of a catalyst heavily depends on the type of catalyst used and the operating conditions.

So far, non-thermal plasma processes were only applied in laboratory scale (Harp, 2019). There is still significant research needed to upscale the process.

2.4 Existing Processes

In recent years, multiple start-ups and small-sized companies started researching methane pyrolysis. Solid catalysts, molten media, or plasma processes were put to work. Scrutinising the totality of the more or less commercial approaches is not expedient and goes beyond the scope of this paper. The following chapter elaborates the pioneers in the decomposition of methane as well as a few of the most advanced concepts of recent projects.

2.4.1 HYPRO, United Oil Products Company

US-based United Oil Products company filed a patent for their HYPRO process (Pohlenz & Scott, 1963), presenting a dual fluidised bed reactor for the production of hydrogen using a Al_2O_3 supported Ni–Fe–Co catalyst (Abánades et al., 2013). The patent (Pohlenz & Scott, 1963) describes a continuous process comprising a reaction zone and a regeneration reactor as depicted in Figure 8. In the former, catalyst moves from top to bottom counter currently to the flow of hydrocarbon gas, being decomposed at temperatures of 815–1100 °C. Deactivated catalyst is subsequently transferred into the regeneration zone, where carbon is oxidised with air. Preferably, oxidising conditions are controlled in a way that preclude both excessive burning of the carbon and oxidation of the catalyst and provide a carbon monoxide rich gas stream. Oxidation of carbon is exothermic, therefore heating the catalyst particles. These subsequently act as a heat carrier, supplying the necessary energy for the pyrolysis reaction. The flow rate in this part of the system is high enough for the catalyst particles to be entrained in the gas flow. At the top of the regenerator, flue gas is separated from the particles, the latter being reintroduced into the reaction zone via a stripper. The stripper section is described as particularly advantageous in the removal of carbon oxides and for the reduction of the heated catalyst particles. Parts of the hydrogen produced in the reaction zone are separated to be used as the stripping agent.

As specified in the patent, the reaction zone as well as the stripping zone include several superimposed grids, ensuring the break-up of any gas bubbles or channelled streams and redistribution of the downward particle flow. These further foster contact between hydrocarbon gas and catalyst and improve the hydrogen yield and stripping efficiency, respectively.

The complexity of the system and the costs of the catalyst inhibited further development of the process beyond a laboratory plant (Abánades et al., 2013; Muradov, 2000a; Schneider et al., 2020). Furthermore, the emissions of CO_2 make the process undesirable for today's standards if not sequestrated (Schneider et al., 2020).

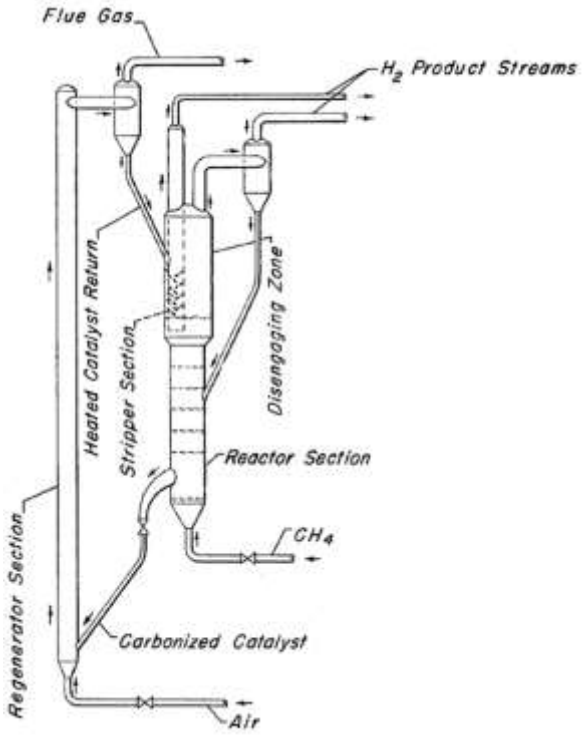

Figure 8: HYPRO process as proposed by Pohlenz & Scott (1963)

2.4.2 Florida Solar Energy Center

In a research project by the Florida Solar Energy Center prepared for the United States Department of Energy, an AC catalyst was used for methane pyrolysis with the target product being hydrogen (University of Central Florida, 2004). They patented a system similar to the HYPRO-process with two separate fluidised beds (Muradov, 2003). One of those was used to decompose methane, while the other regenerated the spent catalyst with an air–hydrocarbon mixture. The resulting water vapour and carbon dioxide is supposed to activate the catalyst by partial gasification. Muradov (2003) and Muradov et al. (2005a) describe the process as follows and as depicted in Figure 9. Hydrocarbon feedstock is decomposed over an AC catalyst in the first fluidised bed reactor. The gases leaving at the top are transferred to a PSA unit, where hydrogen is separated from the remaining hydrocarbon gases. Part of the hydrocarbon gas stream is combusted with air and used in the regeneration unit; the remaining part is recirculated into the pyrolysis chamber. Spent catalyst is transferred to the regeneration unit via a carbon separator and grinder. After treatment with CO_2 and steam, reactivated catalyst is reintroduced into the pyrolysis reactor.

The largest test unit was a 3 kW thermo-catalytic reactor that was fed with pipeline natural gas and commercial grade propane, respectively (Muradov, 2003). The gaseous products had a hydrogen content of 45,5% when using natural gas as a feedstock and 61,8% when using propane. The gasification reactor was never put into practice and no further information regarding scale-up was published since 2005.

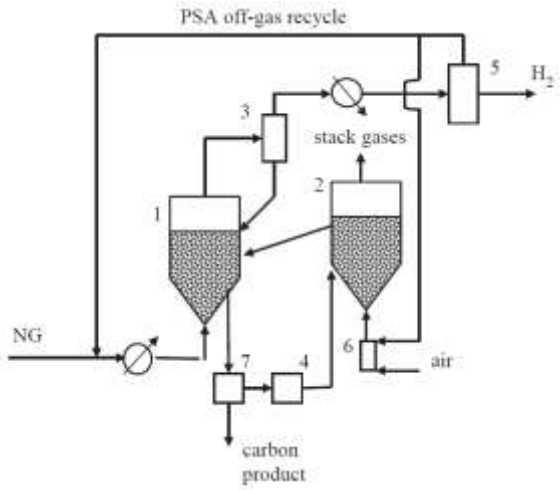

Figure 9: Schematic diagram of hydrogen and carbon production via thermo-catalytic decomposition of natural gas. (1) fluidized bed reactor, (2) fluidized bed heater-regenerator, (3) cyclone, (4) grinder, (5) gas separation unit, (6) combustor, (7) carbon separator. (Muradov et al., 2005a)

2.4.3 Hazer Group Limited

Western Australian company Hazer filed three patents regarding the production of hydrogen and graphitic carbon from hydrocarbons – specifically natural gas – using low-grade iron ore as a catalyst (Cornejo, 2016, 2018; Pocock, Cornejo, & Chua, 2016). One patent (Cornejo, 2018) was withdrawn in February 2021 (*European Patent Bulletin (13/2021)*, 2021). Pocock et al. (2016), propose a three-step fluidised bed reactor, operating at 850 °C and above atmospheric pressure according to Figure 10. The reactors are arranged in series with each subsequent reactor operating at a lower pressure than the preceding reactor. Specifically, the first reactor is operated at 18 bar, the second at 6 bar, and the third at 1 bar (atmospheric pressure).

Albeit being thermodynamically disadvantageous for the pyrolysis reaction itself, it is claimed that the higher pressure is beneficial overall as it fosters contact between the gas and the catalyst surface by promoting the diffusion of the hydrocarbon gas through the graphitic layer to the active iron sites. The methane and the catalyst are guided through the system in counter-flow. This operation mode allows unreacted catalyst to be fed into the lowest pressure reactor, converting methane while being partially deactivated. The catalyst is then transferred to a reactor of higher pressure, where the promoted diffusion into the graphite structure allows for further conversion and deactivation. This step is then repeated in a third reactor. This setup yields a gas stream containing 97 wt% hydrogen.

Pocock et al. (2016) and Cornejo (2016) show that the process requires a portion of the iron oxide to be converted to iron. In contact with methane, it decomposes to hydrogen and an iron carbide intermediate which precipitates from the metal grain boundaries as graphitic carbon. This force of graphite precipitation fractures the coated catalyst, exposing further catalytically active material and causing the disintegration of the metal structure by “dusting”. Similarly, little catalyst preparation is necessary as the catalyst activity is high and catalyst recovery is not required. They propose the graphite enveloped

iron particles to be small enough to allow suspension in the gaseous phase, allowing easy separation from gangue and iron oxide particles.

As of early 2021, Hazer is erecting a commercial demonstration plant, expected to produce 100 tonnes of hydrogen and ca. 380 tonnes of graphitic carbon per year (Hazer Group Limited, 2021). Target completion is 4Q 2021. Feedstock will be biogas from a next-door waste-water treatment plant; the heat necessary for the process will be provided through electrical heating (Ward, 2020).

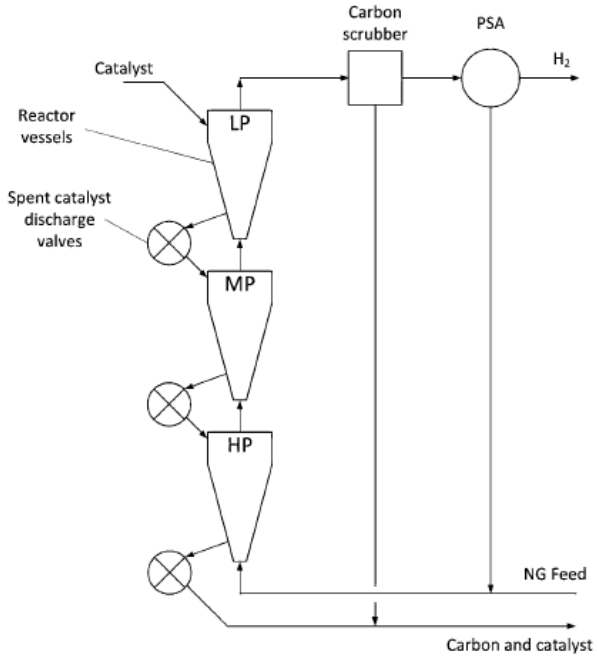

Figure 10: Schematic illustration of the hazer process according to Pocock et al. (2016). LP: low pressure; MP: medium pressure; HP: high pressure.

2.4.4 IASS / KIT

German Karlsruhe Institute of Technology (KIT) in collaboration with the Institute of Advanced Sustainability Studies e.V. (IASS) developed a liquid metal process for the decomposition of methane into hydrogen and solid carbon (Geißler, Plevan, Abánades, Heinzel, Mehravaran, Rathnam, et al., 2015; Geißler et al., 2016; Abánades, Muñoz, Martinez, Geissler, Stoppel, Dietrich, et al., 2018; Abánades, Muñoz, Martínez, Geissler, Stoppel, Dietrich, et al., 2019). The system is illustrated in Figure 11 and uses molten tin due to its broad liquid range and low vapour pressure. Preferably, the temperature of the molten phase is kept between 1050 and 1100 °C. The high corrosive properties of liquid tin require the use of a very resistant material. The proposed system uses a reactor pool out of quartz encased by a thermal insulator. The molten media has a depth of 1050 mm. Hydrocarbon gas is injected through orifices at the bottom of the metal pool, decomposing in contact with the tin and forming a hydrogen gas and solid carbon. The former is removed from the top, the latter accumulates at the surface of the liquid medium and is separated via a porous, rigid section.

Specifically, the porous, rigid section has double the width of the molten metal reactor. The part located above the liquid pool fills with carbon particles. The section then shifts from one side to the other, moving the full half off the pool to an adjacent part of the system where carbon is removed, while bringing the second – empty – part of the section above the pool to be filled with newly formed carbon. This ensures a continuous operation and uninterrupted hydrogen production.

In a proposed industrial-scale application, the hydrogen production is 2,15 kg/s in a 213,2 m² and 1 m deep metal pool (Abánades et al., 2018; Abánades et al., 2019). The off gas has a hydrogen content of 58,6%. A laboratory scale reactor in yielded a maximum of 78% hydrogen (Geißler et al., 2016).

In 2019, KIT started collaborating with German gas- and oil-producer Wintershall Dea GmbH to conduct research on, and lay the foundations for, an industrial application of the process (Heidelberger, 2019). The project is initially scheduled to run for three years.

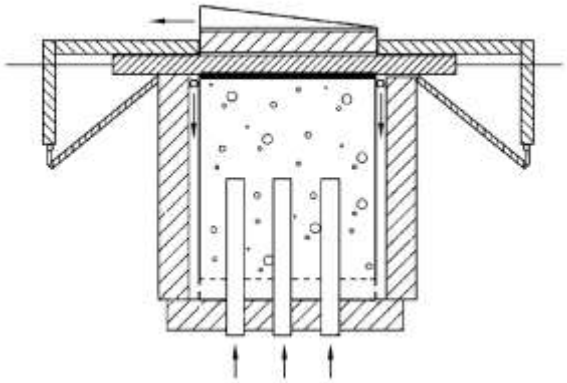

Figure 11: Schematic illustration of the process proposed by Abánades et al. (2019)

2.4.5 Tomsk Polytechnic University, Tomsk–Gazprom

Tomsk Polytechnic University in collaboration with Russian energy supplier Tomsk-Gazprom developed a methane pyrolysis process combining a catalytic and a plasmatic stage (Galanov, Zherlitsyn, Medvedev, Sidorova, & Shiyan, 2011; Korolev, Frants, Landl, Geyman, Zerlitsyn, Shiyan, et al., 2009; Zherlitsyn, Shiyan, & Demchenko, 2016). In their patents (Medvedev, Zherlitsyn, Gunther, Galanov, Shiyan, Ryabchikov, et al., 2005; Zherlitsyn, Medvedev, Shiyan, Korolev, & Franz, 2009; Zherlitsyn, Shiyan, & Kanaev, 2013) they claim that external heating for the pre-heating of the hydrocarbon gas in plasma-reactors leads to a high structural complexity and heat loss, further impeding a high hydrogen and carbon yield. The combination of an initiator (the catalyst) and plasma torch in the proposed system is said to bypass these problems.

The first patent (Medvedev et al., 2005) described a simple prototype of the system, comprised of a tubular reactor that crosses a microwave electromagnetic field a single time. In the latest patented process (Zherlitsyn et al., 2013) as in Figure 12, microwave energy is supplied to an S-shaped waveguide by a microwave generator, crossing the tubular reactor multiple times. The catalyst is placed inside a

cavity of the reactor in a state that provides unimpeded gas flow. The catalyst is characterised as a gas-permeable and electrically conductive substance that is heated by microwaves to a temperature of 400–700 °C. The methane-containing gas in contact with the catalyst primarily leads to the formation of unsaturated hydrocarbons – ethylene and acetylene – and active particles – ion radicals and excited molecules. Carbon nanotubes formed on the catalyst surface are knocked off by micro-discharges between the individual catalyst particles, prolonging its lifetime. The hydrocarbon products and gases are carried through a nozzle at the end of the reactor, after which the plasma of a gas microwave discharge induces the final decomposition to hydrogen and carbon. They propose the reactor to be made from quartz glass, as it exhibits the radiotransparent properties necessary to energise the catalyst while at the same time being heat resistant.

No further announcements on the scale-up of the process have been made since.

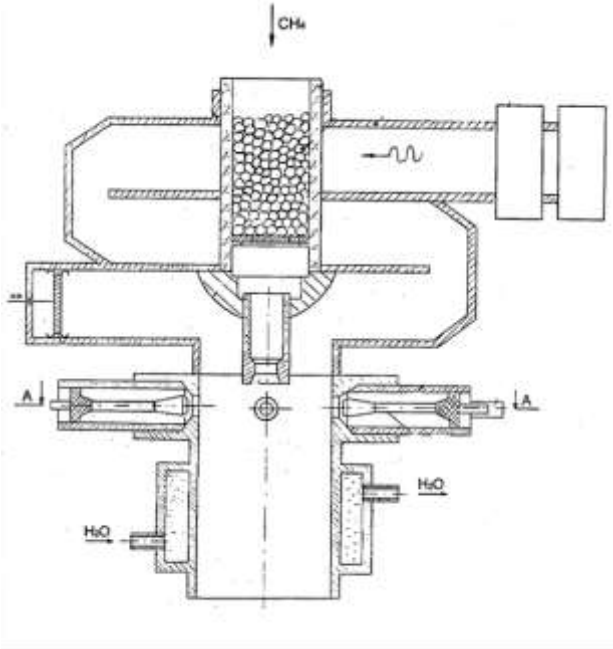

Figure 12: Schematic illustration of the process proposed by Zherlitsyn et al. (2013)

2.4.6 BASF SE

German chemical corporation BASF developed a moving bed process for hydrogen and high-quality coke (Maaß, Göke, Machhammer, Guzmann, Schneider, Hormuth, et al., 2012b, 2012a, 2012c). In the described system according to Figure 13, a granulate of coke is introduced at the top of a reactor and subsequently moves downward with the help of gravity. A hydrocarbon gas – preferably natural gas – moves in counterflow from the bottom to the top of the reactor. Both gas and coke do not require external pre-heating in this invention and exchange heat inside the reactor. This allows the upstreaming hydrogen-containing gas to cool off towards the top, exchanging heat with newly introduced coke particles. The temperature in the reactor reaches a maximum between 1100 and 1400 °C.

The energy necessary for the endothermic methane decomposition is introduced the following way: The discharged gas mixture is separated into a fraction containing pure hydrogen and a fraction containing a mixture of hydrogen and unreacted hydrocarbons; the latter phase is partially reintroduced into the reactor to maximise hydrogen yield and is partially oxidised; the oxidised – and as such hot – gas is routed through a heat exchanger to transfer heat to a part of the hydrogen stream, which is then reintroduced into the reactor, providing most of the required energy. The remaining hydrogen is released as the hydrogen product. In a recent report (BASF SE, 2021) heating is proposed to be carried out solely electrically, potentially avoiding CO_2 emissions altogether.

According to the patent, coke granules at the bottom of the reactor are classified and sieved, with particles of desired size being reintroduced, the rest being commercialised as high-quality furnace coke.

A follow-up research project is being carried out since 2019 in collaboration with several other industrial partners and universities and includes the construction of a test plant in Ludwigshafen (BASF SE, 2021; Bode, 2019). Construction was completed in 2020 (BASF SE, 2021).

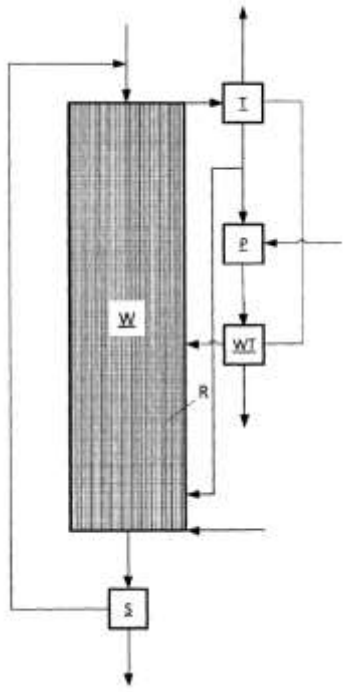

Figure 13: Schematic illustration of electrically heated moving bed as proposed by Maaß et al. (2012b). (P) burner, (R) reaction space, (S) separating device, (T) separating device, (W) moving bed, (WT) heat exchanger.

2.4.7 C-Zero

California-based start-up C-Zero Inc. uses molten media in a continuous flow process to produce hydrogen. In an interview published by St. John (2021), CEO Zach Jones said the company settled for a molten Ni–Bi catalyst as studied by Palmer, Bunyan, Gelinas, Gordon, Metiu, & McFarland (2020). Contrarily, previous documents – especially the presentation during their search for collaborators via US Advanced Research Projects Agency - Energy (McFarland, 2019) – indicated a focus on molten

salts. In their latest patent by McFarland, Upham, Palmer, Su, Mannini, Rahimi, et al. (2019), the focus is also on molten salt system, but combinations of molten metals and salts are also included and based on work by Rahimi et al. (2019). The company started fundraising in 2019 and targets the completion of a pilot plant by the end of 2022. The unit is supposed to produce 250 kg of hydrogen per day (Corey, 2021). Commercialisation of carbon is no target in their approach. In their search for collaborators in late 2019 to early 2020, carbon contamination by the metal catalysts is mentioned as a major issue (McFarland, 2019). It can be speculated this challenge is the reason for disregarding carbon marketing.

The process is designed to operate at elevated pressures of over 5 bar and temperatures around 1000 °C (McFarland, 2019). According to the CEO Zach Jones, the carbon separation technique is the distinguishable factor in their concept (St. John, 2021). In their two latest publicly accessible patents, McFarland et al. (2018; 2019) described systems working with molten salts. McFarland et al. (2019) disclosed several possible systems to remove the solid carbon from the melt. In one system according to Figure 14 (left), the carbon–salt mixture flows over a connection into a filter, retaining the solid carbon and guiding the molten salt back into the bottom of the melt. Another proposed system consists of two interconnected vessels according to Figure 14 (right). The first vessel is a molten salt on top of a molten metal bath. Molten salt containing the carbon – being raised by the moving gas bubbles – transfers to the second vessel where the carbon is removed. The molten salt then circulates back into the first vessel. All embodiments described in these patents consist of two separate sections which make use of the upward movement of the gas. The gas is introduced to the system in one section, initiating a circulating movement of the melt.

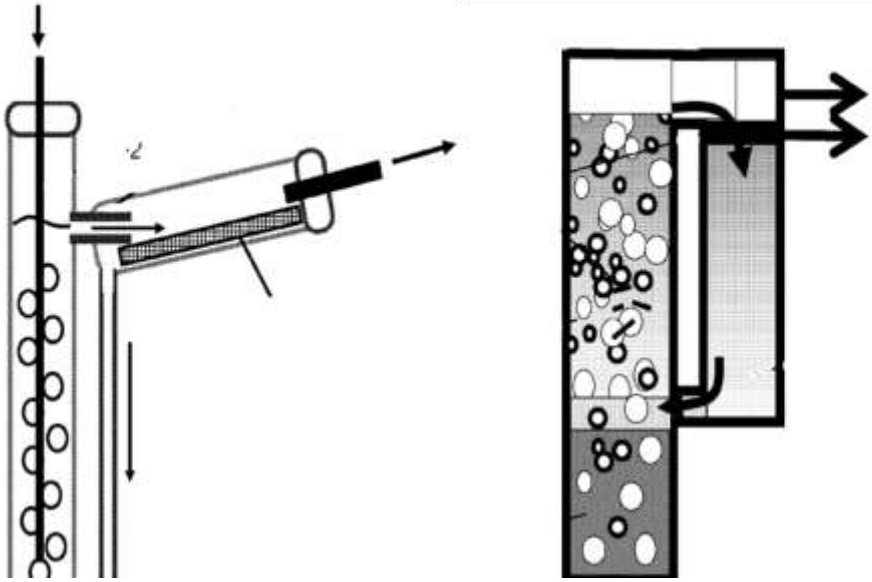

Figure 14: Proposed systems for carbon removal (McFarland et al., 2019)

2.4.8 TNO EMBER

Netherlands Organisation for Applied Scientific Research (TNO) has developed and filed a patent for the Ember process, a molten metal process for methane pyrolysis (TNO, n.d.). However, the patent is not publicly available yet (as of June 2021).

Leal Pérez et al. (2021) propose a molten metal reactor according to Figure 15, working at a pressure of 10 bar and a temperature of 1200 °C. The former reduces H_2 compression costs and permits a smaller reactor volume. The latter – relatively high temperature – is chosen to compensate for the loss of methane conversion by the elevated pressure. They suggest a porous distributor to generate micro-bubbles, as their large surface area aids a high conversion. Their small size also reduces reaction time and reactor volume. It is postulated that the reaction takes place at the gas–liquid interface. Molten gallium is used as – according to the authors – it allows complete separation of the carbon and gas stream. The proposed reactor is made of a high-nickel-chromium-iron alloy, which can withstand temperatures exceeding 1200 °C and the highly oxidative environment created by the liquid metal. Two concepts to supply the necessary energy are reported to be economically feasible: firstly, partially burning the produced carbon with subsequent carbon capture and storage; secondly, using electricity in an electric arc furnace. The former exhibits higher capital costs as it requires a burner, heat exchanger to cool down flue gases and a carbon capture and storage unit but could compete with the latter in the case of constant or increasing electricity prices. For efficient and complete separation of carbon from the molten metal catalyst, they suggest a molten salt bath floating atop the molten metal (TNO, n.d.).

The development of the Ember process is still at an early stage.

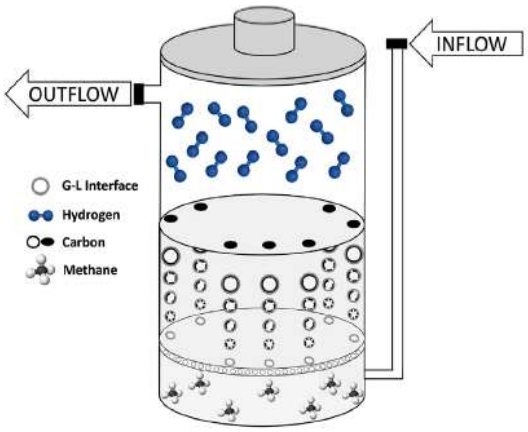

Figure 15: Schematic illustration of the system proposed by Leal Pérez et al. (2021)

2.4.9 Kvaerner Process & Monolith Materials

Norwegian Kvaerner Engineering were the first to develop a direct current plasma process with subsequent scale-up (Ahmed et al., 2009; Schneider et al., 2020). As described by Lynum, Hox, Haugsten, & Langoey (1993), the Kvaerner process is a two-reactor system, where NG is fed from the

top into the plasma reactor along with the plasma gas – which is hydrogen. There, NG is decomposed to carbon black and hydrogen. The decomposition products exit the torch at temperatures ranging from 3000 to 8000 °C. The subsequent reactor changes the physical properties of the carbon black so that the desired product quality is obtained. It does so by variation of temperature and a controlled supply of methane or admixtures. A pipe cooler with heat exchange is located downstream, followed by a complex separation system, removing carbon black of undesired quality form the main product. Hydrogen is partly reused as a plasma gas.

US based Monolith Materials based their plasma process on the Kvaerner technology (Schneider et al., 2020). In their patent (Hardman, Taylor, Hoermann, Johnson, Cardinal, & Hanson, 2016) as in Figure 16, the hydrocarbon injector is disclosed to be water cooled. Methane must be of low temperature when leaving the nozzle. A high temperature would lead to decomposition inside the nozzle and carbon product would precipitate. Upon exiting the nozzle, the hydrocarbon gas is added to a hot gas, which is composed of > 50% hydrogen and is heated and excited into the plasma state by passing an electrode annulus. The temperature of the hot gas exceeds 2400 °C. The authors picture the hydrocarbon gas to be heated by the hot gas. Heat should also be provided through heat radiation off the reactor walls, themselves being kept at desirable temperature ranges via external heating or via the hot gas as well. Residence time and temperature are controlled by moving the lead-in tube, adjusting the reactor volume. The decomposition products move further downward the reactor where the temperature decreases. Carbon atoms cluster together and form high-quality carbon nanoparticles. The further downstream equipment is composed of a heat exchanger, filter, degas chamber and backend. The mechanism targets the production of high-quality carbon nanoparticles that can reinforce elastomer compounds.

Monolith Material's first commercial production facility in Nebraska, USA, started operation in 2021 (Monolith Materials, Inc., 2021). The hydrogen is sent to a nearby power plant for electricity generation (Hardman, 2017). A second plant at the same location is expected to completion in 2024 (Monolith Materials, Inc., 2021).

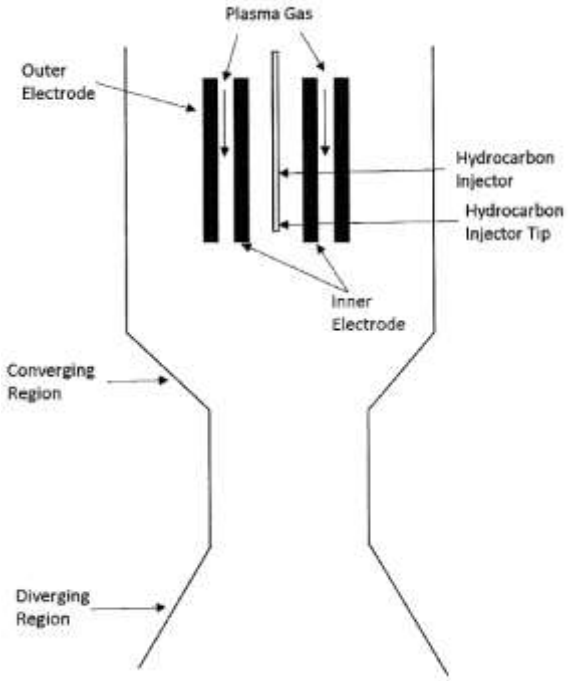

Figure 16: Schematic illustration of the Monolith Materials systems proposed by Hardman et al. (2016)

2.4.10 Carbotopia

Austrian Carbotopia developed a process using a supported iron catalyst in a fluidised bed reactor. First experiments towards this technology began around 2000 (Petters, 2020). The process as illustrated in Figure 17 works at temperatures of 560–850 °C and produces graphene-like carbon. Based on results on laboratory scale, a rotary reactor was constructed to prove the conversion rates of the catalyst in a continuous process (Mauthner, 2010). The apparatus could be operated continuously over the course of more than 6000 hours and had a production capacity of 13 kg carbon and 4,3 kg hydrogen per day (Timmerberg, Kaltschmitt, & Finkbeiner, 2020). However, catalyst was not recycled alongside. Spent catalyst was concentrated via reverse osmosis and dried (Mauthner, 2010). The authors claimed the remaining catalytic activity – tested in a laboratory-scale unit – was 30–40 % lower than for the fresh catalyst. The founder and another member of Carbotopia filed a patent on behalf of Chinese company Bestrong International Limited (Petters & Tse, 2011). They describe a fluidised bed reactor based on the process described above that separates particles rich in nanofibers from particles with less nanofiber loading through density separation. The invention also includes a sprayer that distributes catalyst on the support of bed material particles. No further public information on the process and its technological readiness could be found.

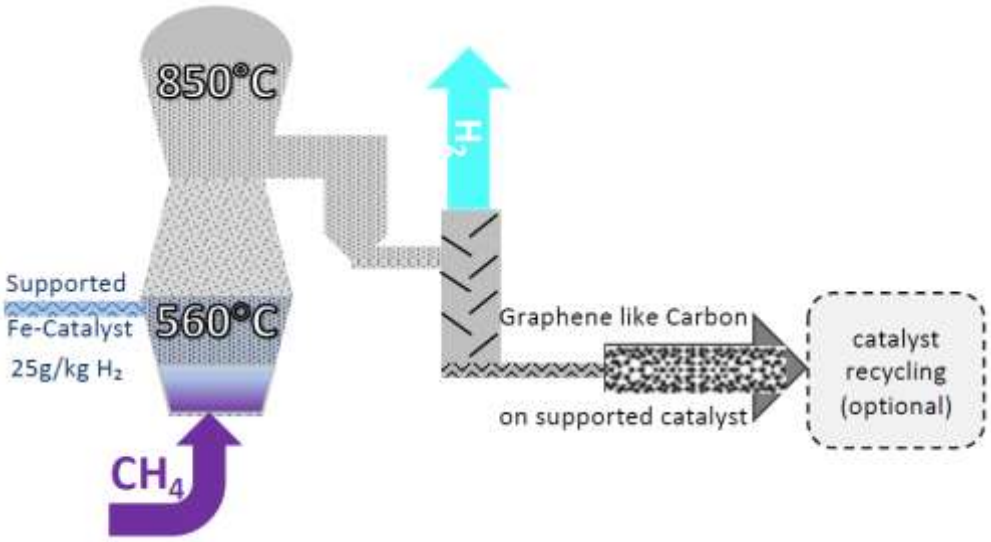

Figure 17: Schematic illustration of the process proposed by Carbotopia (Petters, 2020)

3 Fluidised Bed Systems for Methane Pyrolysis

3.1 Basics of Fluidised Bed Systems

This subchapter gives a quick introduction to general, fundamental theory of fluidised bed systems. Only relevant information contributing to the practical work of this thesis is included.

3.1.1 Properties of Particle and Parameters of Fluidisation

The size of a particle is indicated by its diameter. Since the shape of a grain hardly ever resembles a perfect sphere, several definitions exist to calculate a diameter equivalent. The most important ones can be described as follows.

- The *sieve diameter* d_p is defined by the side length of the square a particle still passes. It is determined by sieve analysis.
- The *volume-based particle diameter* d_V is represented by a sphere with the same volume as the particle.
- The *area-based particle diameter* d_S is represented by a sphere with the same surface area as the particle.
- The *Sauter mean diameter* d_{SV} is represented by a sphere with the same volume/surface area ratio as the particle. This diameter is used in most calculations. It is derived as in equation (1), with S being the surface area of the particle or sphere.

$$\frac{S_p}{V_p} = \frac{S_{Sp}}{V_{Sp}} = \frac{{d_{SV}}^2 \cdot \pi}{\frac{{d_{SV}}^3 \cdot \pi}{6}} \quad \Rightarrow \quad d_{SV} = 6 \cdot \frac{V_p}{S_p} \tag{1}$$

The *shape factor* ϕ is an indicator for the sphericity of a particle. It is used to approximate the Sauter mean diameter from the sieve diameter. It is defined as in equation (2) and can attain values from 0 to 1, in which $\phi = 1$ resembles a perfect sphere.

$$\phi = \frac{volume\ of\ sphere\ with\ equivalent\ volume}{surface\ area\ of\ particle} \tag{2}$$

Knowing the sieve diameter of a particle, the Sauter mean diameter can be approximated depending on their shape:

a) Particles approximately resembling a sphere: $d_{SV} \approx \phi \cdot d_p$.

b) Particles resembling an ellipsoid, in which the dominating dimension is no more than double the size of the other dimensions: $d_{SV} \approx d_p$.

c) Particles resembling an ellipsoid, in which the dominating dimension is more than double the size of the other dimensions: $d_{SV} \approx \phi^2 \cdot d_p$.

The *particle density* ρ_p is used in many fluidised bed calculations. The hydrodynamic density is of importance in fluidised bed systems. It represents the density of the material including all voids and pores. Contrarily, the absolute material density is defined by the subtraction of the volume of pores and is consequently higher.

The *minimum fluidisation velocity* U_{mf} defines the lowest speed of gas at which particles are suspended and form a fluidised bed with a constant pressure loss. A low viscosity and a low gas density lead to a high U_{mf}. Elevated temperatures increase the viscosity and decrease the density of the fluidising gas. Generally, the effect of an increasing viscosity outweighs the effect of a decreasing density, leading to a lower U_{mf}.

The *pressure loss in a fluidised bed* Δp_{fb} is defined by the total mass of the bed material. It is constant while the bed is in a fluidised state and can be approximated with:

$$\Delta p_{fb} = \frac{M \cdot g}{A}. \tag{3}$$

Figure 18 depicts the pressure loss through the bed material against the *superficial gas velocity* U_s, defined as the velocity of the gas in the empty tube. The sections fixed bed, fluidised bed, and pneumatic transport are clearly separated at specific velocities. In the state of a fixed bed, the pressure loss increases with U_s. Upon reaching U_{mf}, the pressure loss approaches a constant value Δp_{fb}.

A distinct transition from a fixed to a fluidised bed is only present in narrow grain size distributions. Wide grain size distributions will give a smooth transition between both states as indicated by the dash-dotted line. Increasing U_s further will eventually lead to the pneumatic transport of the particles upon reaching the *terminal velocity* U_t. The pressure loss slightly increases if the bed material is circulating in the system.

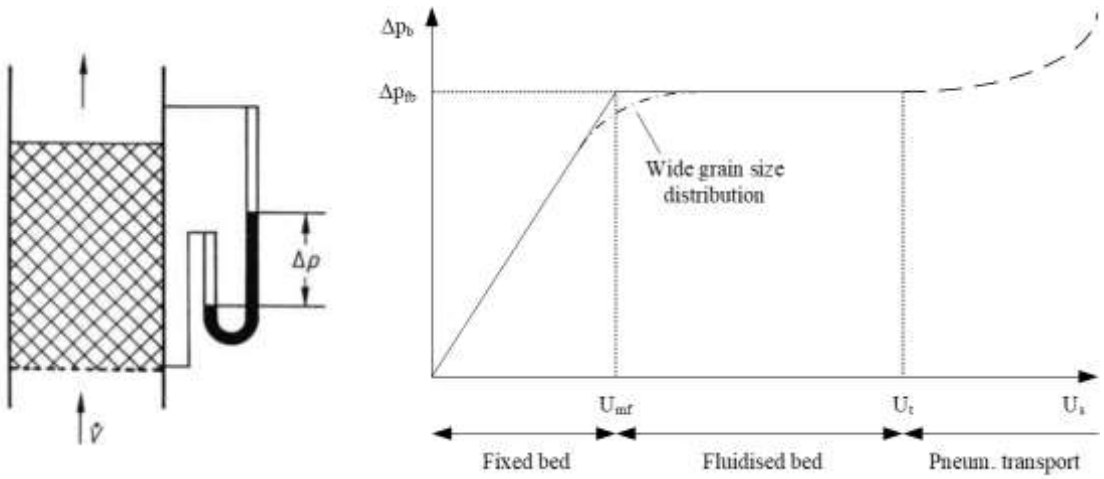

Figure 18: Pressure loss in flow through fixed bed, fluidised bed, and pneumatic transport. Modified from Werther (2000) and Hofbauer (1995).

The practical part of this thesis requires a relation between U_{mf} and d_{SV}. Multiple correlations link these values in gas–solid fluidisations, all highly empirical and system specific (Anantharaman, Cocco, & Chew, 2018). Some of these correlations require knowledge of the porosity and the form factor of the bed material, an information unavailable in these experiments. The Grace correlation is most suitable in the cases presented here and is as follows (Grace & Hetsroni, 1982):

$$Re_{mf} = (27{,}2^2 + 0{,}0408\, Ar)^{0{,}5} - 27{,}2 \tag{4}$$

with

$$Re_{mf} = \frac{d_{SV} \cdot U_{mf} \cdot \rho_g}{\mu} \tag{5}$$

and

$$Ar = \frac{(\rho_p - \rho_g) \cdot \rho_g \cdot d_{SV}^3 \cdot g}{\mu^2}. \tag{6}$$

3.1.2 States of Fluidisation

The regimes of fluidisation depend on the velocity of the fluid introduced into the vessel and the characteristics of the bed and type of particles. The most important ones are illustrated in Figure 19. Each of these regimes has distinct characteristics. Jakobsen (2014) describes the main characteristics of relevant types of fluidisation as subsequently presented.

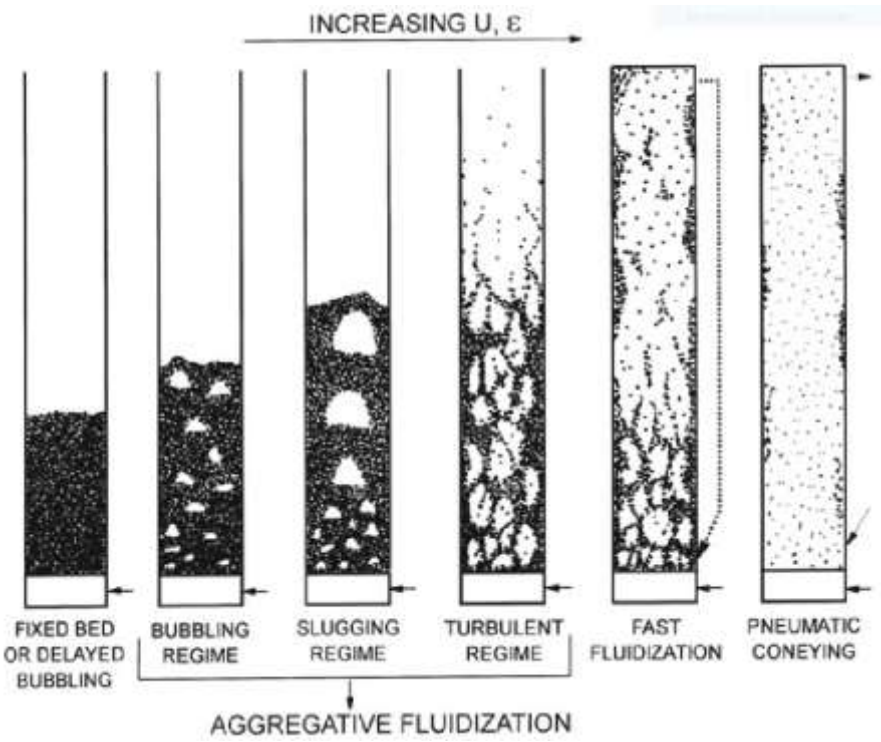

Figure 19: Primary gas–solid flow regimes (Jakobsen, 2014)

Fixed bed: a gas is flowing through a bed of particles at a low velocity. Particles are not in motion. The gas passes through voids in the bed.

Minimum fluidisation: the gas flow exerts an upward force on the bed of particles that just counteracts the vertical component of the compressive force of the particles. At this point, all particles are just suspended in the gas. The pressure drop is in equilibrium with the weight of the particles.

Smooth fluidisation: can usually only be seen when liquids are used as the fluidising agent. The bed of particles expands further above U_{mf} without the formation of bubbles.

Bubbling fluidisation: occurs above U_{mf} in most cases when gases are used for fluidisation. The gas forms bubbles that move through the bed. Bubbles can coalesce and break. Higher gas velocities enhance the coalescence of bubbles.

Turbulent fluidisation: at high superficial gas velocities close to the terminal velocity, the fluidisation becomes turbulent. The upper surface becomes diffuse and the concentration of particles in the freeboard significantly increases. Gas bubbles are more likely to break up in this regime, thus their mean size decreases.

Fast fluidisation: the superficial gas velocity surpassed the terminal velocity. Particles are transported out of the reactor. Clusters of particles move downward at the wall; individual particles are carried upwards in the centre of the tube.

Pneumatic transport: at an even higher gas velocity, all particles are entrained in the fluid and carried out of the vessel. The axial particle concentration is uniform.

3.2 Advantages of fluidised bed reactors for methane pyrolysis

Benefits of using fluidised bed reactors for TCD are elucidated below and compared to both steam methane reforming and other technologies used in methane pyrolysis. Some of the advantages are not unique to fluidised bed systems in TCD but apply to other processes as well.

3.2.1 Optimal Heat and Mass Transfer

Other reactor types – particularly fixed bed reactors – do not necessarily present a uniform temperature throughout the catalyst bed. Hot zones in the system might damage the catalyst (Dunker et al., 2006). Fluidised bed reactors on the other hand offer an easy temperature control and a homogeneous temperature throughout the reaction zone due to the constant and vigorous mixing of the catalyst particulates (Dunker et al., 2006; Pinilla, Suelves, Lázaro, Moliner, & Palacios, 2010; Werther, 2000).

For the design of a fluidised bed reactor, considerations regarding particle heat and mass transfer between fluid and particle are rarely necessary because of the large surface area of the catalyst (Werther, 2000). Heat transfer between the surfaces providing the heat to the system and the particles – often the reactor tube – must, however, be considered. Werther (2000) describes that in single-phase flow, a stagnant gas layer forms at the wall and impedes heat transfer. This layer is interrupted by solid particles carried to and along the wall. These particles absorb heat and remix with the fluidised bed.

Muradov (2001b) points out the possibility of implementing a continuous process with easy and constant addition and removal of fresh and spent catalyst, respectively. This is hardly possible in fixed bed systems. They further state the fluidised bed can act as a buffer when any sort of instability arises, be it temperature or fluidisation velocity or others.

3.2.2 Scale-up

Bringing TCD in fluidised bed reactors to industrial scale is no doubt a difficult and complex process that faces many challenges (Werther, 2000). However, scaling up of many other reactor types showed to be not feasible or present problems that are even harder to overcome. Muradov (2001b) tested various types of reactors for the application of TCD and identified fluidised bed systems to be the most reasonable for industrial application due to the easy addition and withdrawal of catalyst and carbon. Large-scale implementation of fluidised bed reactors in general depends a lot on good engineering practice with simplifications, approximations and educated guesses (Matsen, 1996).

Scaling up fluidised bed units comes with changes of design, geometry, and behaviour of gas-solids inside the reactor. The most important factors that affect the performance during scale up as identified by (Werther, 2000) are discussed as follows.

Typical laboratory scale units have a diameter of less than 60 mm, pilot plants are typically designed with diameters around 500 mm and large-scale units can have diameters of up to 10 m. Larger diameters

lead to a higher velocity of the individual bubbles and thus a shorter residence time, the latter being an important parameter in TCD. Gas distribution in small-scale units is often carried out in porous plates that have ideal distribution properties but display a comparably high pressure-drop. Industrial distributors usually perform worse and reduce the exchange area between bubble and catalyst. Internal fixtures, e.g. for heat exchange, can compensate for the reduction of heat and mass transfer that otherwise occur through the smaller surface–volume ratio. Secondary reactions (e.g. to form ethylene and acetylene) might be of significance in the freeboard. Cooling of the flue-gas happens much slower in large-scale reactors, giving additional time at reasonably high temperatures to react further. Finally, attrition might play a greater role in industrial applications due to higher superficial gas velocities and a larger bed height. This can affect the process both positively – as part of catalyst regeneration through removal of carbon deposits – and negatively – through breaking up of the catalyst particle or by detaching the metal from the catalyst support.

3.2.3 Avoiding Reactor Blockage

The build-up of carbon by-product on catalyst or reactor interfaces can be so severe that it leads to the complete blockage of the reactor. This has been reported to be an issue especially in packed bed reactors (Sánchez-Bastardo et al., 2020) and tubular reactors (Abánades et al., 2011).

Muradov (2001b) reported carbon layers adding up on the walls of tubular reactors, ultimately completely plugging the tube. In packed bed systems, particle size increases through carbon deposition, eventually blocking reactant gas flow (Abbas & Daud, 2010; Muradov, 2000b).

Fluidised bed reactors effectively avoid blockage. The catalyst bed is in constant motion and will simply increase in height as the reaction proceeds (Pinilla et al., 2011). Furthermore, carbon and catalyst can easily and continuously be removed from the system (Muradov, 2001b). Deposition on the reactor wall is hardly possible considering constant abrasion of adhered carbon from the reactor tube.

3.3 Disadvantages and Challenges of Fluidised Bed Reactors for Methane Pyrolysis

Challenges that need to be resolved or dealt with in TCD in fluidised bed reactors are primarily mechanisms that lead to catalyst deactivation. Relevant in that regard are coking, sulphur poisoning, sintering and mechanical degradation. Depending on the catalyst and other parameters, such as superficial gas velocity or temperature, these challenges can be resolved, but often result in other disadvantages. The separation of carbon presents a problem that is almost independent of catalyst and system settings. Some of the disadvantages listed here are not exclusive to fluidised bed systems but apply to other types of reactors as well.

3.3.1 Coking

The longevity of solid metallic and carbonaceous catalysts in TCD is all but exhaustive. The life time of most solid catalyst has been reported to be less than ten hours (Fan et al., 2021). The primary reasons for deactivation are the encapsulation of active sites and plugging of micro- and mesopores, commonly regarded to as coking (Amin et al., 2011).

The susceptibility to coking depends on the reaction conditions and the catalyst used. Carbon catalysts generally offer a higher stability than metal catalysts (Ashik et al., 2015). Carbonaceous catalysts could theoretically be used for an unlimited time through the formation of catalytically active carbon leading to an autocatalytic process. The catalytic activity of the formed carbon is, however, insignificant and thus an autocatalytic approach is not feasible (Muradov et al., 2005b). Metallic catalysts, on the other hand, eventually always undergo complete deactivation (Msheik et al., 2021). Carbon black catalysts are more resistant than AC catalysts (Muradov et al., 2005a). AC deactivates more rapidly than carbon black because carbon deposits in the micropores first.

3.3.2 Sulphur Poisoning

On sites larger than laboratory scale, methane will be supplied as natural gas or by other gases with a significant share of methane, such as biogas or landfill gas. Natural gas typically contains impurities of sulphur components such as hydrogen sulphide in concentrations of 5–500 ppm (Watanabe, Kaburaki, Shimoda, Igarashi, & Satokawa, 2017) Biogas and landfill gas also have a significant content of H_2S (Fidalgo, Muradov, & Menéndez, 2012). Sulphur poisoning has been said to play a role in TCD when using metal catalysts (Ashik et al., 2015). These are susceptible for sulphur chemisorption and deactivate upon sulphur accumulation (Rostrup-Nielsen, 1982). The hydrogen sulphide adsorbs to the active sites and reacts to a metal sulphide and hydrogen according to (xv) (Rostrup-Nielsen, 1982):

$$Me + H_2S \rightarrow MeS + H_2 \qquad (xv)$$

The active sites thus become inaccessible for the reactant. Bartholomew (2001) describes the effects of sulphur poisoning: An adsorbed sulphur atom physically blocks access to a reaction site. It forms a strong chemical bond it forms with the metal which influences the metal atoms adjacent to the respective site. Through electronic modification, these adjacent atoms lose their ability to adsorb or dissociate reactant molecules. The strongly bound sulphur may alter surface properties of the metal that affect catalytic properties in reactions sensitive to structural changes – as is the case in TCD (Abbas & Daud, 2010). Furthermore, adsorbed sulphur blocks access of reactants to each other. Another effect relates to the diffusion of adsorbed reactant which is slowed down or is stopped altogether as sulphur poisoning continues.

It is important to note that sulphur poisoning is only problematic when using metallic catalysts (Fidalgo et al., 2012). This effect is not exclusive to fluidised bed systems but occurs in fixed bed systems the same way.

3.3.3 Separation of Carbon

Contrary to the molten media processes, where solid carbon can be skimmed from the top of the melt, or plasma systems, where carbon particulates are entrained in the gas stream and removed by bag filters, separation of carbon from the solid catalyst surface is more challenging (Abbas & Daud, 2010). Muradov (2000b) suggested the removal of carbon to be easier in fluidised bed units than in other types of reactors, e.g. packed bed reactors, as the process could be operated continuously. Overall, however, little research has been done regarding the separation of carbon from the catalyst. Generally, separation is only required in metal catalysts. Carbonaceous catalysts do not demand separation; carbon deposits on the carbon catalyst surface and its excess could be removed continuously (Muradov, 2002).

Shah, Ma, Wang, & Huffman (2007) reported problems with the separation of carbon nanotubes from a Mo–Fe catalyst on Al_2O_3 support in a fluidised bed. Their hypothesis that carbon nanotubes will detach from the catalyst interface through attrition could not be confirmed. Ammendola, Chirone, Ruoppolo, Russo, & Solimene (2008) proposed a computational model of TCD in fluidised bed reactors and compared the result to experimental data obtained by Ammendola, Ruoppolo, Chirone, & Russo (2006) using a copper-based catalyst on alumina support. Contrary to Shah et al. (2007), they could verify attrition plays a role in catalyst regeneration. I.e., carbon was indeed removed from the catalyst interface.

Parmar, Pant, & Roy (2021) studied the extraction of carbon nanotubes by ultrasound. They used a Ni–Cu–Zn catalyst on Al_2O_3 support in a fluidised bed reactor and stopped the pyrolysis reaction at various defined carbon loadings. The spent catalyst was then ultrasonicated in a water bath. The treated catalyst was subsequently magnetically separated and calcinated for reutilisation. The separation efficiency was measured in % carbon nanotube separation from the spent catalyst. When the carbon loading was higher, a better separation efficiency could be achieved. E.g. the separation efficiency when treating a used catalyst with 70 wt% carbon reached 45–50%, when treating used catalyst with 30 wt% carbon a separation efficiency of only 25–30% could be achieved. This could mean that carbon deposited later on in the process is more loosely bound to the catalyst compared to carbon that adhered early on.

Suelves et al. (2005) suggested that a low concentration of catalyst in the carbon could be acceptable for some applications and enable the marketing of the by-product without purification. This implies, however, that the amount of carbon accumulated until deactivation needs to be significant to compensate the cost of the catalyst and to reduce its concentration in the carbon.

3.3.4 Sintering at High Temperatures

Using metal catalysts at elevated temperatures can cause thermal sintering (Sánchez-Bastardo et al., 2020). This problem is not exclusive to fluidised bed reactors but exists in all processes involving a metal catalyst. However, sintering may initiate defluidisation only in fluidised bed systems. Sintering is irreversible or difficult to reverse at best, making prevention the preferable strategy (Bartholomew, 2001). Carbonaceous catalysts effectively bypass this issue (Abbas & Daud, 2010). A strong metal–support interaction in metallic catalysts can also reduce the risk of thermal agglomeration (Sánchez-Bastardo et al., 2020).

Sintering typically refers to two thermally induced processes: the loss of surface area through crystallite growth of the catalytic phase; and the loss of support area due to support collapse or the loss of catalytic surface area caused by pore collapse (Bartholomew, 2001).

The speed of agglomeration in TCD is influenced by various parameters (Bartholomew, 2001). Presence of water increases the sintering rate of supported metal, which should therefore be considered when regenerating with steam. Reacting with steam, the metal support forms mobile surface hydroxyl groups that are subsequently volatilised at higher temperatures. A strong metal–support interaction can reduce the risk of sintering. In reducing atmospheres (as is the case in methane pyrolysis), the metal crystallite stability is positively affected by a high melting point of the metal. Generally, sintering rates increase exponentially with temperature.

Sintering of catalyst particles generates problems by the increasing particle size and its associated loss of surface area. It can ultimately lead to defluidisation of the catalyst bed. It is postulated in a model established by Tardos, Mazzone, & Pfeffer (1985a, 1985b), that agglomerates form in between two consecutive bubbles passing through, and under a pressure force that is influenced by the bed height. Both parameters foster sintering. Pinilla, Moliner, Suelves, Lazaro, Echegoyen, & Palacios (2007) studied the behaviour of a Ni–Cu–Al catalyst in a pilot-scale fluidised bed system at 700 °C. The catalyst particles were smaller than 100 µm. In regimes with low fluidisation velocities – close to U_{mf} – defluidisation phenomena occurred. They attributed the loss of fluidisation to bigger catalyst particles that accumulate at the bottom and ultimately agglomerate. At higher superficial gas velocities – at 2x U_{mf} – continuous fluidisation was possible, confirming the previously described findings.

3.3.5 Mechanical Degradation

Commercial catalysts are prone to mechanical failures primarily due to their composition (Bartholomew, 2001). Bartholomew (2001) shows: catalysts with particle diameters ranging from several µm to cm are prepared by agglomeration of 0,02–2 µm aggregates of much smaller primary particles with diameters in the 10–100 nm range; the strength increases in the form of: agglomerates < aggregates < primary particles.

Bartholomew (2001) further defines two mechanisms involved in the failure of catalyst agglomerates: fracture of agglomerates into smaller agglomerates; and abrasion of aggregates of primary particles from the surface of the agglomerate. The former is caused by mechanical forces, the latter by mechanical, thermal, or chemical forces. Mechanical stresses are induced by agglomerates colliding with each other or the reactor wall. They can also be caused by shear forces from turbulent eddies. Thermal stresses are induced by a rapidly changing temperature or temperature gradients within the particles. Chemical stresses are caused by phase changes within the particle. These can lead to a change in density and split the particle. Muradov & Vezirolu (2005) pointed out that supported metal catalysts may deteriorate quickly since carbon nanotube or filament formation occurs primarily at the metal–support interface and finally detaches the metal from the support. This may lead to undesirable and costly consumption of metals.

Mechanical failure is a mechanism that is not exclusive to fluidised bed reactors but occurs in all processes involving solid catalyst particles. However, due to the constant movement of the bed particles in fluidised operation and the consequently higher mechanical stresses on the individual agglomerates, it can be said that fluidised beds are more prone to catalyst failure by degradation than e.g. packed bed reactors.

4 Applied Principles and Methods

4.1 Experimental Setup

4.1.1 Overview of the Overall Plant

The apparatus applied in the practical work is a fluidised bed reactor. The bed material is filled into the reactor via a chute at the top. To remove it, the device flange must be opened and the upstream section of the apparatus must be lowered. The gas input at the bottom of the plant follows a vertical tube acting as a preheater. The gas stream then passes a perforated plate and the subsequent fluidised bed before flowing through the freeboard. Both the preheater tube and the tube around the bed material and freeboard are heated via two semi-circular heater shells each. A slightly downwardly inclined pipe connects the reactor to a gravity separator, separating coarse particles from the gas stream and collecting them in a container. The off gas is then filtered with glass wool to remove remaining entrained particles. A sample of the stream is separated to an analysis unit, the remaining off gas is burned if necessary and removed in a chimney.

The test run with AC as bed material and steam as the regenerating agent requires the gas stream used for regeneration to be rerouted. During regeneration, the valves of the main gas route are being closed and a second cycle to saturate a nitrogen gas stream with steam is established. Three gas wash bottles connected via silicon tubes are utilised for this process. The flasks are halfway filled with water and placed in a cryostat to keep the temperature at a constant 81 °C. Considering the vapour pressure at this temperature, the total flow rate after saturation approx. doubles. To provide an even flow through with small bubble diameters, ensuring a saturated gas, bottles with a porous filter plate are employed. Heating of the downstream tubes with heating cords is required to avoid condensation.

4.1.2 Measurement and Regulation Equipment

The gas flow is regulated by hand in rotameters with an upstream control valve. The rotameters regulating CH_4 and CO_2 are calibrated to 6 bar absolute pressure and 25 °C, the rotameter regulating N_2 and air flow is calibrated to 8 bar absolute pressure and 25 °C. Since the gas streams meet the rotameter with an absolute pressure of 6 bar, N_2 and air flow rates need to be adjusted using a correction factor as presented in (7) and (8).

$$f_P = \sqrt{p_{op}/p_{cal}} \tag{7}$$

$$\dot{m}_{op} = f_P * \dot{m}_{cal} \tag{8}$$

The off-gas sample is analysed both continuously by a continuous gas analyser unit and in 12-minute intervals by a gas chromatography unit. The continuous measurement is conducted in a Rosemount NGA 2000, measuring O_2, H_2, CO_2, CO and CH_4. It allows for a precise estimation of the flue gas composition over time and consequently for the calculation of the total mass of the products generated during the test. The only predominant drawback of the continuous analysis is a slightly less precise measurement. The gas chromatographer – a Perkin Elmer gas chromatography unit measuring CH_4, C_2H_6, C_2H_4, C_2H_2 and O_2/Ar – delivers additional data on higher hydrocarbons.

Temperature measurements are performed in the preheater, the bed material, the freeboard, and the cyclone. The bubbling bed temperature is the most relevant for methane pyrolysis in fluidised bed reactors and therefore taken as the reference when experiments are conducted. The plant is operated at atmospheric pressure; thus, the pressure drop in the perforated plate and fluidised bed can be estimated by measuring the pressure in the preheater against ambient conditions.

4.2 Estimation of d_{SV} and U_{mf}

Obtaining both unknown values requires the measurement of one of them. Sieve analysis and – depending on the shape of the particles – applying a form factor can be used to estimate d_{SV}. U_{mf} can be calculated by measuring the pressure loss at a broad variety of flow rates. The latter was applied here.

The pressure loss in a fluidised bed is composed of one component resulting from the plate, and another component resulting from the weight of the material. While the former is crucial for a uniform gas distribution, the latter is of interest here. The pressure measurement was conducted upstream the perforated plate. Hence, it was necessary to analyse the pressure drop of the plate upfront. It was then subtracted from the pressure losses measured with the bed materials filled in. The pressure difference in a fixed bed increases with flow rate. Contrary, in a fluidised bed, it is constant and can be approximated with (3).

The velocity at which the pressure difference changes over from an increase to a constant value is defined as the U_{mf}. For broad particle size distributions – which is the case here – this transition is gradual. Therefore, the linear parts of the fixed and fluidised bed must be elongated. The intersection of these graphs, referencing to Figure 18, defines U_{mf}.

The measurements were performed in a laboratory scale fluidisation reactor at standard ambient temperature and pressure. The relevant parts of the reactor were a metal tube with a diameter of 54,4 mm and a perforated plate for gas distribution. The fluidising agent was air. Flow rates ranging from 0,2 Nm³/h to 2 Nm³/h were used, starting with the highest, and reducing it in steps of 0,1 Nm³/h. The corresponding pressure losses were noted. These values were then plotted to find U_{mf} as described above. The particle diameter was then estimated employing the Grace correlation in (4) and mathematical software.

4.3 Methane Conversion

The methane conversion is a measure for efficiency in fluidised bed systems. A high methane conversion correlates with a high hydrogen yield and is crucial for a profitable process.

The overall conversion of methane is defined as the amount of converted substance in relation to the initially employed substance:

$$X_{CH_4} = \frac{\dot{n}_{CH_4,in} - \dot{n}_{CH_4,out}}{\dot{n}_{CH_4,in}}. \tag{9}$$

Using (14), the equation

$$X_{CH_4} = \frac{1}{\dot{n}_{CH_4,out} + \frac{1}{2}\dot{n}_{H_2}} \cdot \frac{1}{2}\dot{n}_{H_2} \tag{10}$$

can be obtained. Extending the right side with $\dot{n}_{tot,out} / \dot{n}_{tot,out}$, the methane conversion can be calculated solely using data from the flue gas measurement:

$$X_{CH_4} = \frac{1}{\dot{n}_{CH_4,out} + \frac{1}{2}\dot{n}_{H_2}} \cdot \frac{1}{2}\dot{n}_{H_2} \cdot \frac{\dot{n}_{tot,out}}{\dot{n}_{tot,out}} = \frac{1}{x_{CH_4,out} + \frac{1}{2}x_{H_2}} \cdot \frac{1}{2}x_{H_2}. \tag{11}$$

The values obtained through (11) are then divided by the maximum methane conversion rate in each test run:

$$X_{CH_4,rel} = \frac{X_{CH_4}}{X_{CH_4,max}}. \tag{12}$$

4.4 Hydrogen Production and Carbon Balance

Obtaining additional information on hydrogen production rate and the quantity of formed carbon and its deposited is crucial in understanding the pyrolysis process and its upscaling. Given that only the volumetric flow rate of methane at the inlet and the flue gas composition is known, some stoichiometric relations must be introduced. The amount of formed carbon is then compared to the change in mass of the bed material and the mass of material deposited in the gravity separator, filters, and reactor walls. A discrepancy is expected due to imprecisions in the flue gas measurement, especially at low reaction rates over long time periods.

The total molar flow rate of the flue gas is the sum of the molar flow rates of all substances in the off gas:

$$\dot{n}_{tot,out} = \dot{n}_{H_2} + \dot{n}_{CH_4}\left(+\dot{n}_{CO} + \dot{n}_{CO_2}\right). \tag{13}$$

It must be noted that the molar gas flow rates before and after the fluidised bed differ. The inlet methane stream is partially decomposed, the rest leaves the reactor unaffected. For each mol of decomposed methane, two mol of hydrogen are obtained. Given this stoichiometric factor, the molar balance is as follows:

$$\dot{n}_{tot,in} = \dot{n}_{CH_4,in} = \frac{1}{2}\dot{n}_{H_2} + \dot{n}_{CH_4,out}\left(+\dot{n}_{CO} + \dot{n}_{CO_2}\right). \tag{14}$$

The composition of the flue gas is measured in volumetric ratios, which are equivalent to molar ratios in ideal gases. The molar ratio is defined as follows:

$$x_i = \frac{n_i}{n_{tot}} = \frac{\dot{n}_i}{\dot{n}_{tot}}. \tag{15}$$

Dividing equation (14) by $\dot{n}_{tot,out}$ as in (13) and considering (15), gives:

$$\frac{\dot{n}_{CH_4,in}}{\dot{n}_{tot,out}} = \frac{1}{2}x_{H_2} + x_{CH_4,out}\left(+x_{CO} + x_{CO_2}\right) \tag{16}$$

$$\Rightarrow \quad \dot{n}_{tot,out} = \frac{1}{\frac{1}{2}x_{H_2} + x_{CH_4,out}\left(+x_{CO} + x_{CO_2}\right)} \cdot \dot{n}_{CH_4,in}. \tag{17}$$

Dividing (13) by itself leads to:

$$1 = x_{H_2} + x_{CH_4,out}\left(+x_{CO} + x_{CO_2}\right). \tag{18}$$

Ergo, the right side of (16) can be written as:

$$\frac{1}{2}x_{H_2} + x_{CH_4,out}\left(+x_{CO} + x_{CO_2}\right) = 1 - \frac{1}{2}x_{H_2}. \tag{19}$$

By expansion of the left side of equation (17) with $^{x_i}/_{x_i}$, the unknown $\dot{n}_{tot,out}$ can be eliminated:

$$\dot{n}_{tot,out} \cdot \frac{x_i}{x_i} = \dot{n}_{tot,out} \cdot \frac{\dot{n}_i}{\dot{n}_{tot,out}} \cdot \frac{1}{x_i} = \frac{\dot{n}_i}{x_i}. \tag{20}$$

Combining equations (17), (19) and (20), the molar flow rate of each component in the off gas can be calculated as:

$$\dot{n}_i = \frac{1}{1 - \frac{1}{2}x_{H_2}} \cdot x_i \cdot \dot{n}_{CH_4,in}. \tag{21}$$

To determine the entire amount of substance that has been produced, equation (21) must be integrated over time:

$$n_i = \frac{1}{1 - \frac{1}{2}x_{H_2}} \cdot x_i \cdot \dot{n}_{CH_4,in} \cdot \Delta t. \tag{22}$$

To determine the hydrogen production rate, molar mass must be introduced in equation (21):

$$\dot{m}_i = \frac{1}{1 - \frac{1}{2}x_{H_2}} \cdot x_i \cdot \dot{n}_{CH_4,in} \cdot M_i \,. \tag{23}$$

Based on stoichiometric considerations, the amount of deposited carbon is equivalent to twice the amount of produced hydrogen:

$$n_C = 2n_{H_2} \,. \tag{24}$$

4.4.1 Influence of Regeneration and Activation Steps

Some test runs required activation or regeneration steps that were carried out with carbon dioxide or a steam–nitrogen mix. Carbon is a reactant in these processes, thus some of the produced carbon is consumed in these phases. The calculation of the total amount of carbon used in these reactions is done in a similar way. The resulting equations to calculate the amount of used carbon is presented as follows, the individual derivations can be found in the Annex.

Regenerating with steam, the amount of substance can be calculated with:

$$n_i = \frac{x_i}{1 - \left(x_{CO} + x_{CO_2} + x_{H_2}\right)} \cdot \dot{n}_{N_2} \cdot \Delta t \,, \tag{25}$$

and

$$n_C = n_{CO} + n_{CO_2} \,. \tag{26}$$

Regenerating with carbon dioxide, the amount of substance is:

$$n_i = \frac{1}{1 - x_{CO}} \cdot x_i \cdot \dot{n}_{CO_2,in} \cdot \Delta t \,, \tag{27}$$

with

$$n_C = \frac{n_{CO}}{2} \,. \tag{28}$$

4.4.2 Carbon Deposits on Internal Surfaces

Some of the product carbon is deposited on the reactor walls. To quantify this amount for each trial, the reactor is burnt out with air at a known volumetric flow rate.

The chemical reactions are as follows:

$$C + O_2 \rightarrow CO_2 \tag{xvi}$$

$$C + \frac{1}{2}O_2 \rightarrow CO \tag{xvii}$$

The reaction is incomplete. Thus, the flue gas is composed of not only the products carbon dioxide and carbon monoxide along with nitrogen, but remaining oxygen as well:

$$\dot{n}_{tot,out} = \dot{n}_{CO} + \dot{n}_{CO_2} + \dot{n}_{O_2,out} + \dot{n}_{N_2,out} \tag{29}$$

The inlet gas is air, containing primarily oxygen and nitrogen. The inlet air flow can be described as the sum of the outlet gas flow rates for each component, considering stoichiometry from (xvi) and (xvii):

$$\dot{n}_{tot,in} = \dot{n}_{air} = \frac{1}{2}\dot{n}_{CO} + \dot{n}_{CO_2} + \dot{n}_{O_2} + \dot{n}_{N_2} \tag{30}$$

Dividing (30) by $\dot{n}_{tot,out}$ as in (29) leads to:

$$\frac{\dot{n}_{air}}{\dot{n}_{tot,out}} = \frac{1}{2}x_{CO} + x_{CO_2} + x_{O_2,out} + x_{N_2,out} \tag{31}$$

$$\Rightarrow \quad \dot{n}_{tot,out} = \frac{1}{\frac{1}{2}x_{CO} + x_{CO_2} + x_{O_2,out} + x_{N_2,out}} \cdot \dot{n}_{air} \tag{32}$$

Considering that equation (29) divided by itself leads to:

$$1 = x_{CO} + x_{CO_2} + x_{O_2,out} + x_{N_2,out} \tag{33}$$

The right side of (31) can be written as:

$$\frac{1}{2}x_{CO} + x_{CO_2} + x_{O_2,out} + x_{N_2,out} = 1 - \frac{1}{2}x_{CO} \tag{34}$$

Expanding the left side of (32) with $^{x_i}/_{x_i}$:

$$\dot{n}_{tot,out} \cdot \frac{x_i}{x_i} = \dot{n}_{tot,out} \cdot \frac{\dot{n}_i}{\dot{n}_{tot,out}} \cdot \frac{1}{x_i} = \frac{\dot{n}_i}{x_i} \tag{35}$$

Recombining (35) with (32) and entering (34) into the equation leads to:

$$\dot{n}_i = \frac{1}{1 - \frac{1}{2}x_{CO}} \cdot x_i \cdot \dot{n}_{air} \tag{36}$$

Integrating (36) over time:

$$n_i = \frac{1}{1 - \frac{1}{2}x_{CO}} \cdot x_i \cdot \dot{n}_{air} \cdot \Delta t \tag{37}$$

Finally, the amount of carbon deposited on reactor surfaces is equal the combined amounts of CO_2 and CO in the flue gas:

$$n_C = n_{CO_2} + n_{CO} \tag{38}$$

5 Results

This chapter presents the results of each individual experiment with all necessary details. For each bed material, a table with its important characteristics – such as particle diameter d_{SV}, minimum fluidisation velocity U_{mf} and elemental analysis – is presented. Also, rough estimations of their catalytic activity and possible carbon products are given. In every test run, the hydrogen production and – if applicable – share of CO and CO_2 in the flue gas, CH_4 conversion relative to the maximum value in respective experiment, temperature, and pressure loss profile are presented and thoroughly discussed. An assessment of the carbon balance is also included.

5.1 Methane Pyrolysis with Limestone as Bed Material

Bed material	355 g $CaCO_3$/199 g CaO
Catalyst	CaO
U_{mf} (air, 20°C)	150,3 mm/s ($CaCO_3$) / 85,6 mm/s (CaO)
d_{SV}	380 µm
Bed temperature	900 °C
Fluidisation during pyrolysis	(a) 69 mm/s (25% CH_4, 75% N_2) (b) 87 mm/s (41% CH_4, 59% N_2) (c) 71 mm/s (100% CH_4)

Table 1: Parameters Limestone

Figure 20: Bed material Limestone

The first investigated material was limestone (Figure 20). It was screened before the trial to remove very coarse and fine particles and to obtain a particle size distribution from approx. 300 µm to 600 µm. Table 1 shows the parameters for this test run.

The bed material was heated using nitrogen as a fluidising agent. A characteristic of calcium carbonate is the thermal decomposition at elevated temperatures. Starting at temperatures above 600 °C during the heating step, it reacts to calcium oxide and carbon dioxide as per (xviii):

$$CaCO_3(s) \rightarrow CaO(s) + CO_2(g)\,. \qquad (xviii)$$

This process can excellently be observed through exhaust gas measuring as depicted in Figure 21. It shows a slow start of the thermal decomposition at a temperature of 600 °C, followed by a continuous acceleration of the reaction with increasing temperature. Interestingly, the decomposition reaction does not phase out, rather, it stops abruptly after all material has reacted. The temperature profile in the same figure is characterised by the endothermic nature of this reaction. The higher the yield at any given moment, the slower becomes the heating process. After decomposition is concluded, the bed temperature increases sharply.

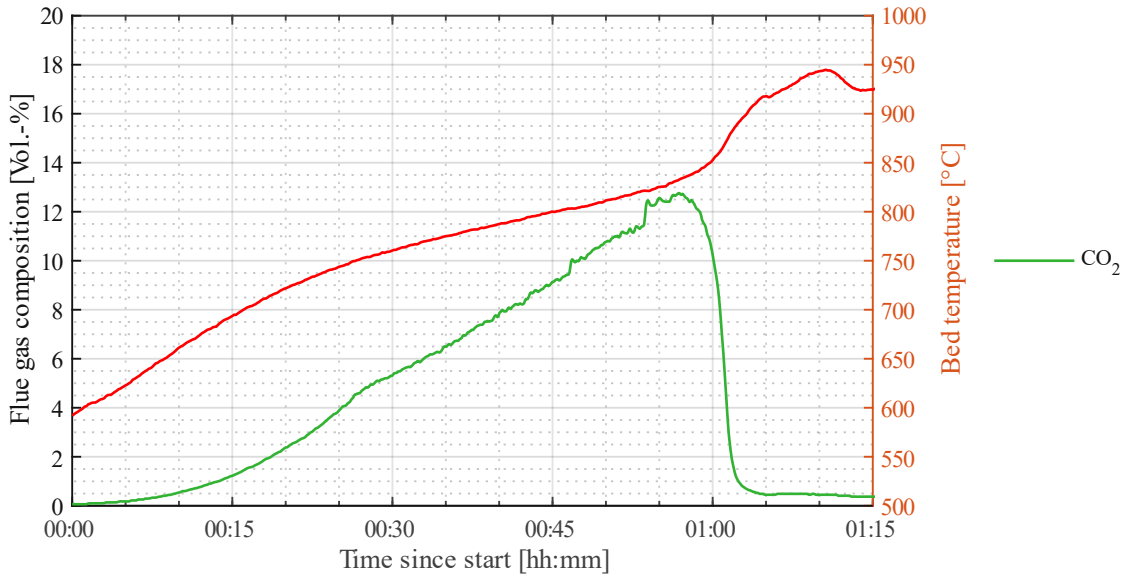

Figure 21: Thermal decomposition of limestone

The decomposition reaction causes a loss of mass. The mass of calcium carbonate being known, this reduction can directly be calculated using stoichiometric relations from the reaction. Stoichiometry shows that:

$$n_{CO_2} = n_{CaCO_3} = \frac{m_{CaCO_3}}{M_{CaCO_3}}. \tag{39}$$

The same can be achieved using the flow rate of nitrogen and the volumetric amount of carbon dioxide in the flue gas. The final equation is:

$$n_{CO_2} = \frac{x_{CO_2}}{1 - x_{CO_2}} \cdot \dot{n}_{N_2} \cdot \Delta t\,. \tag{40}$$

The derivation of (40) can be found in the Annex.

In both cases, the loss of mass is then equivalent to:

$$m_{loss} = m_{CO_2} = n_{CO_2} \cdot M_{CO_2}\,. \tag{41}$$

Both methods are compared in Table 2, revealing a discrepancy of 7,6 g. This can mainly be attributed to inaccuracies in the flue gas measurement.

Table 2: Comparison for the mass of CaO using different calculation methods

	CO_2 [g]	CaO [g]
Stoichiometry	156,2	198,8
Flue gas measurement	163,8	191,2

The bed material was further heated to 900 °C. After the heating process was concluded, fluidisation was carried out with a mixture of methane and nitrogen in (a) and (b), and with methane alone in (c).

The share of methane was increased in each interval. The test run was terminated after 3 hours. The hydrogen production in Figure 22 and 23 was adjusted to represent nitrogen free operation with flow rate (c). A maximum production of 13 g/h in (b) and 9 g/h in (c) could be observed with subsequent rapid deactivation of the catalyst. Loss of catalytic activity is also visible in in Figure 24 and 25, plotting the relative methane conversion. This is an effect that was expected and discussed in 2.1. After reaching a minimum hydrogen production of 1,3 g/h, the graph shows a linear increase in hydrogen output of 0,24 g/h per hour over the course of more than two hours until the end of the test run. This behaviour can be attributed to a self-catalytic effect of the produced carbon as also expressed in research papers (Vander Wal & Makiesse Nkiawete, 2020). In this test run, however, this effect was too weak to have a significant positive impact on hydrogen productivity. This might be attributed to the suspected low width of the carbon layer on the catalyst surface. For a high self-catalytic activity, the carbon layer presumably needs to be of considerable thickness. This theory is strengthened by the test run with iron and olivine as bed material in 5.4, where self-catalysis played a major role and the thickness of the carbon layer on the particles could be assumed to be substantially higher.

Higher hydrocarbons were present in minimal amounts of ethane and ethylene. No traces of acetylene could be measured. The measurements are depicted in Figure 26. It further shows a slight increase of the amount of ethylene over the course of the experiment, while ethane does not exhibit such behaviour.

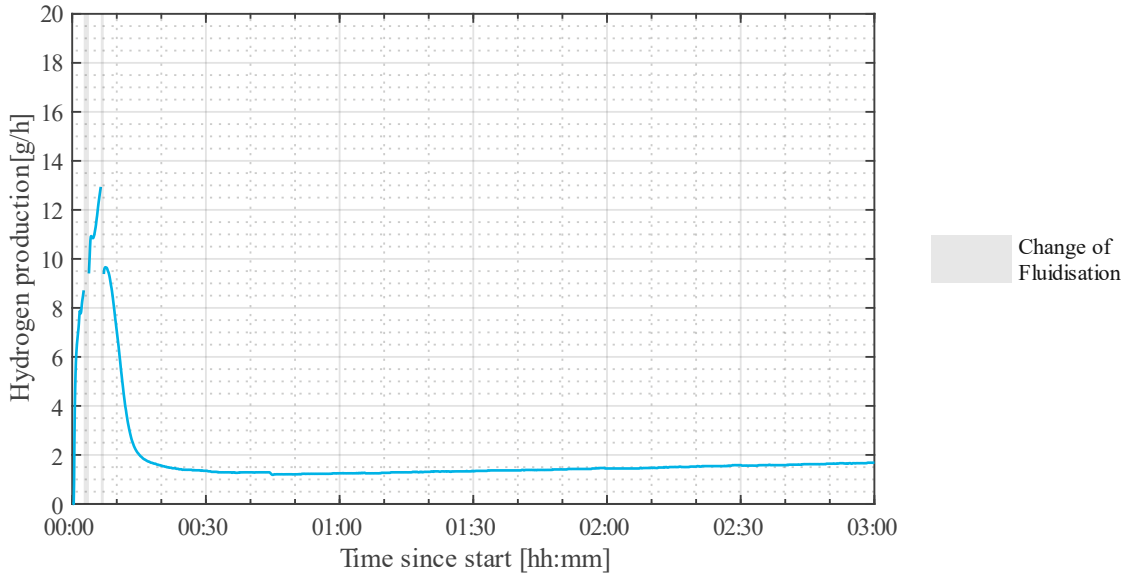

Figure 22: Hydrogen production with $CaCO_3$ as bed material simulating fluidisation (c)

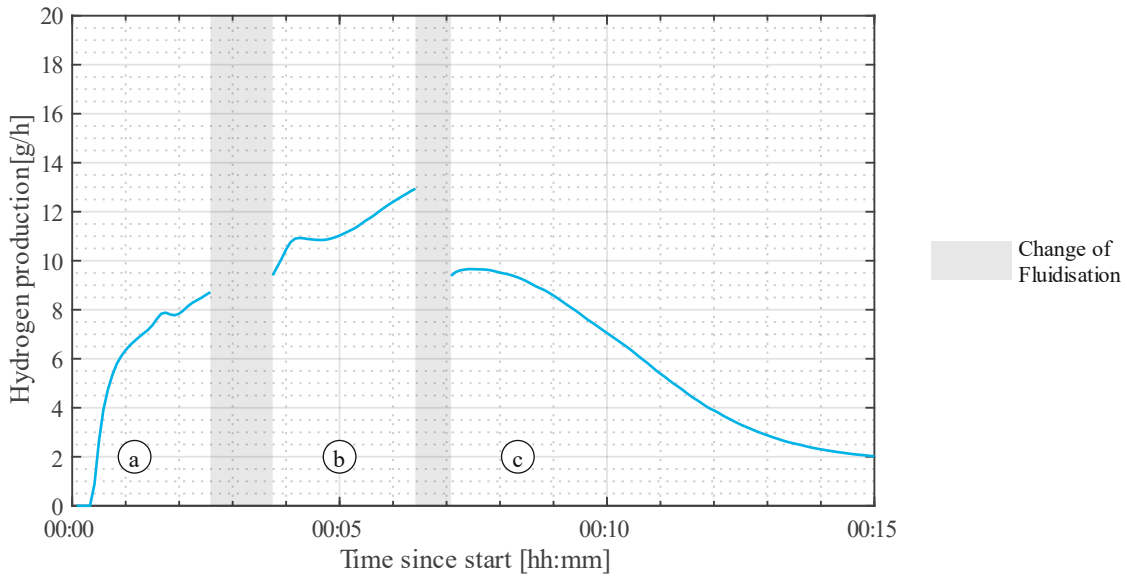

Figure 23: Hydrogen production with $CaCO_3$ as bed material simulating fluidisation (c) (detail)

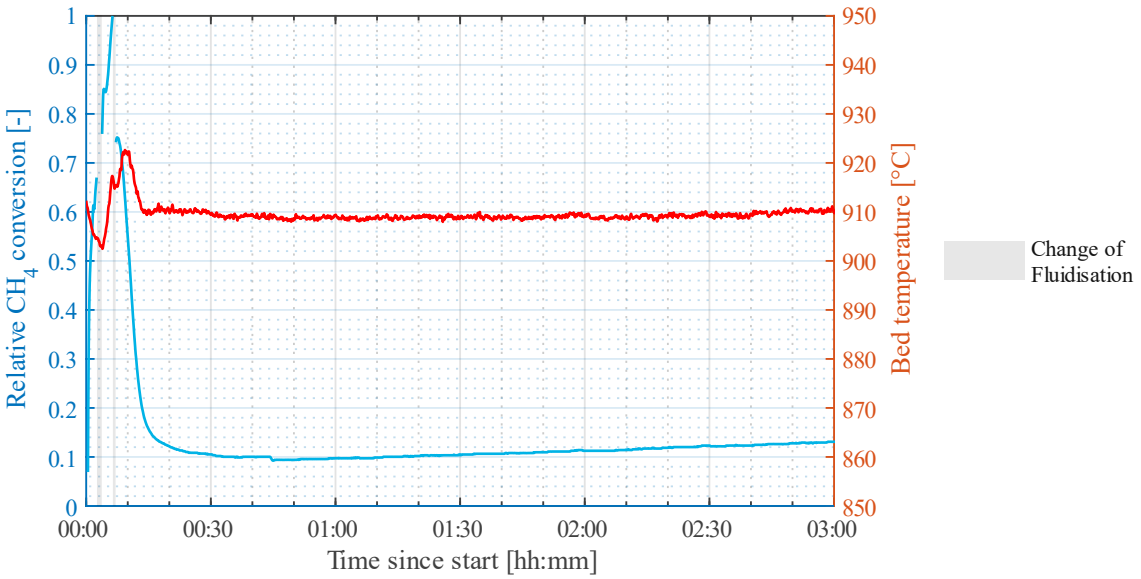

Figure 24: Relative CH_4 conversion with $CaCO_3$ as bed material

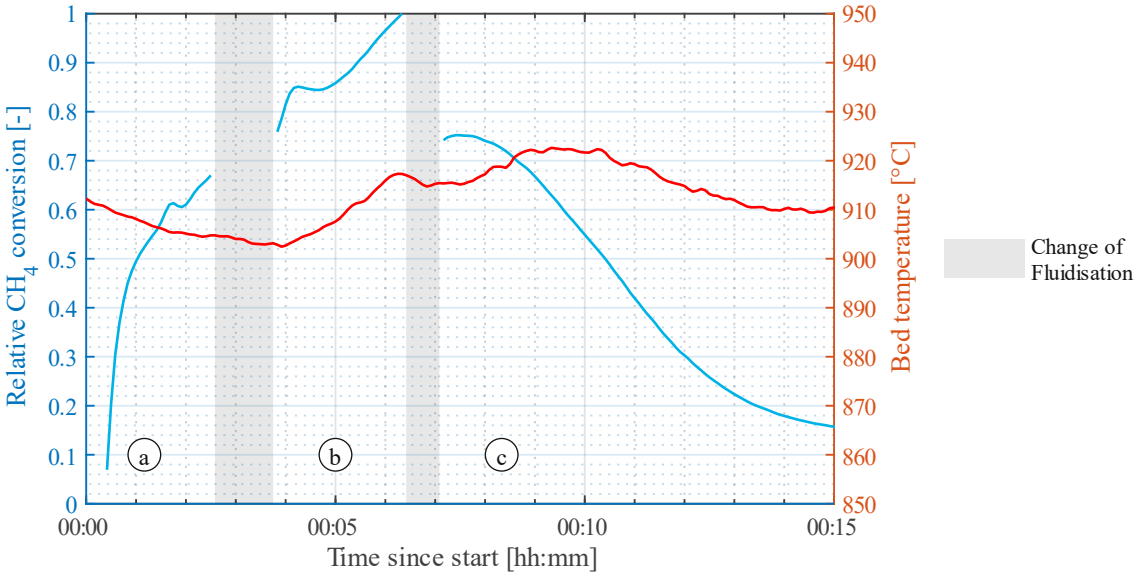

Figure 25: Relative CH_4 conversion with $CaCO_3$ as bed material (detail)

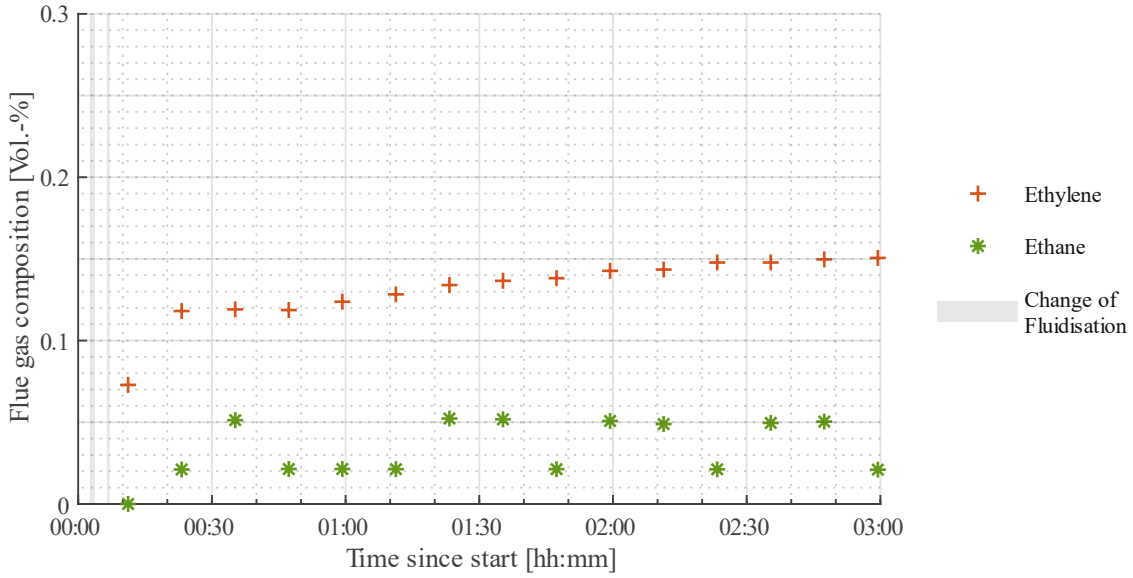

Figure 26: Higher hydrocarbons with $CaCO_3$ as bed material

The profile of the pressure drop in Figure 27 displays a slight, yet quadratic increase over the course of the experiment.

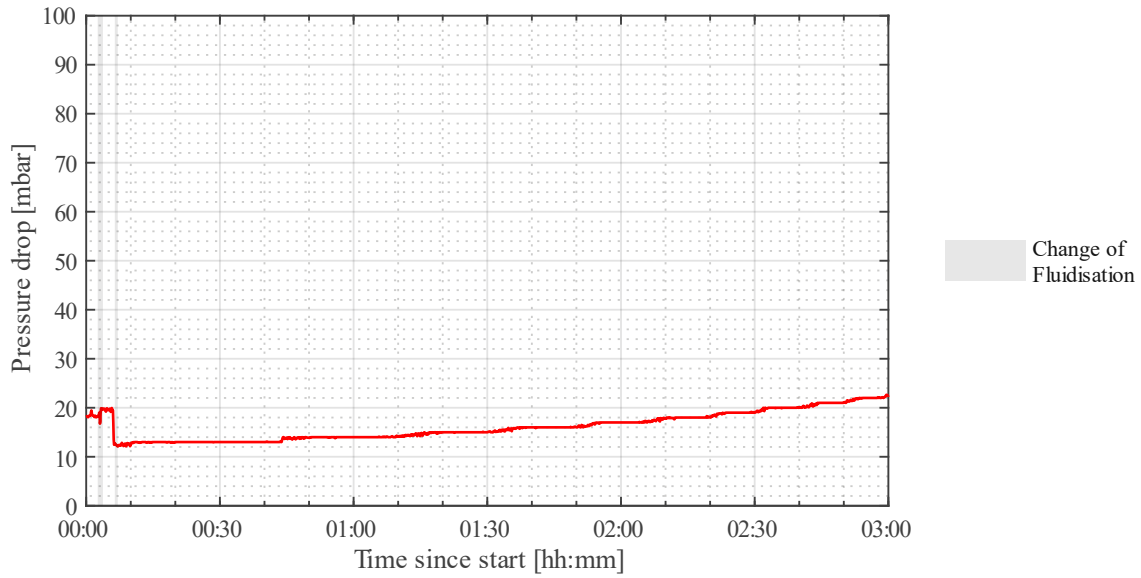

Figure 27: Pressure drop with $CaCO_3$ as bed material

The underlying reasons for the increasing pressure difference here are similar in all test runs. These are discussed in 6.1.2.The mass gain of the bed material and hydrogen production occur simultaneously. The most significant increase could – in this test run – be observed during the first 15 minutes, followed by a minimal and rather constant increase thereafter. Noting that the methane conversion – and therefore the carbon deposition on the catalyst, i.e. the mass increase – was meagre, this influence can be regarded as negligible. This perspective is corroborated comparing the mass of bed material before and after the trial. 355 g limestone were converted to 198,8 g calcium oxide. After the test run, 179,3 g of bed material including carbon deposits were retrieved. The remaining mass was entrained in the gas and separated in the downstream gravity separator and gas filters. A decreasing mass in the bed material generally has the opposite effect to the one observed. That leaves the continuous plugging of the holes in the perforated plate as the only reason for the growing pressure loss.

Figure 28 shows a higher pressure loss during phase (a) with $\Delta p \approx 18$ mbar and (b) with $\Delta p \approx 20$ mbar as compared to (c) with $\Delta p \approx 13$ mbar. In the two earlier sections, fluidisation was carried out with a nitrogen mole fraction of 75 % in (a) and 59 % in (b). At 900 C and standard pressure, the density of methane equals $\rho_g = 0{,}17$ kg/m³, the density of nitrogen equals $\rho_g = 0{,}29$ kg/m³ (Linstrom, 1997). Using (45) reveals that the main driver for the increased pressure loss is the higher overall density in these stages. The higher overall flow rate plays an additional role in (b).

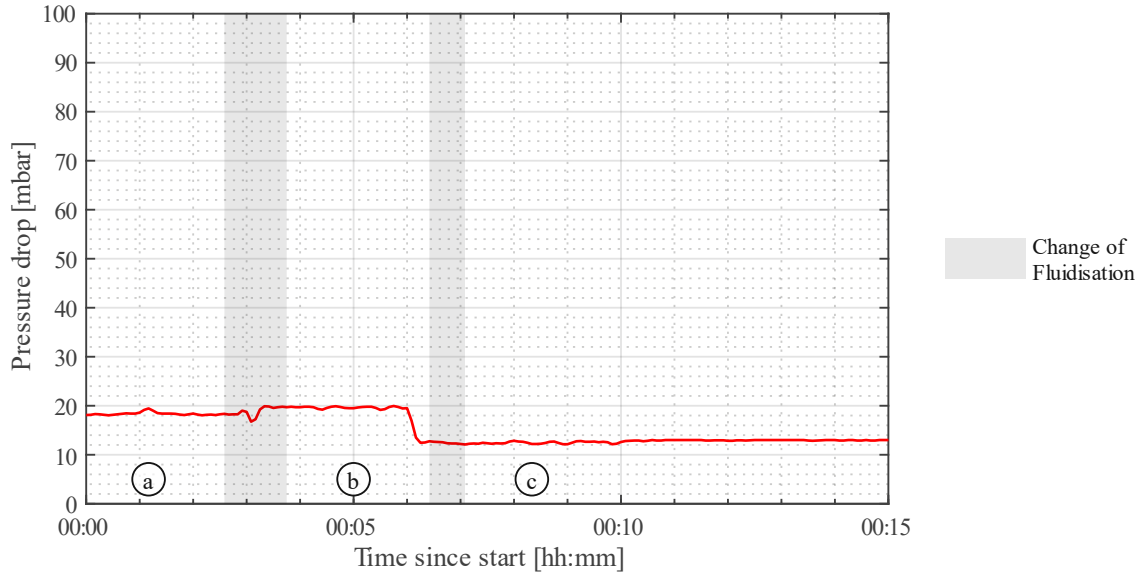

Figure 28: Pressure drop with $CaCO_3$ as bed material (detail)

The temperature profile in Figure 29 shows few saliences. The peak of the preheater temperature at minute 10 can be attributed to the sluggish control of the temperature. After reducing the gas flow rate in (c), the lower need for energy was counteracted slowly, leading to a first increasing temperature.

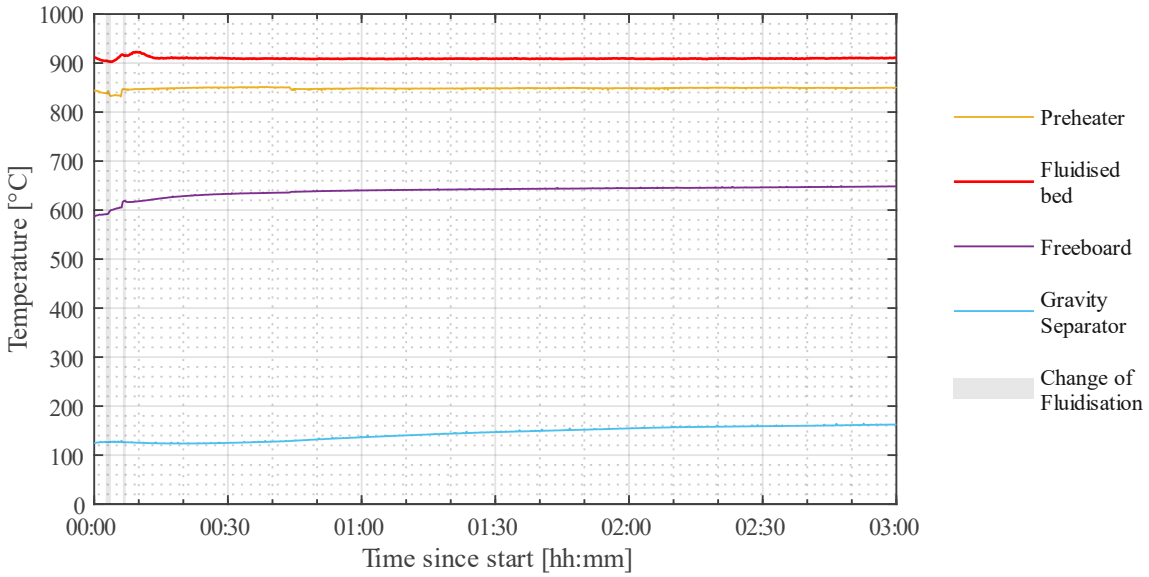

Figure 29: Temperature profile with $CaCO_3$ as bed material

5.2 Methane Pyrolysis with Activated Carbon as Bed Material

Bed material	C as activated carbon
Catalyst	C as activated carbon
U_{mf} (air, 20 °C)	130 mm/s
d_{SV}	860 µm

Table 3: Parameters AC

Figure 30: Bed material AC

AC (Figure 30) has been extensively studied in the literature (Moliner et al., 2005; Muradov et al., 2005b) and proved to have good catalytic effects, albeit followed by rapid deactivation. The catalytic activity of ACs relies heavily on its immense surface area (Abbas & Daud, 2010) and the deactivation correlates with its reduction (Muradov et al., 2005a).

In these trials, the material was prepared to have a grain size distribution ranging from approx. 300 to 600 µm, obtaining the parameters given in Table 3. Peculiar for AC compared to the other studied materials were the comparably high amounts of carbon monoxide in the flue gas during pyrolysis. This can be attributed to oxidic components in the AC that react with the produced carbon. Substantial carbon monoxide emissions were present primarily in the initial stages of the pyrolysis process, indicating that oxidic constituents were depleted from the bed material rather quickly. In later phases of the process, no significant amounts of carbon monoxide were detected.

Deactivation was caused by clogging of pores by the deposited carbon and associated loss of surface area. This causation has already been discussed in the scientific community (Abbas & Daud, 2010). AC can be reactivated by treatment with various gases as discussed in 2.1. In cases presented in this paper, steam and CO_2 regeneration was performed.

In a large-scale system, the regeneration reaction could be managed in a separate fluidised bed chamber, creating a circulating system of optimised residence times. Partial combustion of the carbon with air is exothermic and can simultaneously generate the heat required for the pyrolysis process. This comes with the drawback of emitting carbon dioxide. Applying steam, on the other hand, does not generate substantial amounts of carbon dioxide. However, considering the endothermic nature of the water–gas reaction (xiv), it requires additional energy and is incapable of providing any of the required energy for methane pyrolysis. The main advantage of using steam is the production of syngas, which can be further utilised.

5.2.1 Activated Carbon 1

Bed material	100,37 g C as activated carbon
Bed temperature	910 °C
Fluidisation during pyrolysis	89 mm/s (CH_4)
Fluidisation during reactivation	71 mm/s (CO_2)

Table 4: Parameters AC1

The first test run was carried out with the parameters presented in Table 4. The bed material was heated up to 910 °C using nitrogen as a fluidising agent. Upon reaching goal temperature levels, pyrolysis was started with a methane velocity of 89 mm/s.

The flue gas composition in Figure 31 depicts a high hydrogen yield the first 15 minutes, including a dip at minute 3, followed by a steady decline. Figure 32 corroborates this observation. After reaching an initial hydrogen output of 30 g/h, the graph rapidly drops to 25 g/h due to a plummeting bed temperature. This fall at the start of the reaction is the result of the endothermic nature of the pyrolysis reaction as well as temperature regulation that is too sluggish to counteract sufficiently. Hydrogen production subsequently increases concurrently with a rising temperature. After reaching a new peak at 29 g/h, conversion of methane decreases due to the deactivation of the applied catalyst, leading to a low yield of hydrogen of 2,3 g/h after a duration of 1:15 h.

To regenerate the spent catalyst, carbon dioxide was applied at a gas velocity of 71 mm/s for 8 minutes. Figure 31 displays an initially high reaction rate, converting up to 40% of all CO_2 to CO. The high speed of the reaction quickly decreases and approaches a low and constant rate. 42,5 g of carbon had been produced before regeneration was started, 6,36 g or 15% of which were combusted thereby

Figure 32 shows a conversion rate of 16% compared to its maximum, equalling a hydrogen output of 5,1 g/h, when the pyrolysis process was restarted. Following deactivation leads to a low hydrogen production of 2,2 g/h before terminating the test. It can therefore be concluded that the regeneration process was executed too late or over an insufficient time frame. No further regeneration cycle was carried out. A self-catalytic effect was not observed.

As depicted in Figure 33, traces of ethane and ethylene were present over the whole course of the test. A low methane conversion favoured ethylene emissions. Presumably, the same can be said for ethane, however, due to the meagre amounts emitted, this cannot be concluded with sufficient certainty.

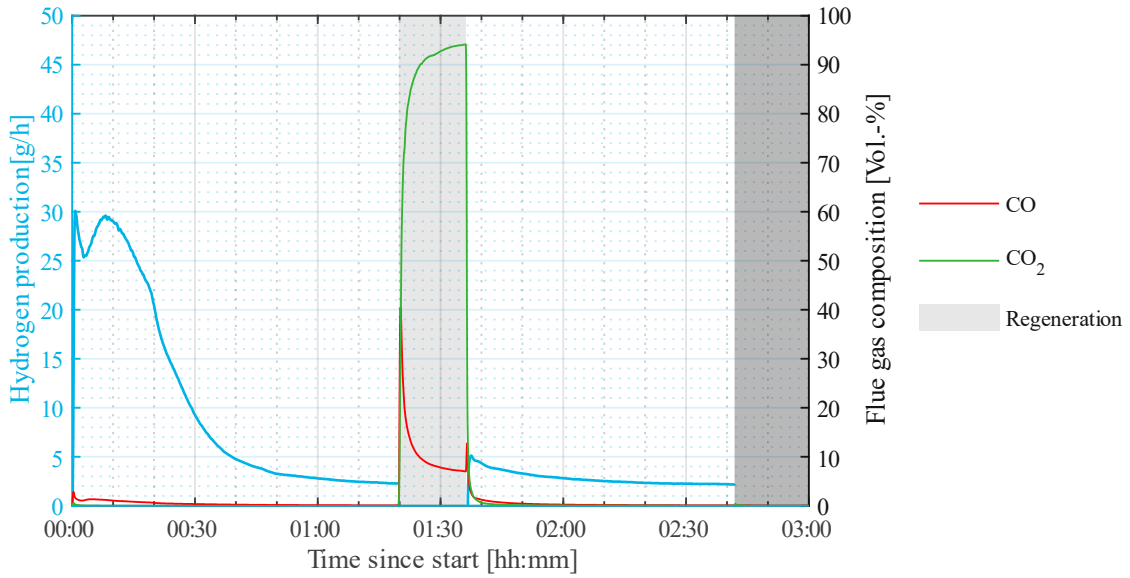

Figure 31: Hydrogen production and flue gas composition AC1

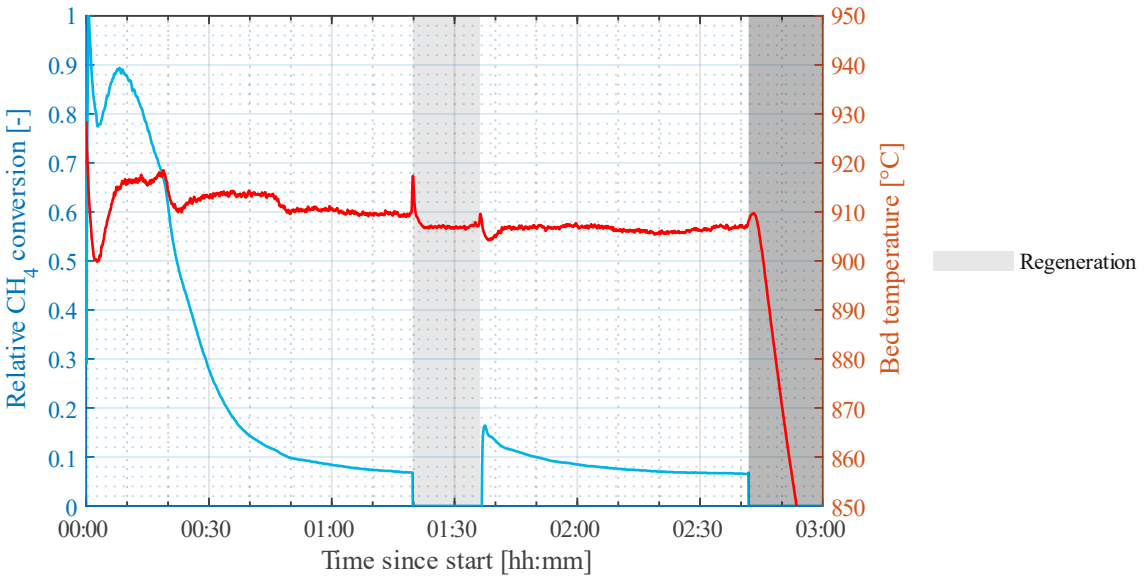

Figure 32: Relative CH_4 conversion AC1

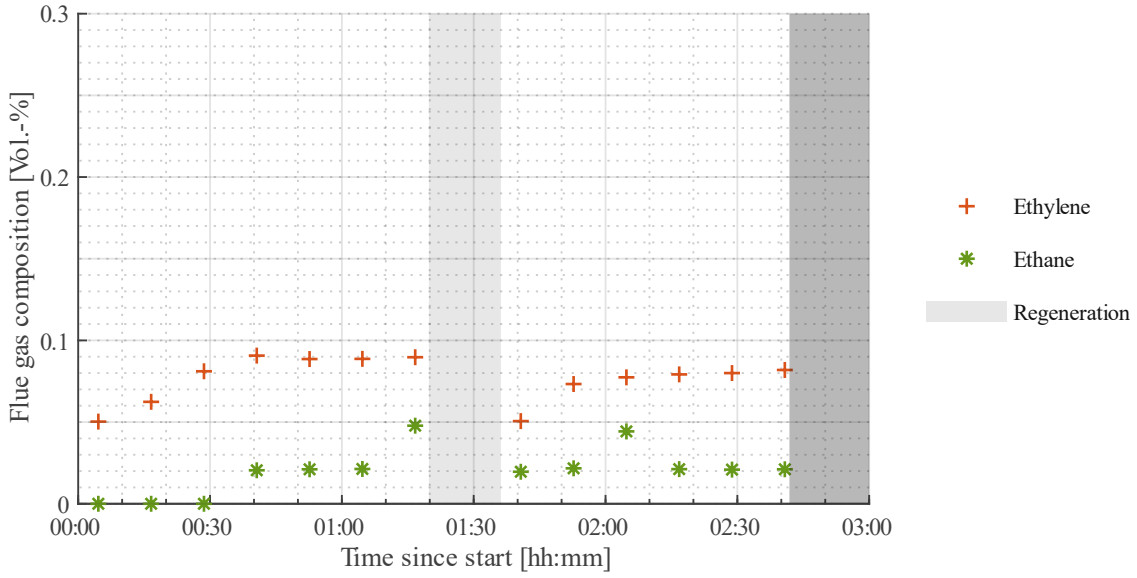

Figure 33: Higher hydrocarbons AC1

Figure 34 clearly illustrates the dip of the fluidised bed temperature immediately after the start of the pyrolysis reaction. This is caused by the endothermic nature of the reaction. In return, the cooler bed induces a lower methane conversion as seen before.

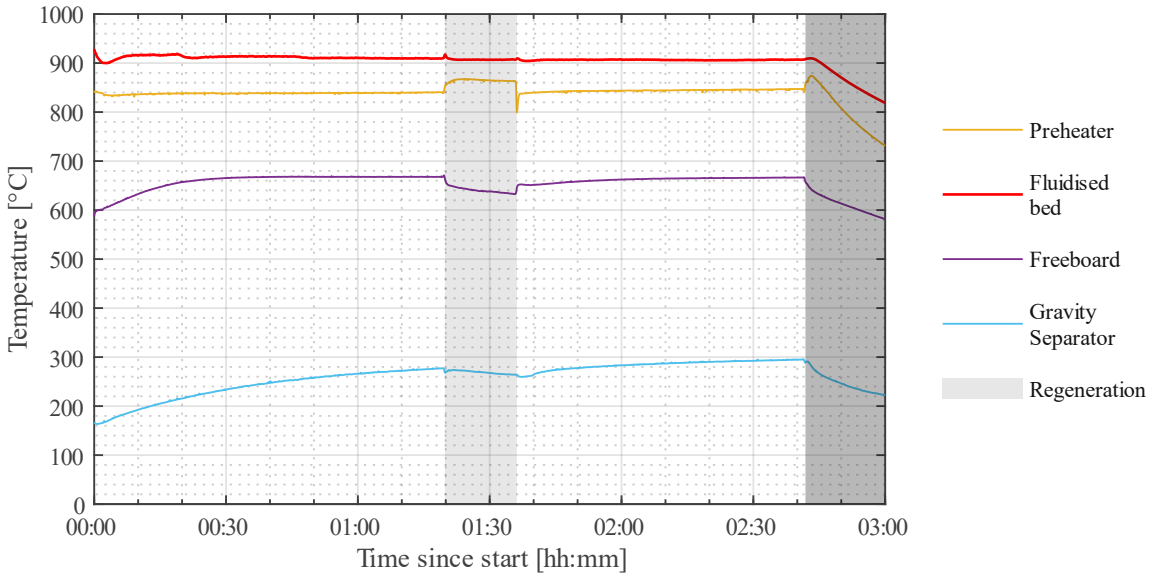

Figure 34: Temperature profile AC1

The pressure drop in Figure 35 shows a quadratic characteristic once more. The same rationale as in 6.1.2 can be employed. Gain of mass of the bed material and its influence on pressure is insignificant. The added mass of 35 g results in an additional pressure difference of 1,47 mbar, contributing to approx. 1% of the total additional pressure drop. During the regeneration process, the pressure loss decreases as a result of the combustion of parts of the carbon, potentially unplugging the holes in the perforated plate. After regeneration, the amplitude amounts to 50 mbar compared to 60 mbar before. Using carbon

dioxide as the fluidising agent during regeneration causes an overall higher pressure drop regarding its higher density compared to methane as discussed in 6.1.2.

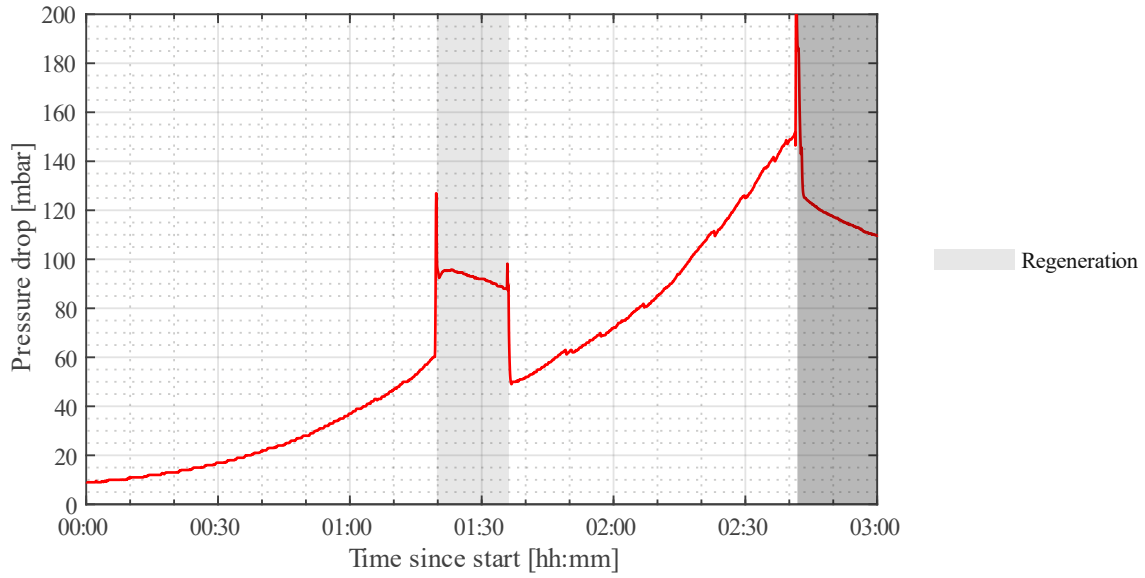

Figure 35: Pressure drop AC1

The carbon balance is summarised in Table 5. 52,57 g of carbon were produced during the trial according to flue gas measurement and a calculation as stated in 4.4. Most of the retrieved carbon – 75,9 % – could be found in the bed material. 12,8 % were burned during regeneration and 8,6 % of the carbon was deposited on reactor walls. The amount of carbon entrained in the gas flow and separated in the gravity separator or filters was minimal. Any discrepancy was within the expected range.

Table 5: Carbon balance AC1

	[g]	[%]
Total amount of carbon collected	**46,26**	**100,0**
Bed material	34,72	75,9
Regeneration	5,86	12,8
Filter pyrolysis	0,27	0,6
Filter heating/cooling	0,72	1,6
Gravity separator	0,28	0,6
Reactor walls	3,92	8,6
Carbon produced according to flue gas measurement	**52,57**	
Discrepancy	*6,82*	

5.2.2 Activated Carbon 2

Bed material	150,39 g C as activated carbon
Bed temperature	950 °C
Fluidisation during pyrolysis	71 mm/s (CH_4)

Table 6: Parameters AC2

The second test run with AC was carried out on altered parameters (Table 6) and omitting a reactivation step. A higher bed temperature of 950 °C and a lower methane velocity of 71 mm/s were put in place. The bed height was raised to 139 mm. Each of these parameter variations fosters methane conversion. Higher temperatures shift the thermodynamic equilibrium to the product side, while a lower flow rate and heightened bed imply extended residence times of the gas in the fluidised bed.

Pyrolysis operation after heating with nitrogen demonstrated similar behaviour as in AC1 was observable. The production of hydrogen reaches a maximum of 40,5 g/h as illustrated in Figure 36. Figure 37 depicts the maximum methane conversion in the first minutes, followed by a drop concurrently with bed temperature and a subsequent increase to 93% of the previous level as the temperature is restored. After ten minutes, first signs of catalyst deactivation are discernible in both figures. The deactivation rate reaches its maximum after approximately 25 minutes and then flattens out at a hydrogen output of 6 g/h. There are no indicators for a self-catalytic effect.

Similar to AC1, higher amounts of ethane and ethylene were measured when methane conversion was low. The corresponding data from the gas chromatography unit is presented in Figure 38. It shows a higher maximum amount of ethylene compared to previous tests, peaking at a share of over 0,2%.

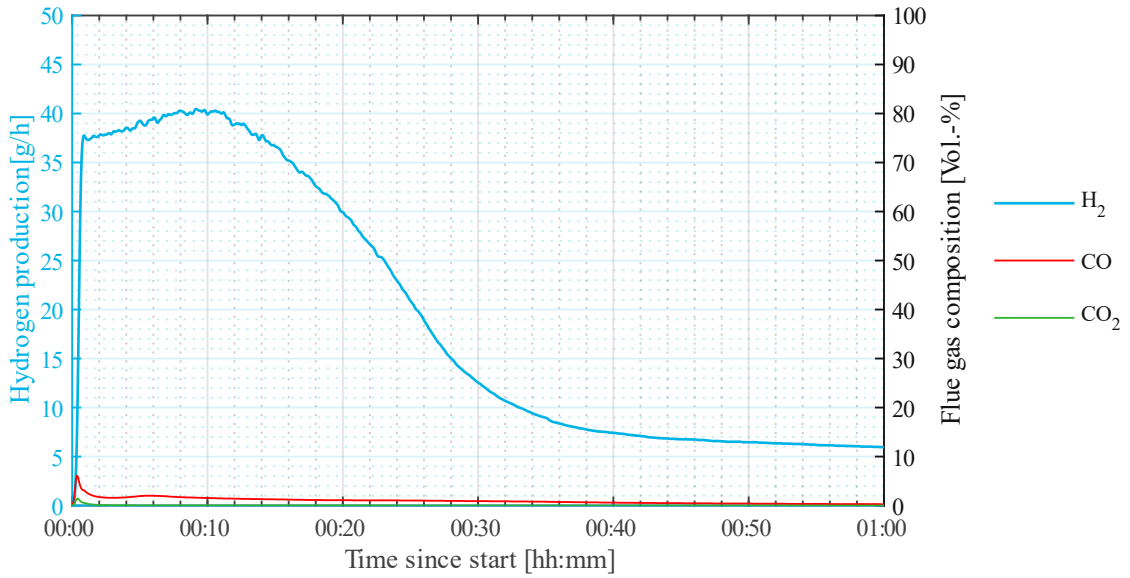

Figure 36: Hydrogen production and flue gas composition AC2

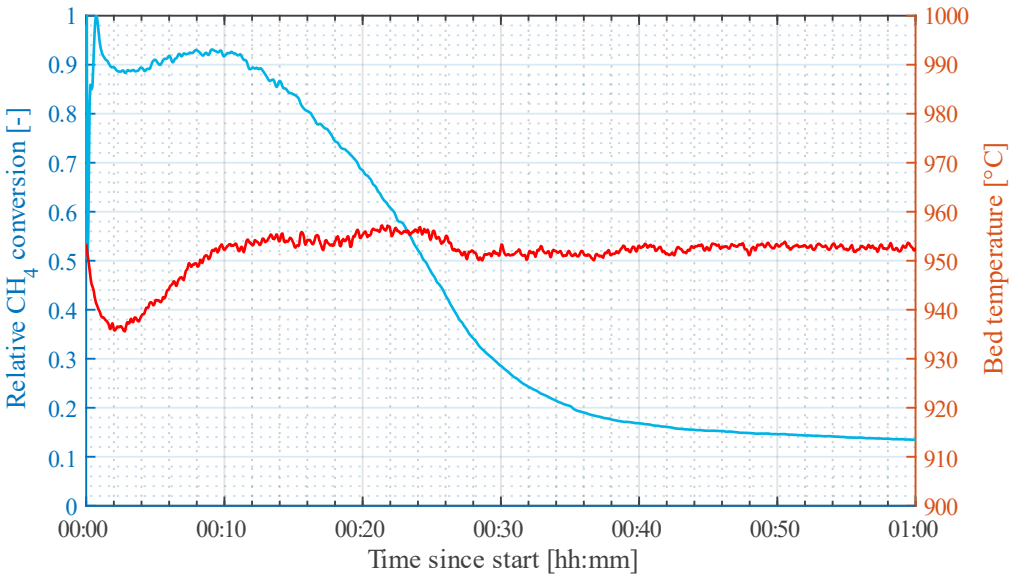

Figure 37: Relative CH_4 conversion AC2

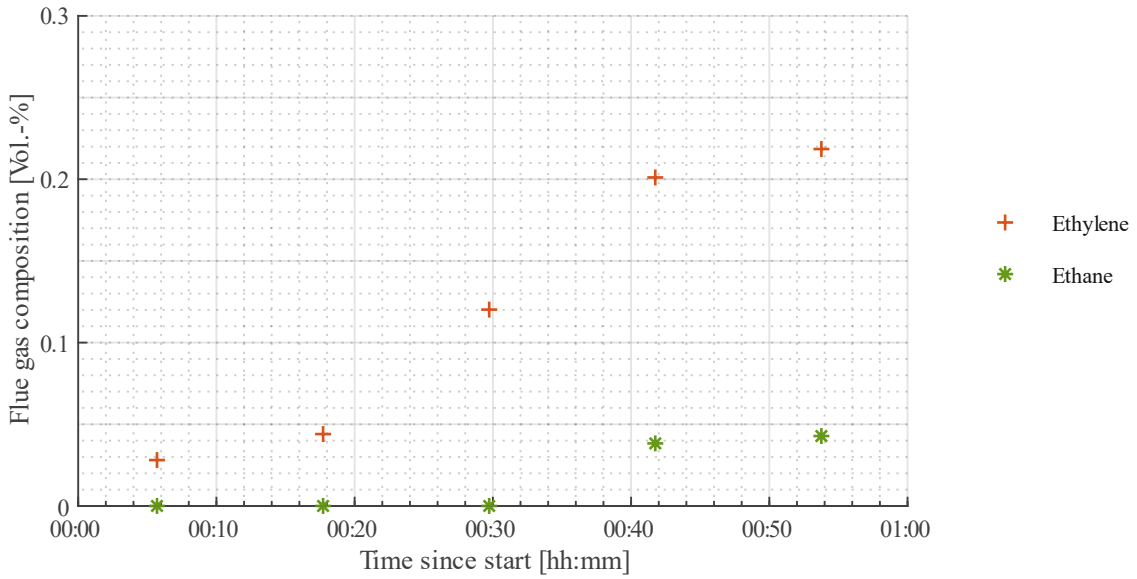

Figure 38: Higher hydrocarbons AC2

The temperature profile in Figure 39 shows regular data The initial fall of the fluidised bed temperature caused the decrease of hydrogen yield. Subsequently, constant 950 °C remained. The temperature in the freeboard and gravity separator increases over the course of the experiment. The convergence of the freeboard temperature to a constant value is distinct, reaching a maximum of 644 °C. The gravity separator, on the other hand, shows no clear signs for a flattening curve. Such a behaviour is, however, expected in longer-term experiments.

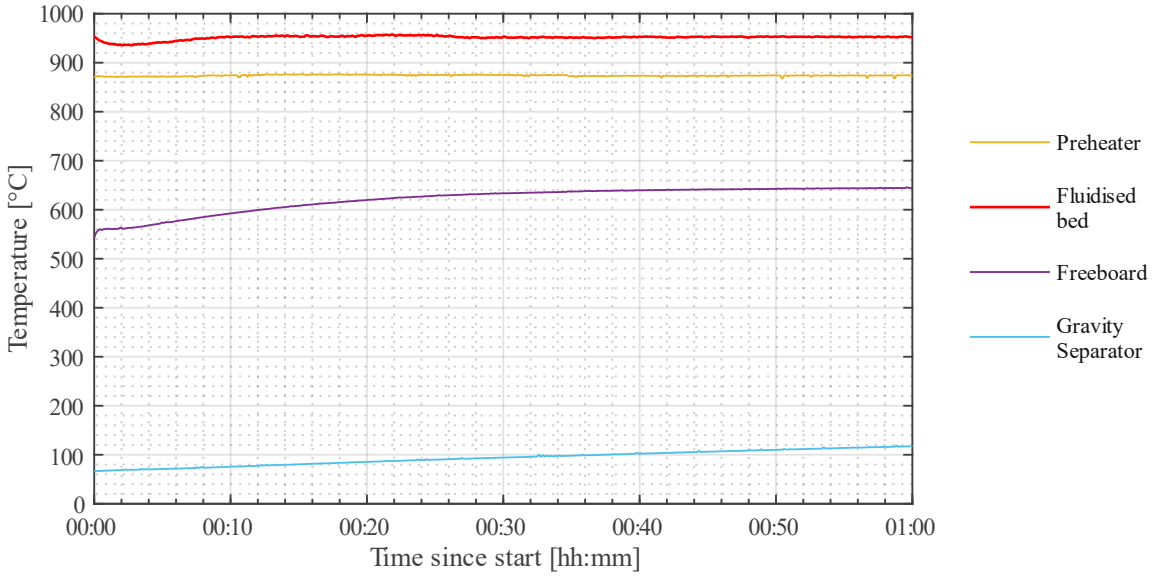

Figure 39: Temperature profile AC2

Pressure loss is illustrated in Figure 40. The graph deviates from previous experiments. Albeit also following a quadratic path in the first 30 minutes, the pressure loss later increases in a more linear manner. This cannot be attributed to an increasing mass of the bed material. Over the course of the experiment, the bed material including carbon deposits increased its mass by 42 g. Using (43), this leads to an increased pressure drop of 1,8 mbar, which is approx. 4% of the total additional pressure difference. It must also not be assumed that the plugging effect halts at one point for another effect to take its place. Rather, this behaviour can be explained by a diminishing rate at which the plugging of the perforated plate occurs and by abrasion of newly formed carbon by the moving AC particles.

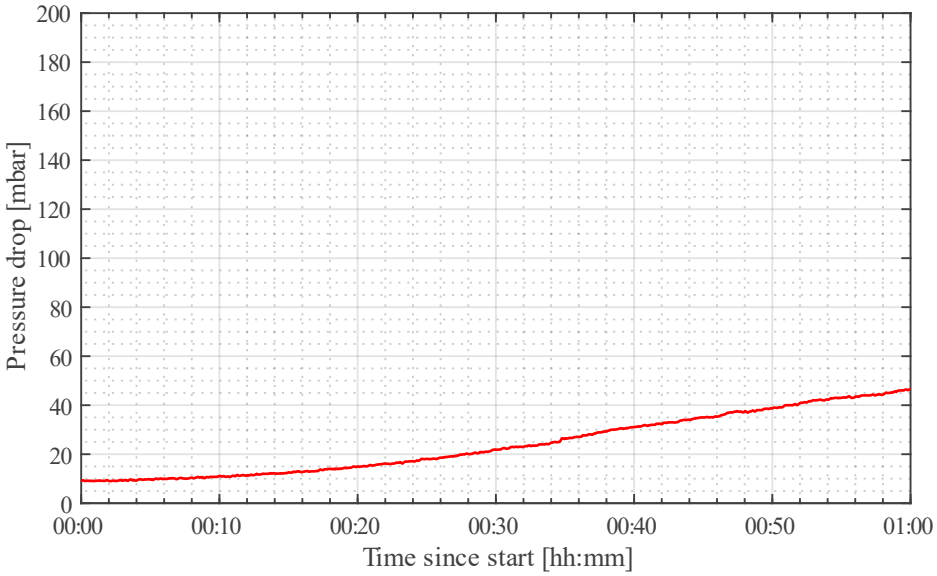

Figure 40: Pressure drop AC2

Inspecting the bed material after the trial as in Figure 41 revealed agglomeration of some of the bed material atop the distributor plate. The formed cake showed visible channels located above unblocked

holes of the plate for the gas to pass. The agglomeration indicates that the temperature used during pyrolysis locally exceeded an acceptable range for this specific bed material.

Figure 41: Bed material AC2 after trial with particle agglomerates that formed atop the distributor plate

The carbon balance is summarised in Table 7. 58,97 g of carbon were produced during the experiment according to flue gas measurement. Like in AC1, most of the formed carbon could be found in the bed material. 9% were deposited on reactor walls. The discrepancy was higher than in AC1 but still within expected boundaries.

Table 7: Carbon balance AC2

	[g]	**[%]**
Total amount of carbon collected	**47,22**	**100,0**
Bed material	42,39	89,8
Filter pyrolysis	0,09	0,2
Perforated plate	0,20	0,4
Gravity separator	0,30	0,6
Reactor walls	4,23	9,0
Carbon produced according to flue gas measurement	**58,97**	
Discrepancy	*11,76*	

5.2.3 Activated Carbon 3

Bed material	100,12 g C as activated carbon
Bed temperature	950 °C
Fluidisation during pyrolysis	89 mm/s (CH_4)
Fluidisation during regeneration	43 mm/s (50% N_2, 50% H_2O)

Table 8: Parameters AC3

The third test run with AC was performed with the parameters presented in Table 8. A mass of 100,12 g AC as bed material was used at a temperature of 950 °C and steam acted as the regenerating agent. This

has the benefit of generating syngas which can be further utilised. The chemical reactions (xii)–(xiv) were listed before. Only small amounts of CO_2 were produced via (xiii) and the water–gas shift reaction (xiv).

The pyrolysis and regeneration reactions were carried out alternately in seven-minute intervals for the first ten cycles. Thereafter, one cycle of 3 minutes regeneration and another one of 15 minutes regeneration followed. For the pyrolysis reaction, methane was applied at a velocity of 89 mm/s. Regeneration was performed with nitrogen saturated with water at a temperature of 81 °C. The saturated vapour pressure at this temperature equals 0,493 bar (Haar, Gallagher, & Kell, 1988), i.e. the gas–steam stream after saturation consists of 49,3 % water and almost doubled its molar flow rate, giving a gas velocity of approx. 43 mm/s.

Figure 42 plots the hydrogen production and flue gas composition versus time, Figure 43 the relative methane conversion rate and bed temperature during the pyrolysis cycles. The drop in hydrogen yield is distinctly visible in each interval. The initially decreasing temperature contributes largely to this phenomenon. The effect cannot be attributed to catalyst deactivation alone. This statement holds true even more when comparing these results to those of AC1 and AC2, where a similar fall in methane conversion had been detected. Quantifying and proportioning the described effects on the decreasing hydrogen output is not expedient. A more suitable approach is a direct comparison of the individual cycles, nullifying the temperature effect. Between the first and second cycle, a moderate catalytic deactivation is detectable and the hydrogen production falls from 29 g/h at the end of the first seven-minute pyrolysis interval to 25 g/h at the end of the second, marking a change of 4 g/h. Comparing cycle two to three and cycle three to four, this difference expands to 9 g/h and 5 g/h, respectively. Results are in accordance with the findings in AC1 and AC2, where the deactivation rate surged to its maximum after approx. 15 minutes. For the following pyrolysis cycles, hydrogen production rates and relative methane conversion behave almost identical. It must therefore be assumed that an equilibrium of deactivation of the catalyst during pyrolysis and reactivation during regeneration with steam has been reached.

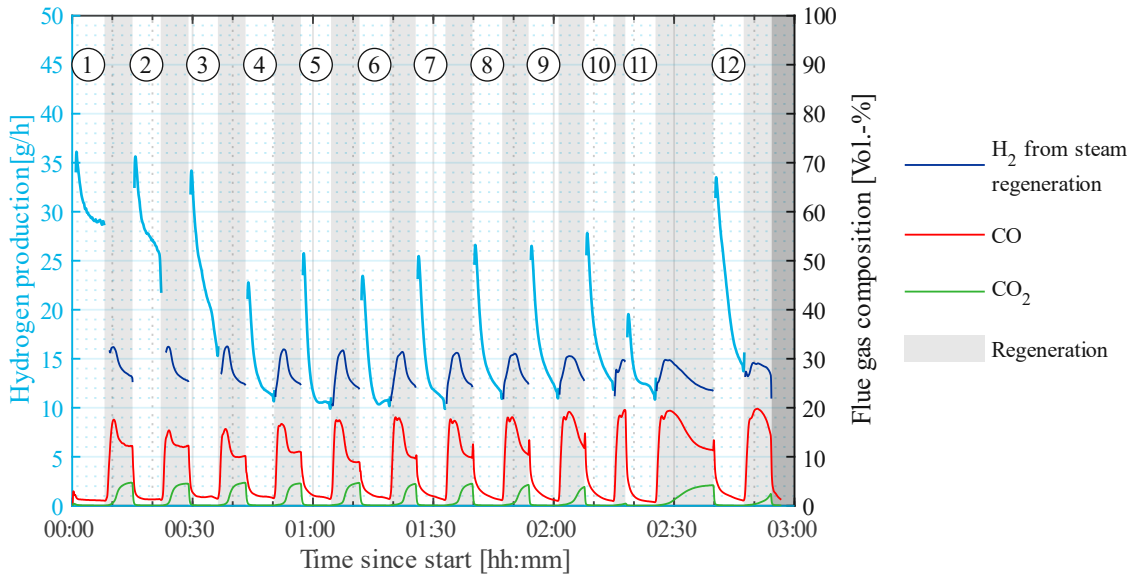

Figure 42: Hydrogen production and flue gas composition AC3

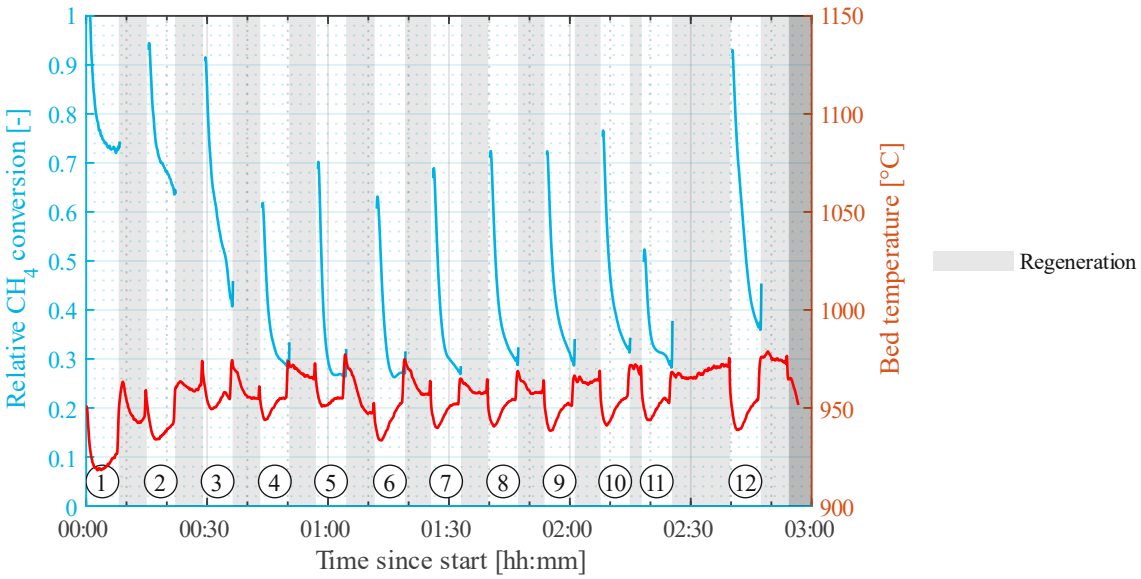

Figure 43: Relative CH_4 conversion AC3

AC deactivates due to the rapid loss of surface area. The objective of regeneration is to restore some of the lost interface. It shows that regeneration is insufficient to counteract the catalyst deactivation in the first three intervals. Examining and comparing relative methane conversion of AC3 – excluding the regeneration phases – to AC1 in Figure 44 proof that regeneration does not attenuate this process. A significant positive impact of the reactivation step can only be observed after completing the fourth pyrolysis cycle. At this point, the catalyst deactivation is fully counteracted by regeneration. In later cycles, a minor improvement of the hydrogen yield can be seen, upping the methane conversion from a minimum of 28% compared to its maximum in pyrolysis cycle five and six to a minimum of 31% in cycle ten.

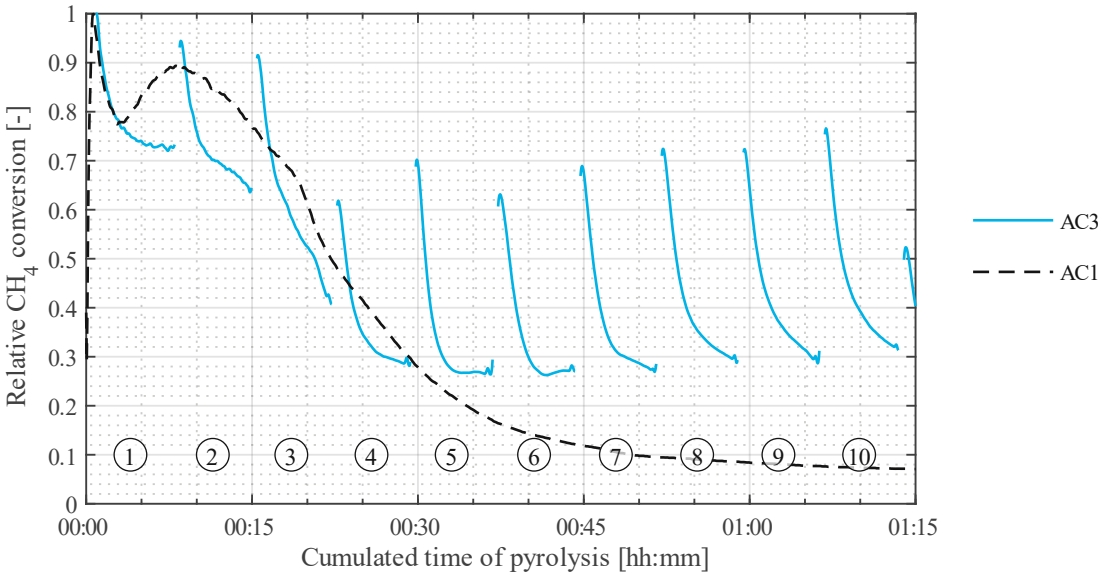

Figure 44: Relative CH_4 conversion AC3 compared to AC1

The eleventh cycle was performed after a three-minute regeneration step, impacting a reduction of the hydrogen production. Evident in Figure 42 and Figure 43, the decline is more significant at the top than the bottom of the graph, albeit affecting the whole period. The twelfth cycle was carried out after a 15-minute regeneration step, resulting in an increase of hydrogen production. Again, the change is more significant in the graph's maxima but detectable throughout. The hypothesis of a positive correlation of regeneration time and methane conversation can therefore be confirmed. Further research is required to quantify the effect as the observation does not represent an equilibrium. An equilibrium would level out after several cycles. It can, however, be stated that the conversion rate at its minimum is at least 1 pp lower for the 3-minute regeneration experiment and at least 1 pp higher for the 15-minute regeneration experiment when compared to cycle ten. Optimising the pyrolysis and regeneration times will ultimately be assessed on economic terms.

The regeneration phases can be analysed in Figure 42. From the water–gas reaction, the share of hydrogen and carbon monoxide would be expected to be identical. This is not the case for two reasons. Firstly, the hydrogen from the pyrolysis reaction does not instantly deplete, i.e. there is a latency in the system that does not allow for sharp transitions. Secondly, the water–gas shift reaction causes some of the carbon monoxide to react to carbon dioxide and hydrogen. These counteracting effects cause the shares of these components to differ. The gas composition within each cycle repeatedly shows the same behaviour. An initial peak in hydrogen and carbon monoxide production is followed by a slow decline of these products. This means, more of the water vapour reacts with carbon in the beginning of each reactivation cycle. A possible explanation is that loosely adsorbed carbon deposits react with steam and quickly deplete. The water–gas reaction then continues with stronger bound carbon from the AC itself and deposits inside the AC's pores. These are less exposed to the gas stream and thus the reaction becomes slower.

Figure 45 depicts the data measured by the gas chromatography unit. Traces of ethane and ethylene are present. The design of this experiment prevents a statement about the behaviour of higher hydrocarbon emissions over time.

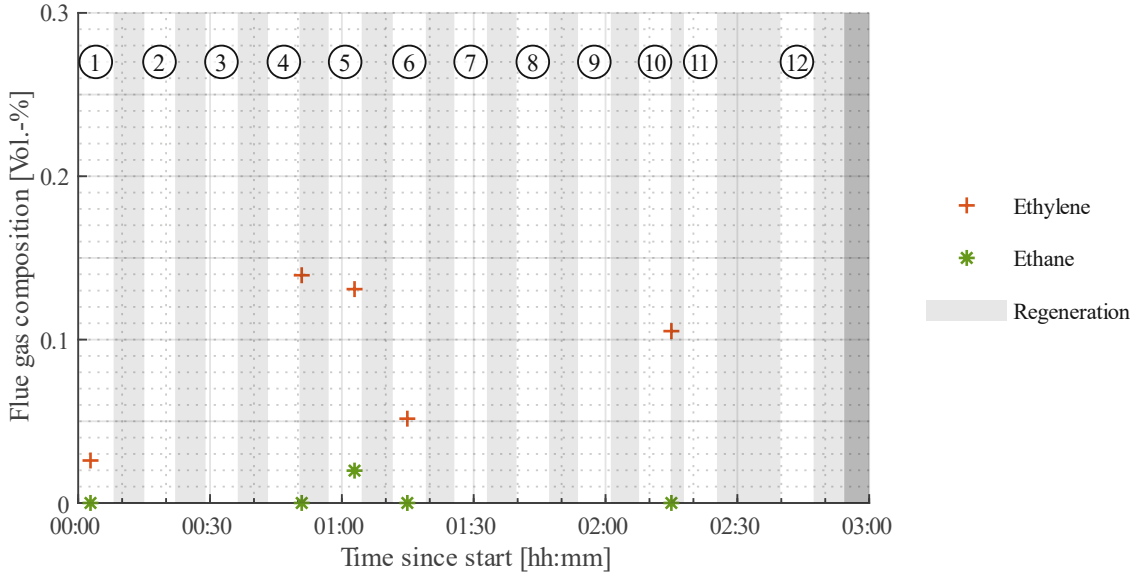

Figure 45: Higher hydrocarbons AC3

The temperature diagram in Figure 46 depicts behaviour as expected. For each pyrolysis cycle, the bed temperature shows initial decline caused by the endothermic reaction. The bed temperature rises during the regeneration process. Even though the regeneration reaction is more endothermic (131 kJ/mol vs 74,5 kJ/mol), less heat is required due to a lower gas velocity (89 mm/s CH_4 vs 43 mm/s H_2O/N_2) and lower heat capacities at 1100 K (71,8 J/(mol·K) CH_4 vs 42,5 J/(mol·K) H_2O and 33,2 J/(mol·K) N_2 (Allison, 1996)). These factors also explain ups and downs in preheater and freeboard temperatures. The temperature in the preheater is favoured by a lower flow rate and heat capacity, as it diminishes the heat exchange and requires less energy, respectively. The freeboard, on the other hand, requires high flow rates with gases with high heat capacities and a well-managed heat exchange throughout the reactor to attain high temperatures, leading to an opposing behaviour.

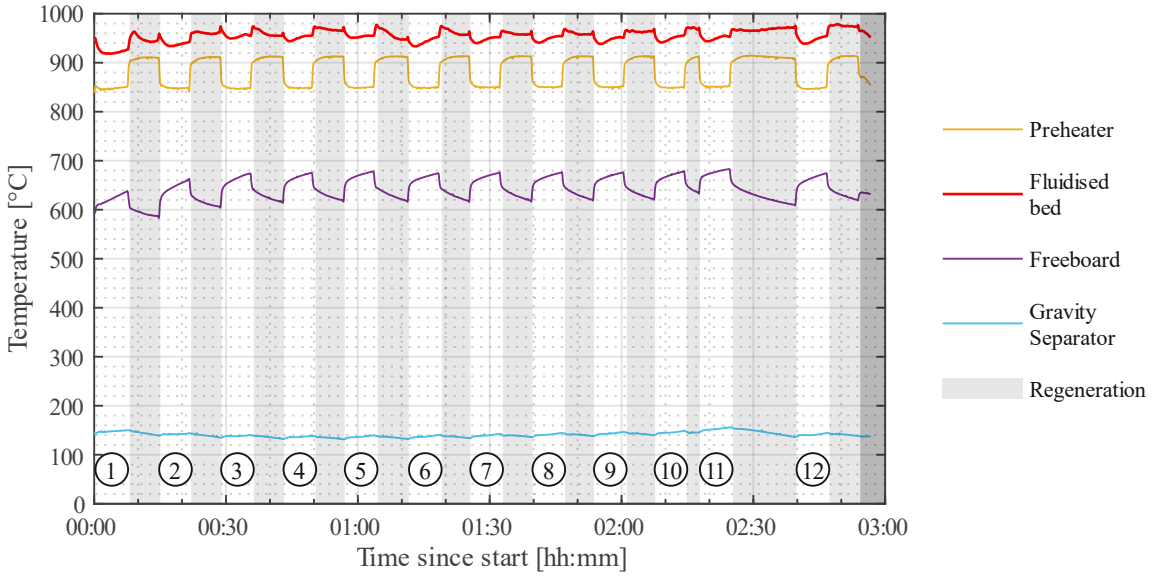

Figure 46: Temperature profile AC3

Figure 47 illustrates the pressure drop, which – overall – is monotonically increasing in an extent similar to AC1. However, the slope in any individual cycle is steeper compared to AC1. The pressure difference increases in each pyrolysis cycle from a minimum to a maximum. During the regeneration process, some of the causing effects are counteracted, which leads to the next pyrolysis step starting from a point that is well below the maximum of the previous cycle, yet higher than the prior minimum. The high gradient can be explained by effects during the regeneration cycles that favour carbon deposition in the holes of the porous plate. This hypothesis can, however, not be corroborated with specific data.

The pressure loss in Figure 47 is lower during regeneration due to the smaller flow rate. It was expected to decrease during these phases; however, the differences are – at this flow rate – too small to have a measurable impact on 7-minute regeneration cycles and are only observable during a 15-minute period. Comparing the individual cycles, a reduction of the pressure loss due to regeneration it is clearly visible. The later cycles show an equilibrium between growing loss of pressure during pyrolysis and decreasing loss of pressure during regeneration. This can be attributed to an equilibrium between the rate of carbon deposition in the holes of the distributor plate during pyrolysis and rate of carbon removal inside the holes during regeneration.

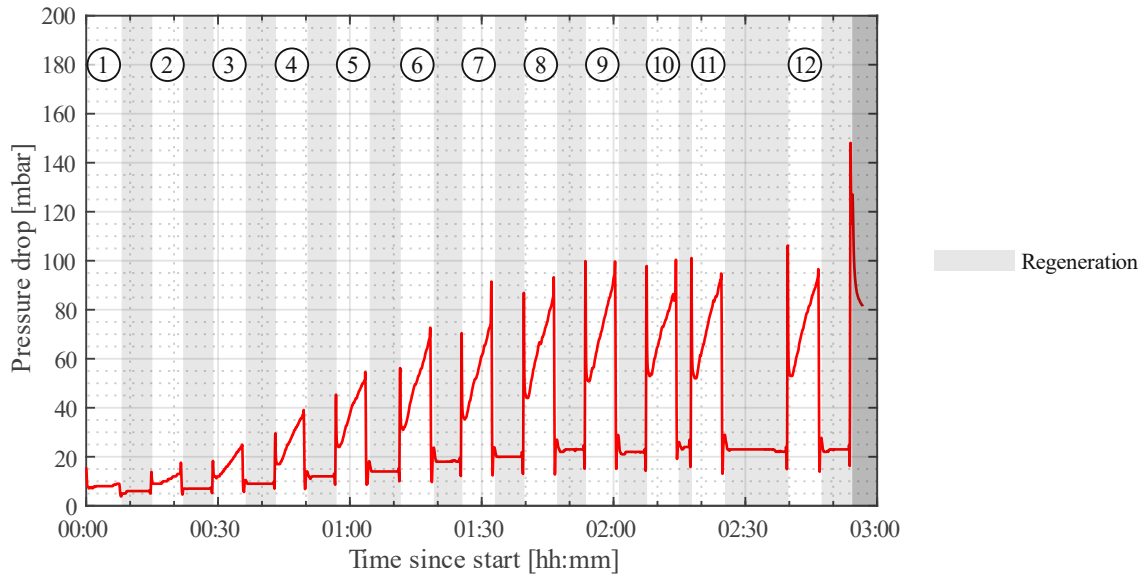

Figure 47: Pressure drop AC3

A reliable carbon balance cannot be calculated here. The number of changes in the fluidisation combined with the latency of the gas analyser unit impedes a reliable estimation of the amount of carbon produced, leading to a high discrepancy between the collected mass of carbon and the mass calculated from flue gas measuring.

5.3 Methane Pyrolysis with Ilmenite as Bed Material

Bed material	604,4 g $FeTiO_3$
Catalyst	Fe
U_{mf} (air, 20 °C)	41,2 mm/s
d_{SV}	150 µm
Bed temperature	850 °C, 800 °C
Fluidisation during pyrolysis	89 mm/s, 114 mm/s (CH_4)
Fluidisation during reduction	119 mm/s (52% N_2, 48% H_2)

Table 9: Parameters $FeTiO_3$

Figure 48: Bed material $FeTiO_3$

Ilmenite (Figure 48) must be activated to function as a catalyst for methane pyrolysis. Reduction with hydrogen produces water, iron, and titanium dioxide:

$$FeTiO_3(s) + H_2(g) \rightarrow H_2O(g) + Fe(s) + TiO_2(s)\,, \qquad (xix)$$

in which iron exhibits relevant catalytic activity, as has also been found in previous research (Konieczny, Mondal, Wiltowski, & Dydo, 2008). Therefore, the idea is to reduce the outer surface of the ilmenite particles while keeping the core intact for the structure to remain.

The parameters of this test run are presented in Table 9. Fluidised with nitrogen, ilmenite was heated to 850 °C and then reduced with a mix of nitrogen and hydrogen. Adding nitrogen to the reduction process was necessary to obtain an exhaust gas with a low water content, preventing condensation at undesirable sites. This process was performed for 30 minutes.

The partial reduction of the bed material is accompanied with a loss in mass. Estimation of the extent of this reduction is done by introducing stoichiometric relations. The final equation is:

$$m_{loss} = m_O = \left(\dot{n}_{H_2,in} - \frac{x_{H_2,out}}{x_{N_2}} \cdot \dot{n}_{N_2} \right) \cdot \Delta t \cdot M_O \, . \qquad (42)$$

Its derivation can be found in the Annex.

Over the course of the experiment, including immediately after completing the reduction process, fluidisation showed to be problematic. Loss of fluidisation manifested itself in a first slow and then sudden drop in pressure. Presumably, this was due to coagulation effects. Iron is soft at elevated temperatures and tends to adhere to other particles, upping the particle size and eventually creating a cake. Bigger particles require a higher U_{mf}, as soon as U_{mf} surpasses U_0, no more fluidisation is possible, and a fixed bed remains. This hypothesis was corroborated by investigation of the bed material after the trial, where parts of a porous cake were clearly present. Fluidisation would supposedly have been improved by diluting the bed material with cheap, catalytically less active or inactive components, such as olivine, or by shortening the reduction time. Dilution is preferable, as the latter would lead to less catalytically active iron being produced, diminishing methane conversion.

During the trial, these coagulation effects were partially counteracted by reducing the bed temperature from 850 °C during the first 15 minutes to below 800 °C, and by increasing the methane velocity from 89 mm/s during the first 30 minutes to 114 mm/s. Fluidisation could also be restored introducing mechanical forces to the reactor.

Figure 49 shows an overall low hydrogen production. Fluidising with methane at a velocity of 89 mm/s at 850 °C yielded 5–7 g H_2 per hour. Maximum methane conversion as in Figure 50 was achieved at this temperature shortly before a defluidisation occurrence. At 790–800 °C, the conversion rate reduces to 30–40% of its maximum, corresponding to a hydrogen output of 2,5–4 g/h. The spikes in these graphs are caused by short-term changes in the fluidisation properties and are not representative. A slight increase in methane conversion and hydrogen yield can be seen in the first 15 minutes of the pyrolysis reaction and again in the period from minute 34 to minute 47 because of a marginally rising temperature.

No higher hydrocarbons could be detected via gas chromatography measurements over the whole course of the experiment.

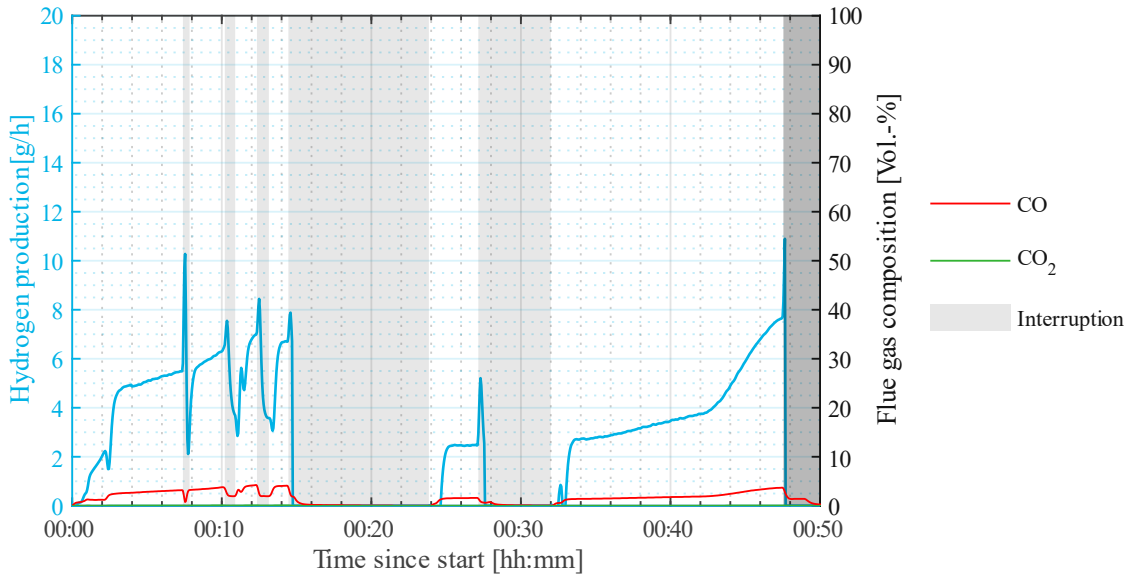

Figure 49: Hydrogen production and flue gas composition with $FeTiO_3$ as bed material

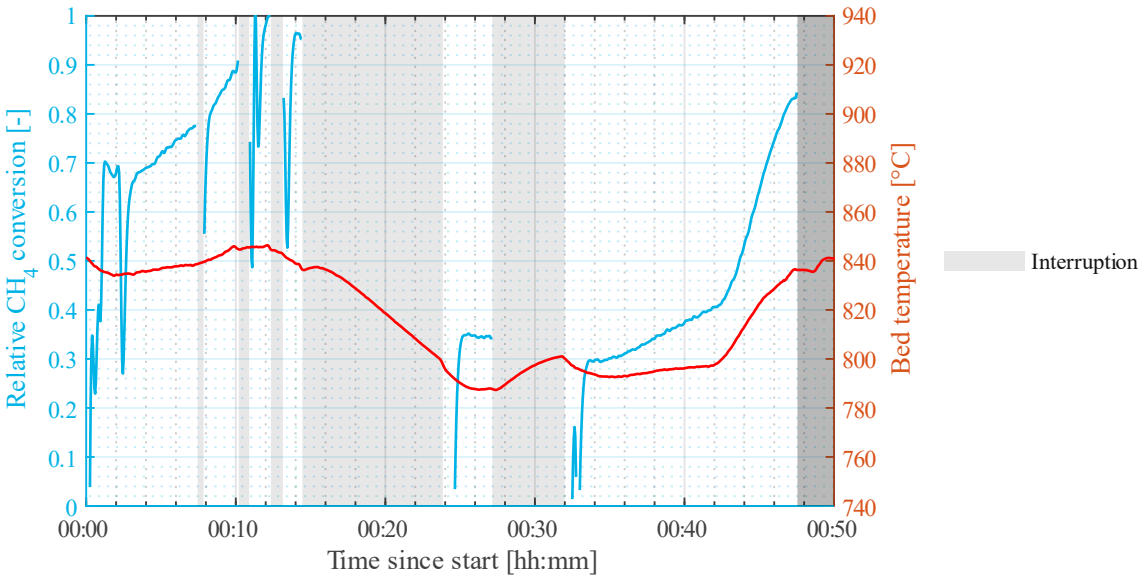

Figure 50: Relative CH_4 conversion with $FeTiO_3$ as bed material

Next to hydrogen, small amounts of carbon monoxide were measured. The CO and H_2-curves in Figure 49 correlate. Hypothetically, methane can reduce the ilmenite further, setting oxygen free, and reacting further to carbon monoxide with deposited carbon.

The temperature profile in Figure 51 depicts irregularities at times of disruption, i.e. when fluidisation ceases. Specifically, the preheater temperature is higher during interruption phases one and two and lower during phases three and four. The freeboard shows an opposing behaviour.

During interruption one and two, nitrogen was added to the fluidisation, leading to an overall higher volumetric flow rate and a higher fluidisation number. The added nitrogen requires additional energy to heat, the higher volumetric flow rate fosters the heat exchange throughout the reactor. Both factors influence the preheater temperature negatively, while the higher heat exchange has a positive impact on the freeboard temperature.

During interruption three and four, nitrogen was used as the only fluidising agent at a velocity of 93 mm/s. That is 4 mm/s higher than the methane velocity before disruption three and 21 mm/s less than the gas velocity used thereafter. Combined with the smaller heat capacity of nitrogen, less energy is required to heat the gas and the overall heat exchange is smaller, facilitating both a high preheater temperature and a low temperature in the freeboard.

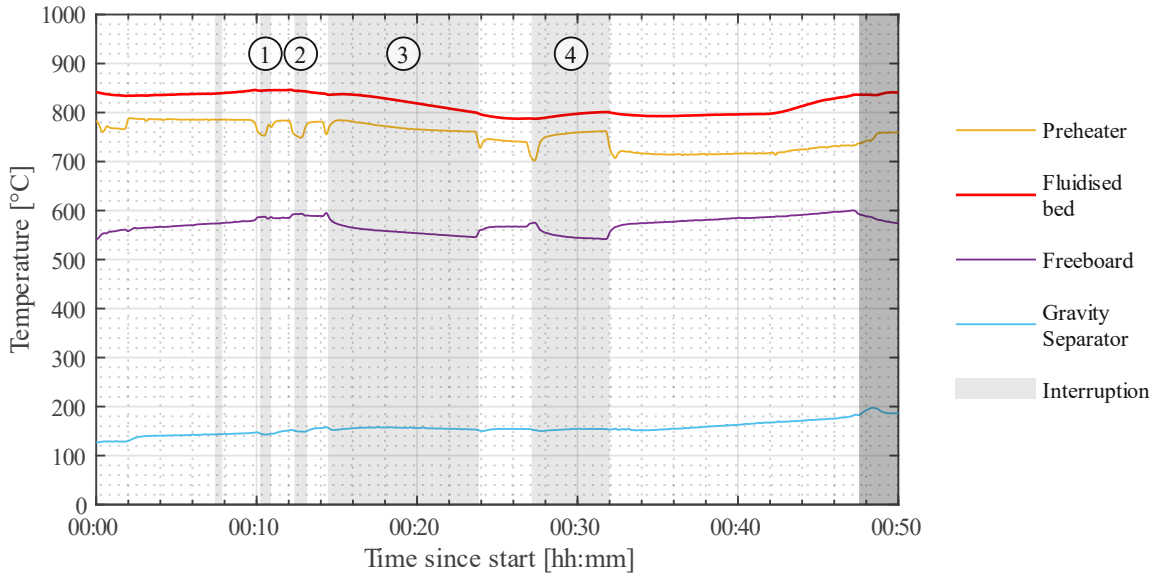

Figure 51: Temperature profile with $FeTiO_3$ as bed material

Figure 52 clearly shows the fluidisation problems that were present throughout the trial. At all times during pyrolysis, the pressure drop decreases, first slowly and then at an ever increasing pace. This indicates that particles first coagulate gradually until they reach a critical size at which U_{mf} surpasses U_0 and the fluidised bed shifts to a fixed bed. The lower temperature and higher flow rate in the last part of the test run do not inhibit these coagulation effects with the subsequent fluidisation problems, however, they mitigate them. The lower temperature potentially reduces the rate at which particles adhere to one another, the higher flow rate increases U_0 and thus the grain size at which fluidisation stops.

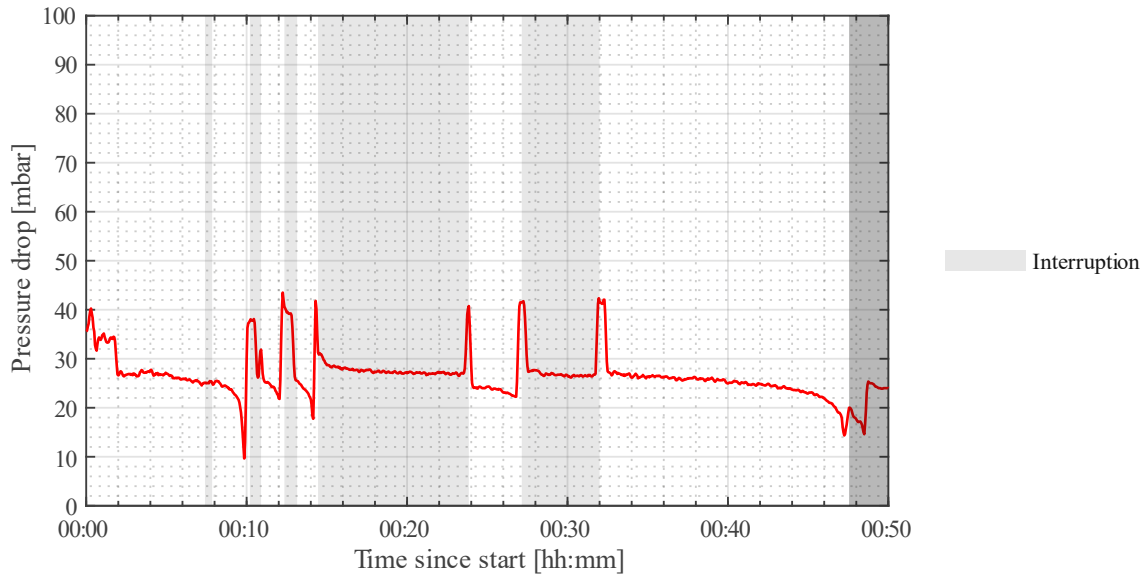

Figure 52: Pressure drop with $FeTiO_3$ as bed material

5.4 Methane Pyrolysis with Iron and Olivine as Bed Material

Bed material	Fe-powder, Olivine
Catalyst	Fe
U_{mf} (air, 20 °C)	98,8 mm/s
d_{SV}	196 µm

Table 10: Parameters Iron-Olivine

Figure 53: Bed material Iron-Olivine

This experiment applies iron directly as a catalyst with parameters from Table 10. This way, there is no need for activation. Olivine acts as a dilutant to foster fluidisation properties and prevent coagulation effects. In these trials, iron powder was mixed with olivine in a ratio of 72 wt% iron and 28 wt% olivine, corresponding to a volumetric ratio of approx. 50:50 as depicted in Figure 53. In the first half of trial Iron-Olivine 1, a greater share of olivine was used. This was part of a cautious approach, slowly testing the limits of this bed material in terms of fluidisation properties. In part (c) of Iron-Olivine 2, the proportion of iron was higher to further boost methane conversion and examine if a higher share is acceptable.

Test runs of this bed material showed significant self-catalytic properties. The discussed characteristic potentially makes iron-olivine mixtures one of the most profitable from an economic viewpoint.

5.4.1 Iron-Olivine 1

Bed material	(a) 514,3 g Fe-powder, 301,8 g Olivine (b) 768,5 g Fe-powder, 301,8 g Olivine
Bed temperature	(a) 650 °C, 750 °C, 830 °C, 900 °C (b) 950 °C
Fluidisation during pyrolysis	71 mm/s (CH_4)

Table 11: Parameters Iron-Olivine 1

The test run with parameters from Table 11 was divided into two main sections. In part (a), methane pyrolysis was carried out in short intervals at increasingly higher temperatures from 650 °C to 900 °C, with iron powder and olivine mixed in a ratio of 63 wt% to 37 wt%. In section (b), the pyrolysis reaction was observed over a longer period at a temperature of 950 °C, adding further iron to the bed material to obtain an iron–olivine ratio of 72 wt% to 28 wt%. Considering the respective densities, this corresponds to a volumetric ratio of approx. 50:50. This cautious approach with sectional heating and great dilution at the beginning tried to minimise the risk of coagulation.

The temperature dependence of the pyrolysis reaction is very pronounced in the first parts of the test run. Figure 54 and Figure 55 show a hydrogen production of 7 g/h at 650 °C, corresponding to 16% of the maximum conversion rate observed in this test. The hydrogen yield reaches 36 g/h at a temperature of 900 °C, 72% of the maximum. Anew, rapid deactivation of the catalyst is evident throughout part (a). The deactivation of the catalyst continues in (b), and the relative conversion rate bottoms at 42%. A steady increase of the hydrogen yield over the course of more than two hours follows. The curve flattens out at a production of 55 g/h. This behaviour must be attributed to a self-catalytic effect of the formed carbon.

Marginal amounts of CO and CO_2 are emitted in the initial phases of the experiment. The oxygen necessary for this reaction can be found in traces in olivine. These emissions cease when all oxygen is depleted.

The emissions of higher hydrocarbons such as ethane and ethylene were limited. According to Figure 56, most samples do not contain detectable amounts of these substances.

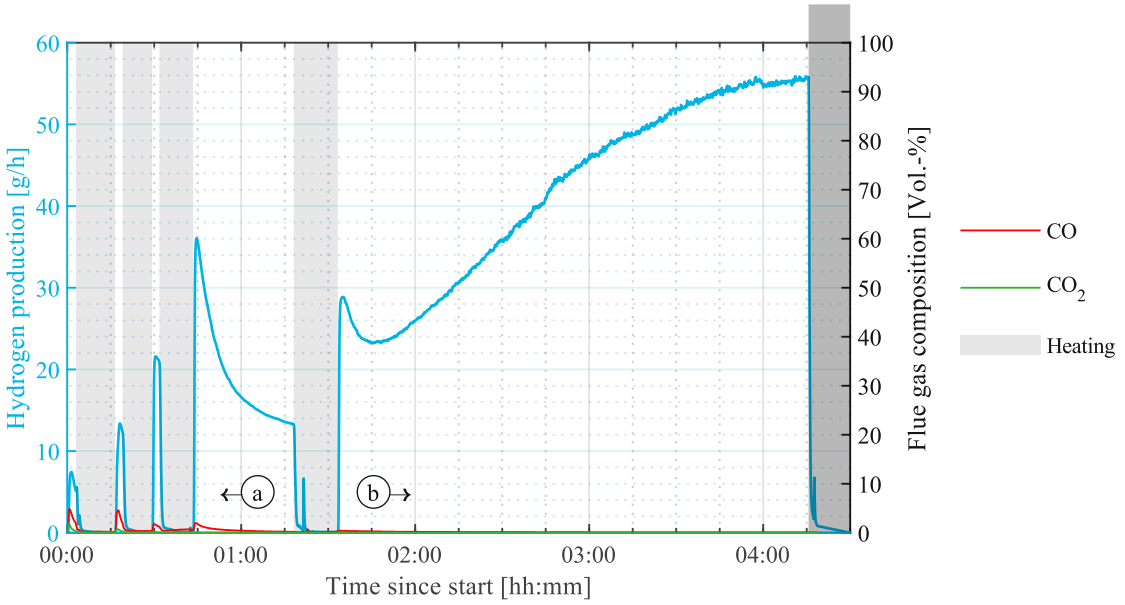

Figure 54: Hydrogen production and flue gas composition, Iron-Olivine 1

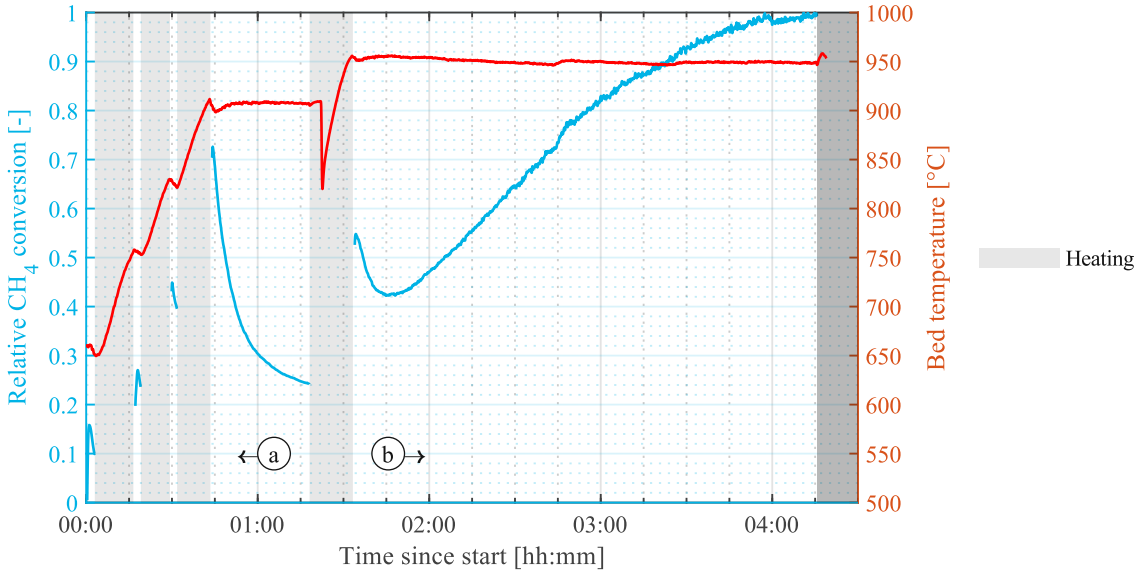

Figure 55: Relative CH_4 conversion, Iron-Olivine 1

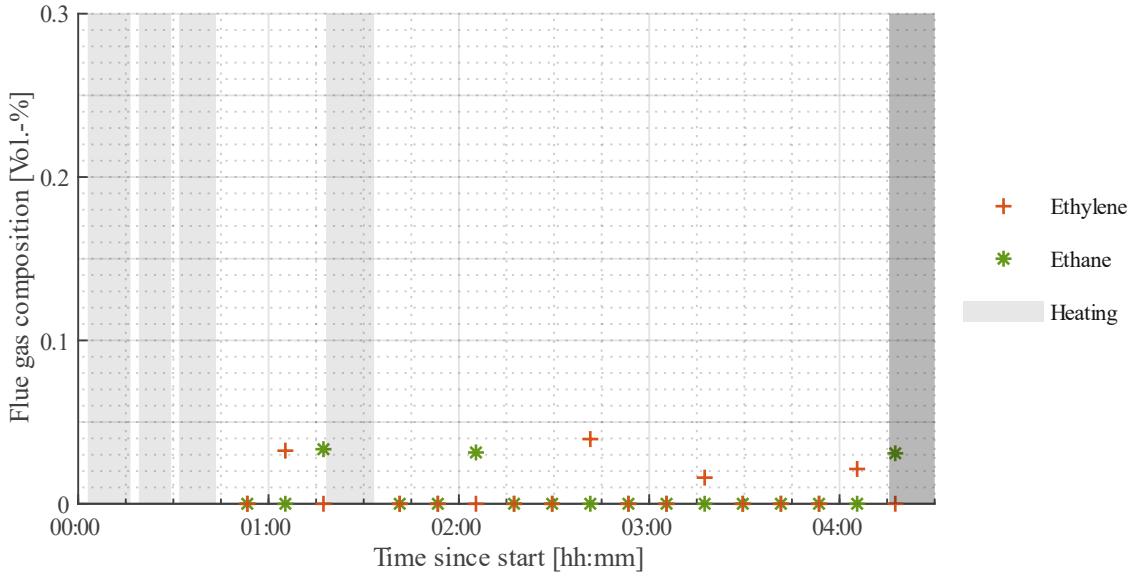

Figure 56: Higher hydrocarbons Iron-Olivine 1

An initial decrease of the bed temperature at each start of the pyrolysis process is clearly visible in Figure 57. The extend of this change is in the range of 10 °C and is counteracted within minutes. The preheater and freeboard experience lower temperatures during the heating phases as compared to the pyrolysis phases. Heating is carried out with nitrogen at a velocity of 89 mm/s, pyrolysis with methane at a velocity of 71 mm/s. At 1100 K, the heat capacity of N_2 is $C_p^0 = 33{,}2$ J/(mol·K) compared to $C_p^0 = 71{,}8$ J/(mol·K) for CH_4 (Allison, 1996), which – at a constant flow rate – leads to a lower heat exchange with the downstream parts of the reactor. A higher flow rate fosters heat exchange, however, the difference in this case is too low to compensate for the differences in the heat capacities, causing a lower temperature in the freeboard while fluidising with nitrogen.

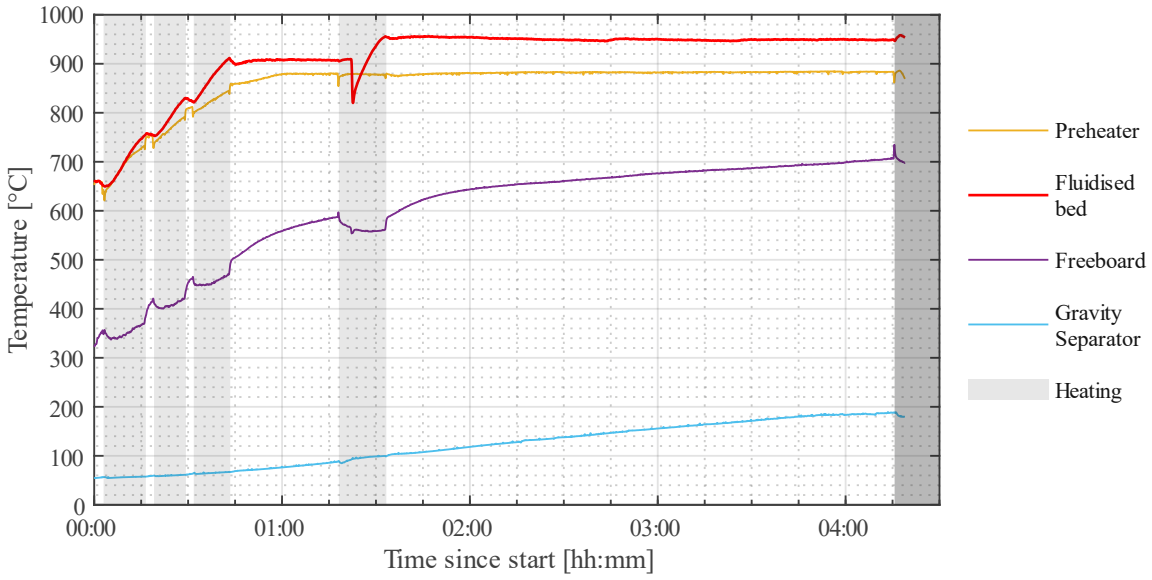

Figure 57: Temperature profile, Iron-Olivine 1

Contrary to previous experiments, the pressure drop in Figure 58 does not increase in the form of a quadratic function. Instead, it resembles a more linear, yet somewhat irregular increase. Closer inspection of the bed material after the trial reveals that the bulk density decreased from 2,22 g/cm³ to 1,48 g/cm³, indicating substantial amounts of low-density carbon on the high-density bed material. The minimal fluidisation velocity decreased from 99 mm/s to 70 mm/s. This can be caused by a declining particle density and a declining d_{SV}, both presumably playing a role here. Considering that substantial amounts of iron can be found in the container aft the cyclone, it must be suspected that the iron particles broke into pieces, partially small enough to be entrained in the gas stream. It is also likely that iron carbide was formed during the process as mentioned by Avdeeva et al. (2002) citing a Russian paper by Veselov, Levanyuk, Pilinenko, & Meshenko (1977). Another possible effect counteracting a quadratic increase is the abrasion of deposited carbon. Considering the small particle sizes, abrasion is possible in much deeper areas of the holes in the perforated plate.

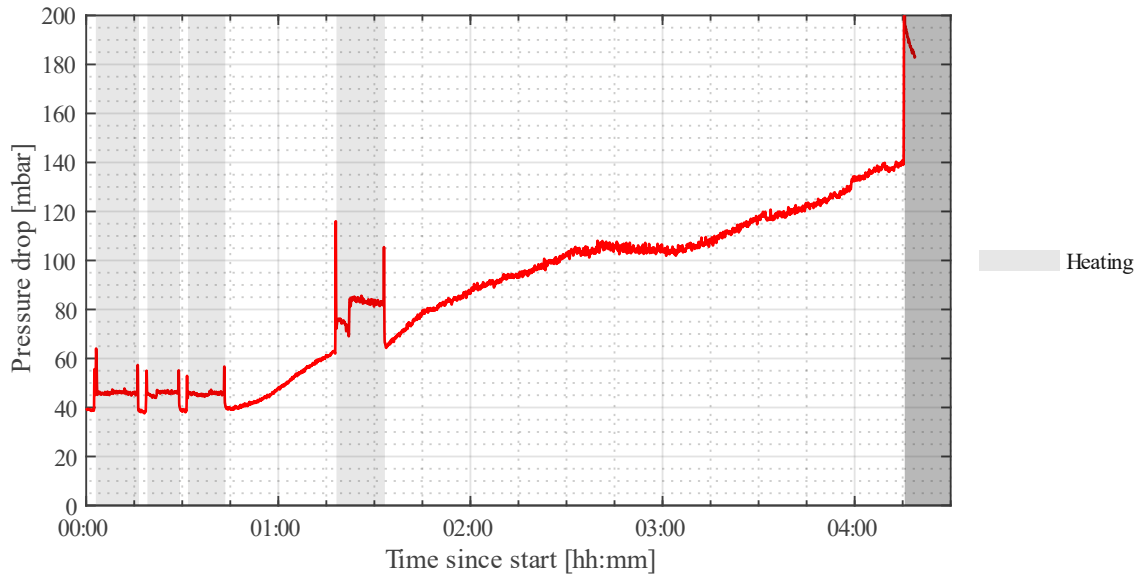

Figure 58: Pressure drop, Iron-Olivine 1

Analysation of material collected in the trial Iron-Olivine 2 showed varying carbon contents in samples taken from different parts of the reactor. The bed material after the trial, material collected in the gravity separator during pyrolysis and during cooling, and material collected in the filter was analysed. The results are given in Table 15 in 5.4.2 and are approx. valid for the experiment discussed here.

The carbon balance presented in Table 12 accounts for these results by multiplying the respective percentages with the mass of the material from the gravity separator and filters and adding the difference to the mass gain of the bed material. While a major 73,04% of the carbon could still be found precipitated on the bed material, a substantial amount of 16,73% had been collected via the gravity separator. Deposits on the reactor surfaces accounted for 4,63% of the formed carbon. More material than usual was collected in the filters as depicted in Figure 59. The discrepancy is within the acceptable range.

Table 12: Carbon balance Iron-Olivine 1

	[g]	[%]
Total amount of carbon collected	**331,59**	**100**
Bed material	242,21	73,04
Filter pyrolysis	9,28	2,80
Filter heating/cooling	9,28	2,80
Gravity separator	55,48	16,73
Reactor walls	15,34	4,63
Carbon produced according to flue gas measurement	**377,38**	
Discrepancy	*45,79*	

Figure 59: Fine powder of carbon and bed material on the filter

5.4.2 Iron-Olivine 2

Bed material	(a) 574 g Fe-powder, 225,6 g Olivine (b) 648,2 g Fe-powder, 254,8 g Olivine (c–j) 796,6 g Fe-powder, 254,8 g Olivine
Bed temperature	(A) 650–920 °C (B) 920–930 °C (C) 930 °C, 940 °C (D) 940 °C
Fluidisation during pyrolysis	various

Table 13: Parameters Iron-Olivine 3

The parameters of the second trial with iron and olivine as bed material are given in Table 13. Various fluidisation options and varying bed heights and compositions were used. NG with a purity of 70–98% (according to the producer) was employed as the primary fluidising agent, simulating more realistic conditions.

The test run was divided into several sections. In (A), the pyrolysis process was started from a low temperature with subsequent heating to the desired conditions. Doing so mitigates the risk of coagulation, as it allows the iron particles to form a protective carbon layer before reaching critical temperatures. This was followed by an analysis of the influence of the bed height and increasing the share of iron in the bed material in (B). Part (C) was designed to study multi-stage operation at two different temperatures, resulting in a correlation between bed height and methane conversion. In the last part (D), the pyrolysis behaviour of natural gas was compared with pure methane.

The pyrolysis process was started after the bed material – with composition (a) from Table 13 – reached a temperature of 650 °C at a NG velocity of 71 mm/s. Figure 60 and 61 show no hydrogen production at this point. With subsequent heating, hydrogen production was initiated at a temperature of approx. 690 °C. This was significantly higher than in the test run Iron-Olivine 1, where significant amounts of hydrogen were measurable at a temperature of 660 °C. The bed material was further heated, and the velocity of NG was raised to 89 mm/s after 17 minutes.

A declining methane yield is visible at minute 57 after a steep increase of the bed temperature. This could be the result of a coagulating effect in the bed material. However, the curve of the pressure drop at that time and the lack of an exponential growth in the later stages of the experiment do not corroborate this train of thought. Another possibility is the deactivation mechanism – which was distinct in the previous tests with this bed material – becoming predominant at this point, i.e. albeit an increasing temperature is beneficial for the pyrolysis reaction, catalyst deactivation exceeds this effect.

Nitrogen was added to the fluidisation after this occurrence (giving a fluidisation velocity of 111 mm/s with 19% N_2 and 81% CH_4) to delay further pyrolysis to verify that no coagulation had occurred. The hydrogen yield resumed to increase thereafter, indicating that catalyst deactivation had subsided, and self-catalysis of the carbon deposits had remained to increase. This behaviour allowed to reset the fluidisation velocity of NG to 71 mm/s. At a temperature of approx. 920 °C and at the time of maximum self-catalysis, hydrogen output reached a maximum of 19 g/h.

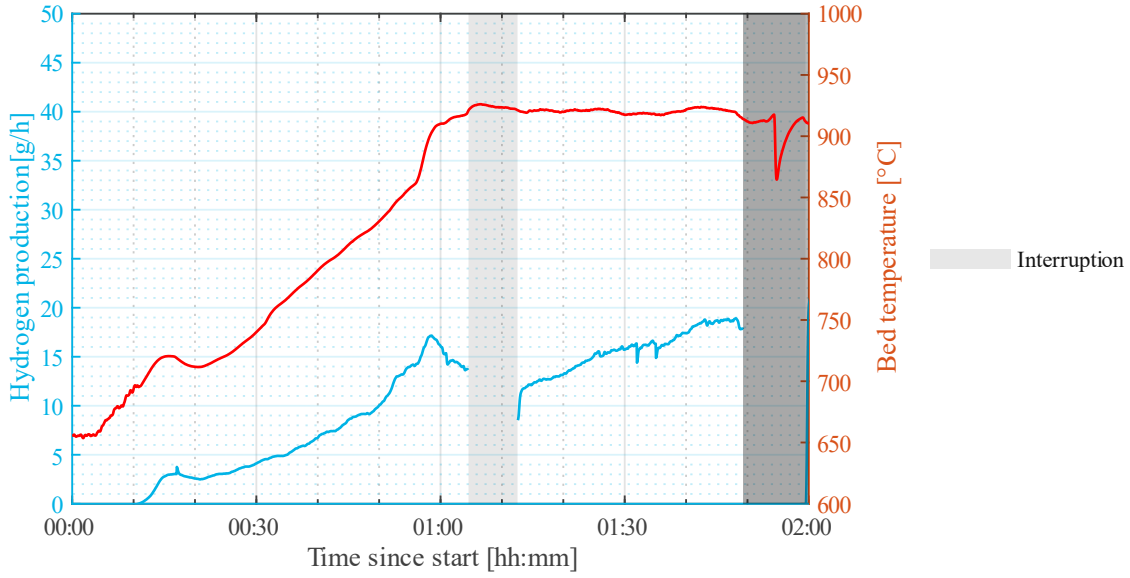

Figure 60: Hydrogen production Iron-Olivine 3, part A

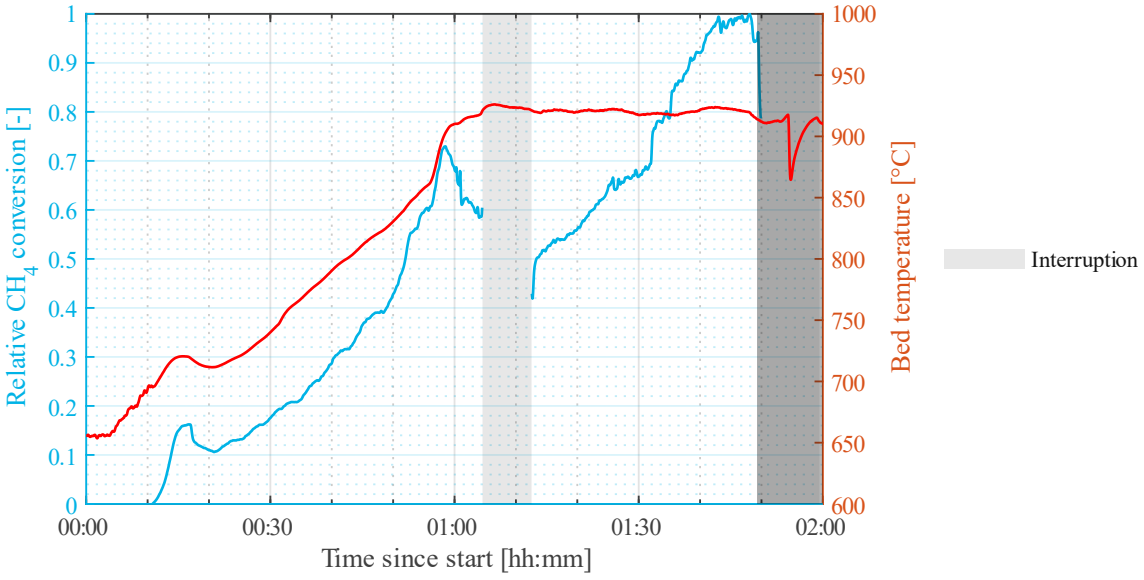

Figure 61: Relative CH_4 conversion Iron-Olivine 3, part A

In part (B), the bed height and the iron content were increased in two steps. Figure 62 and 63 depict hydrogen production and relative methane conversion of this part of the trial.

First, fresh bed material was added to obtain the parameters indicated by (b) in Table 13. Pyrolysis was resumed at a NG velocity of 71 mm/s. The deactivation mechanism on the fresh catalyst did not have a measurable effect and methane conversion climbed partly due to the self-catalytic effect, partly due to a rise in temperature. The maximum hydrogen yield was 27 g/h at a temperature of 925 °C.

Further iron powder was added at 2:40 h after start, giving composition (c) from Table 13. The behaviour was similar to before. At a temperature of 930 °C, a maximum hydrogen production of 35 g/h was obtained.

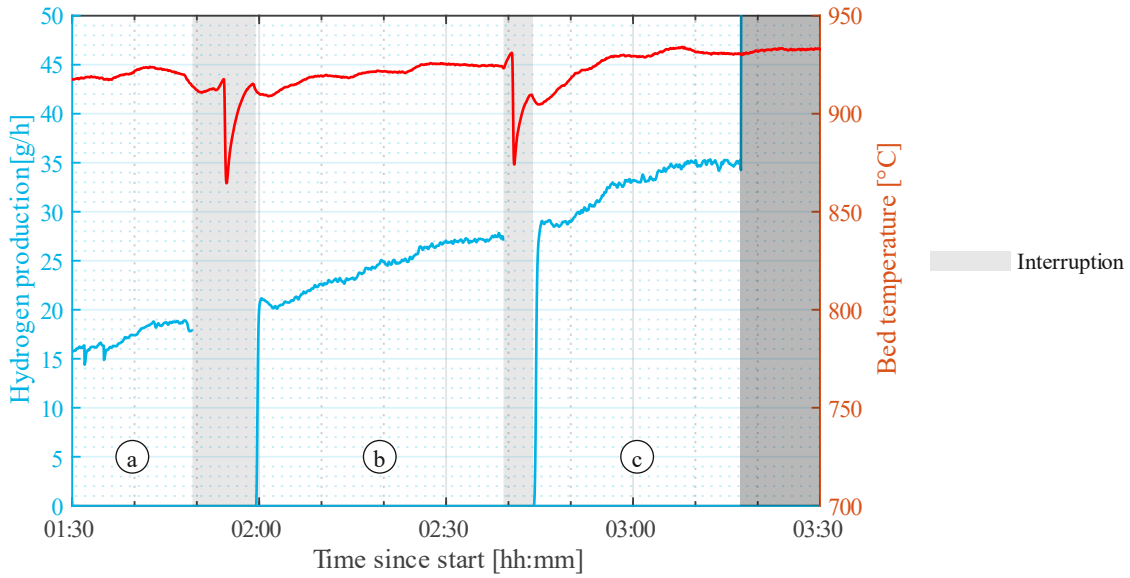

Figure 62: Hydrogen production Iron-Olivine 3, part B

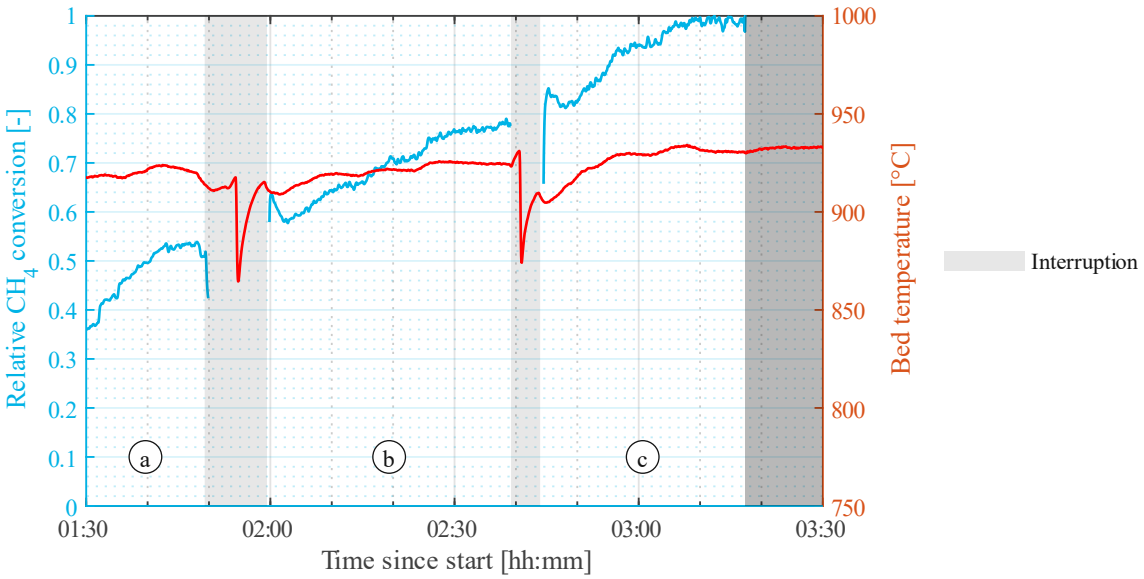

Figure 63: Relative CH_4 conversion Iron-Olivine 3, part B

Part (C) of the test was designed to acquire data on the impact of different bed heights at two different temperatures – 930 °C and 940 °C. Double and triple the bed height was simulated by fluidising with the gas composition approx. equivalent to the off-gas composition from the previous step. The precision of this equivalence was limited by the accuracy and the minimum adjustable flow rate of the rotameters. The experimental setup and results are presented in Table 14. Figure 64 and 65 depict the corresponding data from the off-gas analyser and the methane conversion.

Table 14: Experimental data studying the impact of bed height at a temperature of 930 °C and 940 °C

		d	e	f	g	h
Bed temperature [°C]		930	930	930	940	940
Relative, simulated bed height [-]		1	2	3	1	2
Fluidisation	[mm/s]	71	114	107	71	107
	NG [%]	100	50	33	100	33
	H_2 [%]	0	50	67	0	66
Hydrogen production rate [g/h]		35	89	105	48	110
Relative CH_4 conversion [-]		0,73	1,15	1,44	1,00	1,51

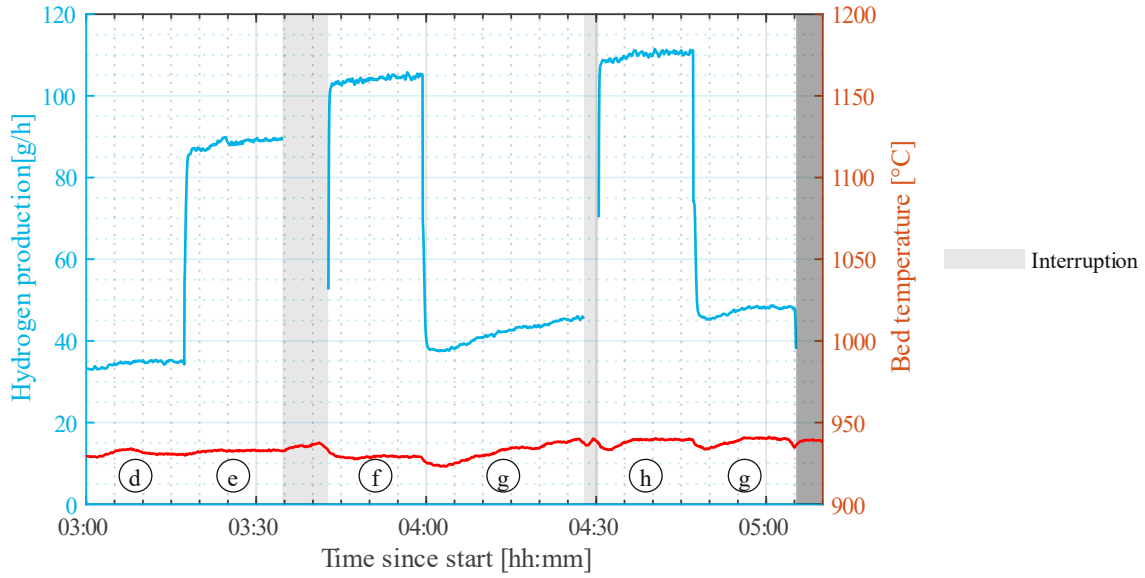

Figure 64: Hydrogen production Iron-Olivine 3, part C

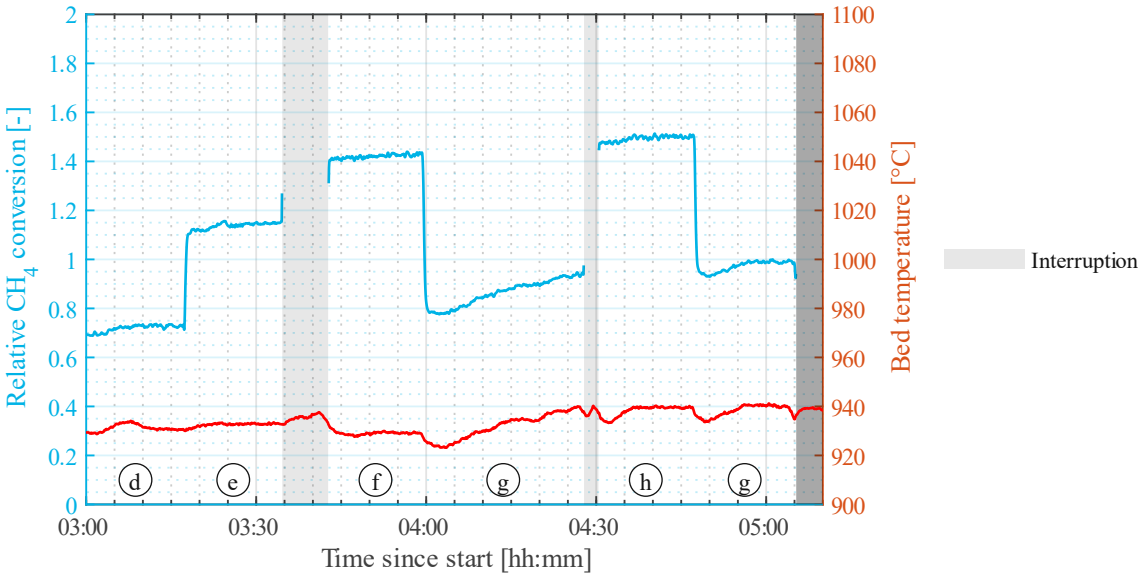

Figure 65: Relative CH_4 conversion Iron-Olivine 3, part C

This data was collected to approximate methane conversion for any bed height as depicted in Figure 66. It becomes apparent that increasing the temperature from 930 °C to 940 °C allows for a significant reduction of the bed height.

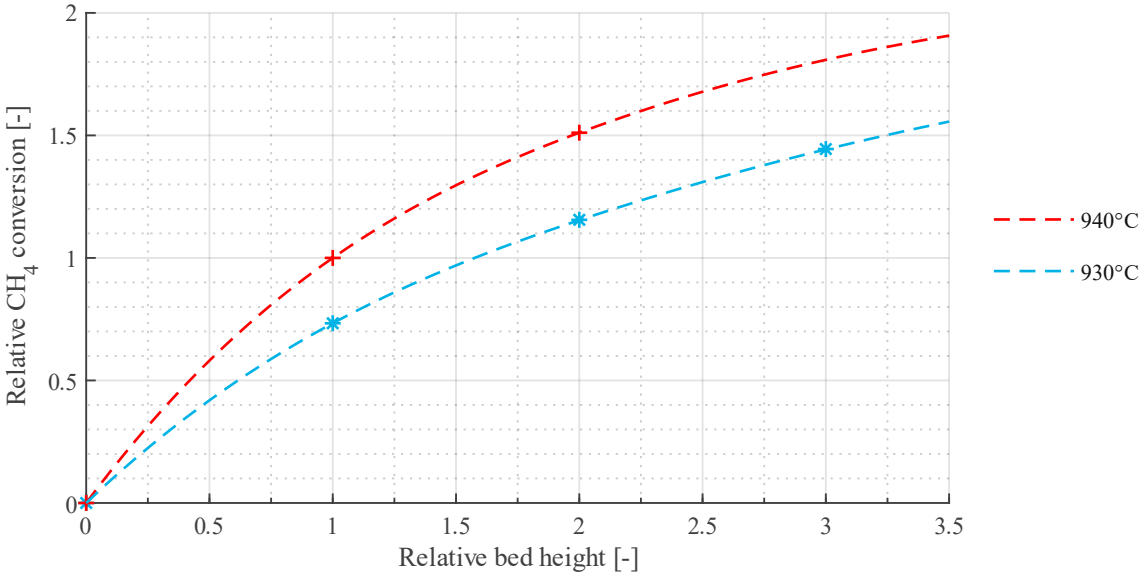

Figure 66: Relative CH_4 conversion vs relative bed height

In part (D) of the experiment, pyrolysis of NG was compared with pyrolysis of pure CH_4 at a temperature of 940 °C and a velocity of 71 mm/s. According to Figure 67 and 68, the impact on the composition of the off-gas and on methane conversion is minimal. The hydrogen output is approx. 2 g/h higher when applying pure methane as compared to NG. However, the NG tested here proved to have few impurities with a methane content of approx. 98% (the upper end of the manufacturers estimate). Thus, the behaviour might differ using NG with a higher content of contaminants.

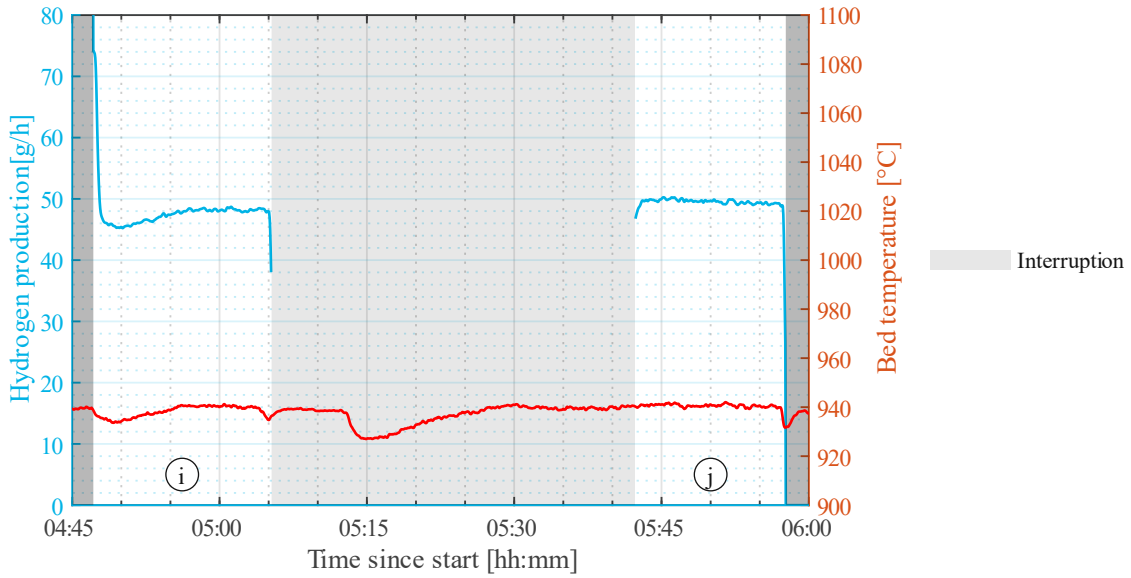

Figure 67: Hydrogen production Iron-Olivine 3, part D

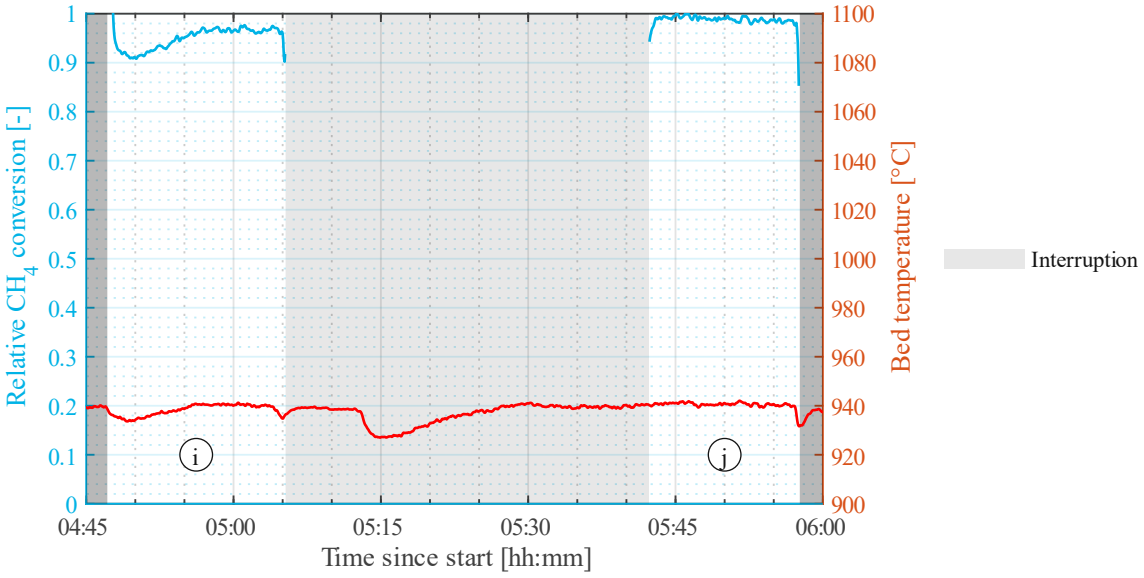

Figure 68: Relative CH_4 conversion Iron-Olivine 3, part D

Contrary to previous experiments with the same bed material, significant amounts of higher hydrocarbons could be measured. In Figure 69, an inverse correlation between methane conversion and share of higher hydrocarbons seems apparent. Ethylene and Ethane are more abundant at times of low hydrogen yield. This leads to the assumption that these compounds are present in NG and crack at higher temperatures.

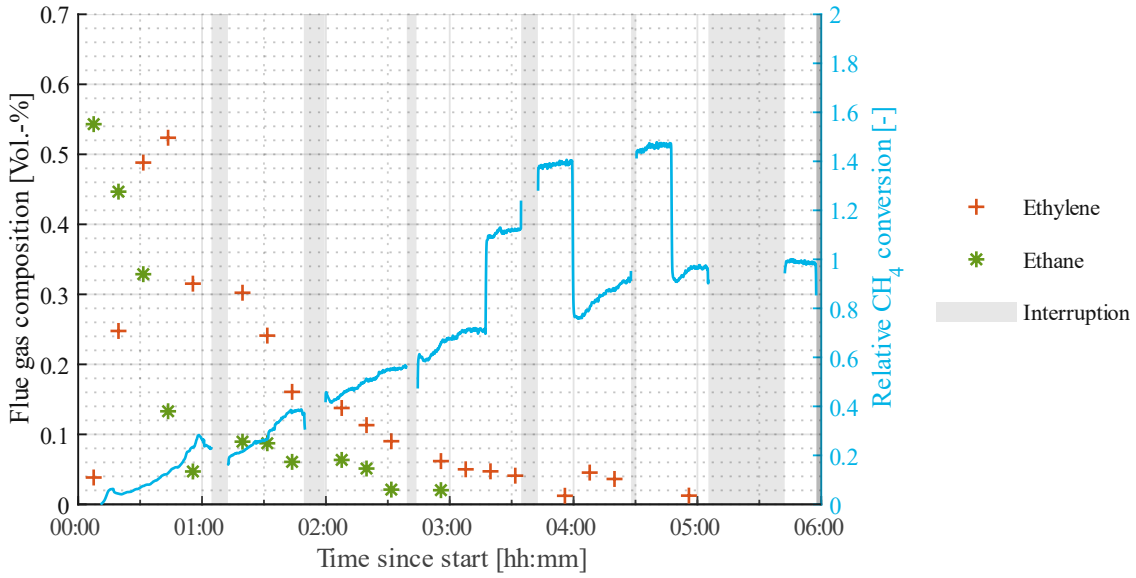

Figure 69: Higher hydrocarbons Iron-Olivine 3

The temperature profile throughout the whole test run is depicted in Figure 70 and does not show any anomalies.

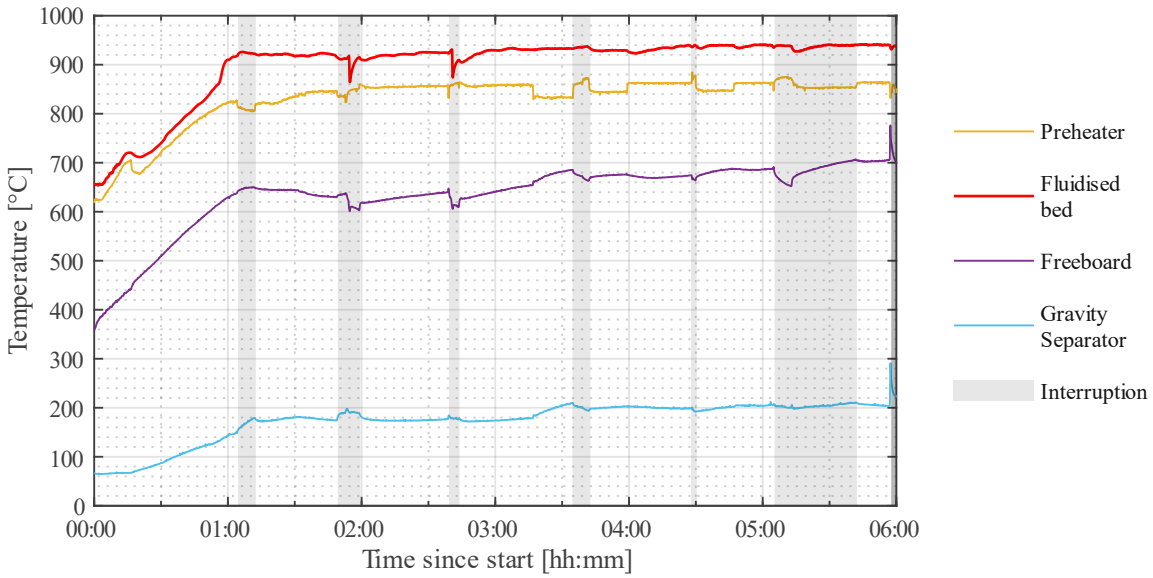

Figure 70: Temperature profile, Iron-Olivine 3

The pressure loss in Figure 71 never increases parabolically and stays rather constant throughout the experiment. This indicates an equilibrium between abrasion and deposition of carbon in the holes of the perforated plate.

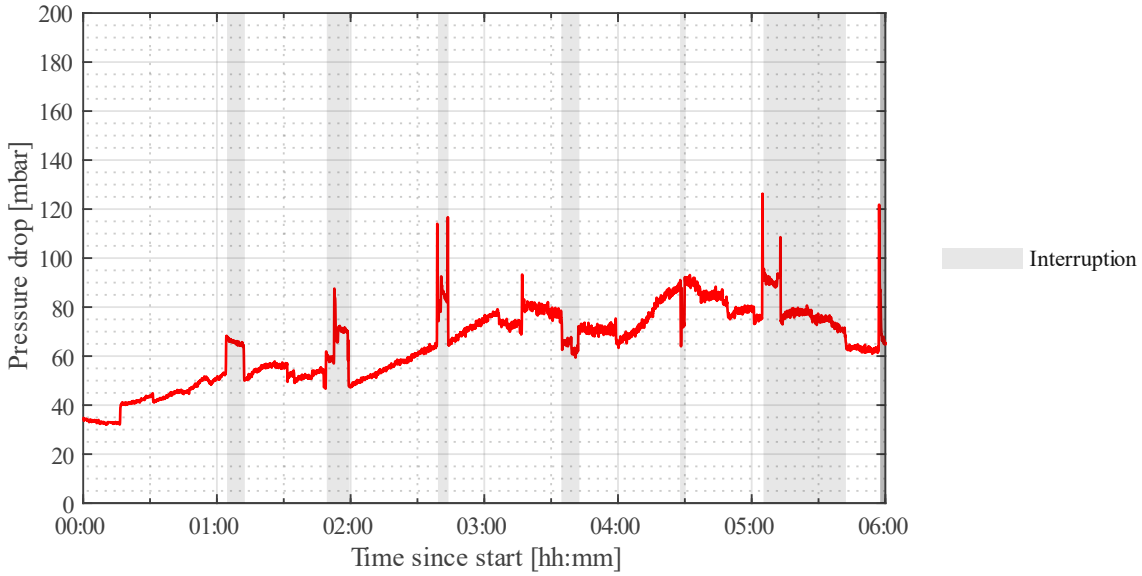

Figure 71: Pressure drop Iron-Olivine 3

An analysis of the material collected here was performed by the Test Laboratory for Combustion Systems at Technical University of Vienna. Specifically, the bed material after trial, the material collected in the gravity separator during pyrolysis and during the cooling phase, and the material collected in the filter was analysed. The relevant results of this analysis are given in Table 15.

Table 15: Carbon content of samples collected in Iron-Olivine 3

	[wt-%]	homogenised [wt-%]
Bed material	25,86	19,71
Gravity separator (collected during pyrolysis)	44,37	43,04
Gravity separator (collected during cooling phase)	62,19	56,29
Filter	71,94	78,84

The carbon balance presented in Table 16 accounts for these results. A total mass of 392,37 g of carbon were produced according to the flue gas measurement. Weighing the bed material, filter and material in the gravity separator revealed that this is an underestimation by at least 31,08 g. A considerable amount of 29,6% of carbon was found in the gravity separator.

Table 16: Carbon balance Iron-Olivine 3

	[g]	[%]
Total amount of carbon collected	**423,45**	**100,00**
Bed material	269,25	63,58
Filter	17,09	4,04
Gravity separator (pyrolysis)	11,75	2,78
Gravity separator (cooling)	125,35	29,60
Carbon produced according to flue gas measurement	**431,13**	
Discrepancy	*7,68*	

6 Discussion of Results and Summary

6.1 Common Characteristics

Comparing the flue gas composition, temperature, pressure and methane-conversion graphs, some recurring behaviours can be observed. In this subchapter, some of these characteristics are discussed exemplarily using specific experiments.

6.1.1 Temperature Dependency

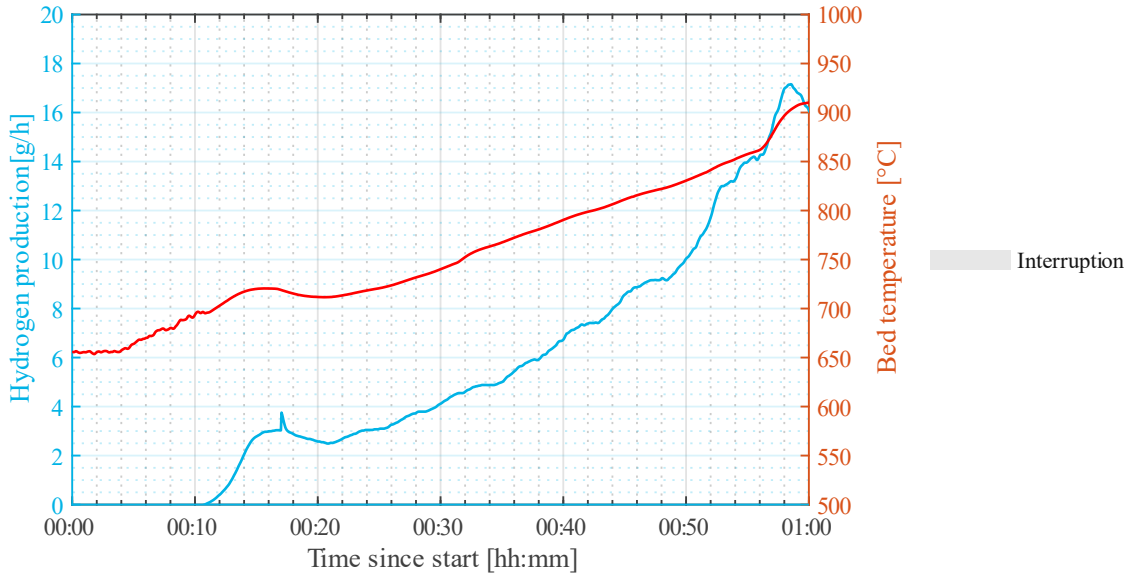

Figure 72: Temperature dependence with Fe–Olivine as bed material

The pyrolysis reaction is an endothermic reaction and is highly temperature dependent in both a catalytic and non-catalytic reaction. A high temperature fosters methane decomposition. At low temperatures, the equilibrium is on the educt side of the equation. This high dependency on temperature can be seen throughout all experiments, where a slightly decreasing bed temperature promptly causes a drop of conversion rate. Figure 72 illustrates this characteristic exemplarily for the first test run with iron powder and olivine as bed material, where methane conversion quadruples from 4% at a temperature of 700 °C to 13% at a temperature of 900 °C.

6.1.2 Pressure Drop

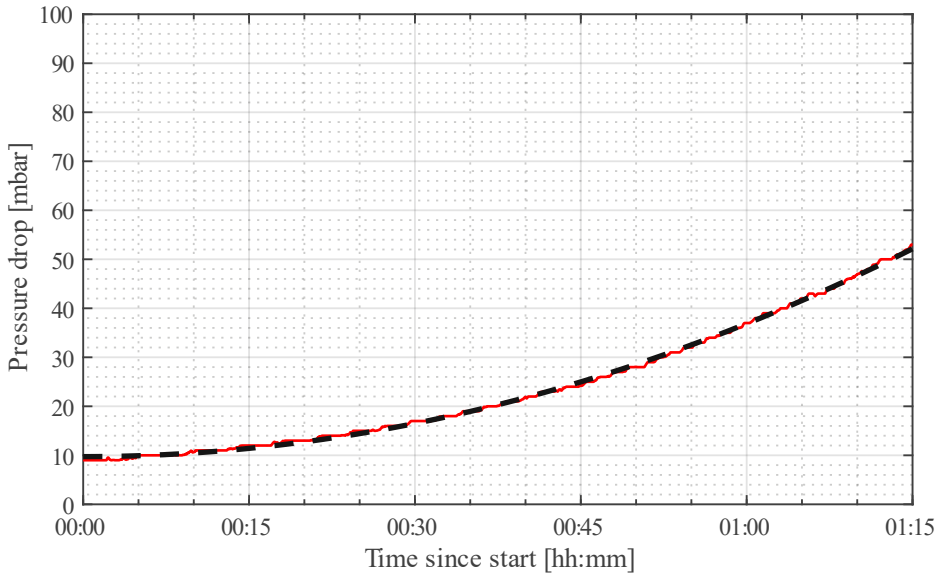

Figure 73: Pressure loss with AC as bed material, trial AC1

Fluidised bed systems – per default – exhibit a loss in pressure. It consists of two components, one exerted by the gas distributor (a plate in our case), the other by the weight of the bed material. Over the course of the experiments, the pressure drop increases in all tests runs in the extent of tens to hundreds of mbar. In many cases, the increase can be described with a quadratic function as seen in Figure 73. The growth must be ascribed to either the bed material or the distributor plate. Specifically, there are two phenomena that can be responsible for this behaviour. Firstly, the increase in mass of the bed material due to the carbon deposition on the catalyst surface. Secondly, the continuous plugging of the holes in the perforated plate.

The mass gain of the bed material occurs simultaneously with the hydrogen production through carbon deposition on the catalyst surface. Equation (43) is Pascal's law calculating the hydrostatic pressure difference and is applicable in bubbling fluidised bed systems (Hofbauer, 1995):

$$\Delta p = p - p_0 = \frac{M \cdot g}{A}. \tag{43}$$

Deriving (43) according to time gives equation (44), where it becomes obvious that the pressure drop should change concurrently with mass:

$$\frac{\partial p}{\partial t} - p_0 = \frac{\partial M}{\partial t} \cdot \frac{g}{A}. \tag{44}$$

In most trials presented here, the change in mass is limited to a few tens to hundreds of grams. In the reactor used, 100 g additional mass of the bed material correspond to an additional pressure loss of 4,2 mbar according to (43). Consequently, this factor does play a role, but affects little when compared to the total additional pressure differences measured in the test runs. Moreover, it fails to explain the

quadratic shape of the curve: Assuming a constant hydrogen yield and neglecting abrasion and other effects, a constant carbon deposition is exerted. This causes the mass of the bed material to increase linearly, directly leading to a linear growth of the pressure difference. For it to be quadratic, the carbon deposition and therefore the CH_4 conversion would need to present a quadratic behaviour as well. That is not the case in any of the conducted trials. This further corroborates the hypothesis that an increase in mass of the bed material is not the main driver for an increase in pressure loss.

Therefore, it can be theorised that mechanisms related to the distributor plate must be the major contributor to this occurrence. In the experimental setup, the distributor plate is a perforated plate made from iron. Investigation of the plate after each test run reveals that a significant number of holes are either completely plugged or significantly reduced in diameter through carbon deposits.

The pressure loss in a perforated plate Δp_D is a function of the gas velocity in the holes U_0, the gas density ρ_g and a resistance coefficient ξ:

$$\Delta p_D = p_D - p_0 = \xi \cdot \frac{\rho_g}{2} \cdot U_0^2 \,. \tag{45}$$

There exist various correlations for the resistance coefficient depending on the characteristics of the distributor plate. The present experimental setup allows to use the following:

$$\xi_0 = 1{,}5 \cdot \left(\frac{d_0}{s}\right)^{0{,}26} \qquad valid\ for\ 1 < \frac{d_0}{s} < 10 \,. \tag{46}$$

The velocity in the holes is a function of the superficial velocity and the number and diameter of the holes:

$$U_0 = \frac{A}{A_0} \cdot U_s \,, \tag{47}$$

with:

$$A_0 = N \cdot a_0 = N \cdot \frac{d_0^2 \cdot \pi}{4} \,. \tag{48}$$

Neglecting the diameter dependence of ξ, it is apparent that Δp_D is approximately inversely proportional to a_0 squared and d_0 to the power of four:

$$\Delta p_D \propto a_0^{-2} \quad and \quad \Delta p_D \propto d_0^{-4} \,. \tag{49}$$

Equation (49) can be derived with respect to time to obtain rates at which the respective parameters change:

$$\frac{\partial p_D}{\partial t} \propto \frac{\partial a_0^{-2}}{\partial t} \quad and \quad \frac{\partial p_D}{\partial t} \propto \frac{\partial d_0^{-4}}{\partial t} \,. \tag{50}$$

Assuming a constant rate of carbon deposition inside the holes, a_0 decreases linearly. According to (50), this leads to a quadratic shape of the rate at which the pressure drop of the perforated plate changes.

Figure 74–76 highlight completely plugged (dark orange), partially plugged (bright orange), and predominantly unplugged (green) holes in the perforated plates of selected trials. All these trials experienced a significant growth of the pressure drop throughout the course of the experiments. Table 17 does, however, indicate that the change of pressure was greater in AC1 and Iron-Olivine 1 than in the trial with limestone. This might indicate that visual examination of the perforated plates is an insufficient indicator to determine the extent of blockage and carbon deposition inside the holes.

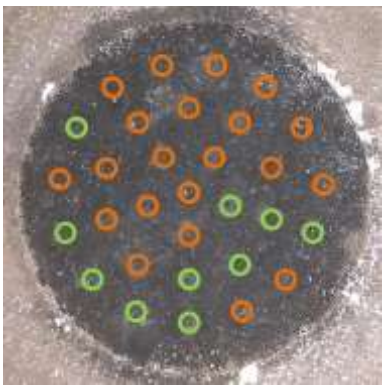

Figure 74: Perforated plate Limestone

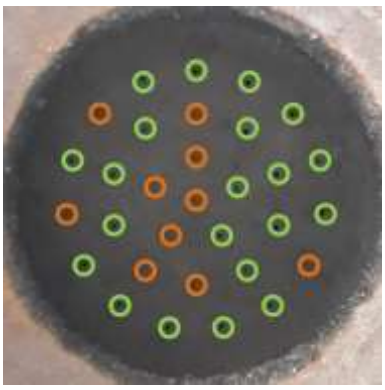

Figure 75: Perforated Plate AC1

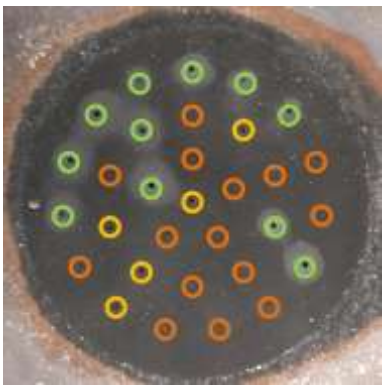

Figure 76: Perforated plate Iron-Olivine 1

Table 17: Pressure loss in selected trials

	Limestone	AC1	Iron-Olivine 1
Δp at beginning [mbar]	12	10	40
Δp at end [mbar]	22	150	140

6.2 Comparative Analysis

Our trials have shown that Limestone hardly has the potential to significantly catalyse methane decomposition. Typical for limestone is the decomposition to calcium oxide and carbon dioxide at elevated temperatures. The calcium oxide further acts as the catalyst. Albeit a maximum hydrogen production rate of 13 g/h was achieved, and a higher output is potentially possible if a higher bed temperature or a lower methane flow rate is employed, the bed material quickly deactivates. After dropping to a minimum of 1,3 g/h, the conversion rate kept increasing, indicating a minor self-catalytic effect of the carbon deposits on the bed particles. The impact of this effect was, however, insignificant in the test run. For two hours, the hydrogen yield grew at a rate of 0,24 g/h per hour. Long term studies are needed to ascertain how long this growth is present. Considering the ineffectiveness of this catalyst compared to others, further studies regarding limestone can be regarded to as not expedient.

Experiments utilising activated carbon resulted in high yields of hydrogen but also in rapid deactivation of the catalyst. One tests run was performed at 910 °C and two at 950 °C. At 910 °C and a methane

velocity of 89 mm/s, a maximum hydrogen output of 30 g/h could be achieved. At 950 °C the maximum hydrogen production rate was 40 g/h at a methane velocity of 71 mm/s and 36 g/h at 89 mm/s. In one case, exceeding the temperature of 950 °C resulted in the coagulation of carbon particles and the formation of a cake with channels. In all trials, the catalyst deactivated rapidly within 30 minutes of use until hydrogen yield remained approximately constant at 2,2 g/h at 910 °C or 6 g/h at 950 °C, respectively. Regeneration is possible, albeit the catalytic activity was not fully restored. Reactivation with CO_2 increased the hydrogen output from 2,3 g/h to 5,1 g/h through gasification of 15% of the carbon deposits. The catalyst subsequently deactivated in the same manner as before until a near constant hydrogen yield of 2,2 g/h was obtained. Regeneration with H_2O returned more promising results and led to the emission of a gas containing hydrogen, CO and CO_2, which is partially usable as syngas. Our test run alternated between pyrolysis and regeneration in 7-minute cycles. The initial pace of deactivation was nearly identical to trials without reactivation. Reactivation and deactivation were in balance in later parts of the reaction, in which the hydrogen production rate ranged from 11 to 27 g/h. However, this mode of operation led to the emission of substantial amounts of carbon dioxide. Additionally, the endothermic process of steam gasification requires additional energy. In both regeneration scenarios, substantial amounts of carbon will be lost, inhibiting its marketing, and reducing the economic profitability. In the case of reactivation with steam, the lost profits from a loss of carbon and the additional revenues from use and utilisation of syngas must be offset. Both scenarios would best be implemented in a circulating fluidised bed system, with carbon-encapsulated AC particles moving from the pyrolysis reactor to the combustion or gasification reactor, where some of the carbon is burned off or gasified. The catalyst is entrained in the gas flow and reintroduced into the pyrolysis chamber from the top.

Ilmenite as a catalyst requires an activation step with hydrogen to reduce the outer surface of the particles to iron. As a metal, it is prone to coagulation at elevated temperatures, resulting from phase changes or softening of the material. This problem was prominent throughout our trial. Agglomeration of the bed material led to defluidisation at temperatures even below 850 °C. The maximum hydrogen production rate that could be achieved was 7,5 g/h at a methane velocity of 114 mm/s and 6,5 g/h at a velocity of 89 mm/s. Operation at a lower temperature of 800 °C and a velocity of 114 mm/s to prevent defluidisation resulted in low hydrogen yield of 3 g/h. Albeit being low, the conversation rate has an increasing tendency throughout the trial. This could potentially be ascribed to a self-catalytic effect of carbon deposits. Ilmenite requires further investigation. Diluting the material with an inert substance such as olivine could possibly prevent agglomeration of the metallic particles and allow for higher temperatures, bringing the hydrogen yield to acceptable levels. Starting the pyrolysis reaction at low temperatures with subsequent heating, as has been done in trials with iron and olivine, could also hamper aggregation tendencies by forming a protective carbon layer on the outer particle interface.

In the two test runs with iron powder, the catalyst was diluted with olivine to obviate the fluidisation problems observed with ilmenite. The operation was initialised at low temperatures with subsequent heating. It is thought that doing so created a carbon layer on the outermost interface of the metal particles that exacerbated their coagulation. Proceeding this way enabled successful operation at temperatures of 950 °C. The catalytic activity of the bed material first quickly decreased due to expected deactivation effects, but soon approached a minimum after which the activity constantly increased. This effect can be ascribed to an auto-catalytic effect of the formed carbon deposits and to breaking up of particles to grains of smaller sizes, enlarging the exposed surface area. In our mode of operation, a maximum hydrogen production rate of 55 g/h was achieved at a temperature of 950°C. Simulating a bed with double the height at a temperature of 940 °C, methane conversation increased by 50%. It was also shown that increasing the temperature by 10 °C from 930 °C to 940 °C could reduce the necessary bed height to achieve the same methane conversation by approximately 33%. Part of the test was dedicated to compare the hydrogen yields between commercial grade natural gas and pure methane. No significant difference between the two input-gases was found. However, the natural gas that was employed here proved to have little contaminants, with a methane concentration of approx. 98%. In all cases, the conversation rate approached a maximum. Further long-term experiments are necessary to verify the longevity of the bed material. The carbon collected in the gravity separator and filters was contaminated with significant amounts of iron. It is therefore necessary to find an efficient separation process. This is imperative if marketing of the carbon by-product is desired.

Neither bed material caused significant emissions of ethane or ethylene. Using natural gas for fluidisation caused emissions of these substances at low temperatures and when catalytic activity was low. High temperatures of 900 °C and good catalytic properties led to efficient cracking of these components.

7 Conclusion and Outlook

Current state of the art hydrogen production through steam methane reforming emits vast amounts of carbon dioxide. A shift towards a greener technology is inevitable to combat climate change. Implementing carbon capture and storage in current processes is controversial. The alternative route of water electrolysis requires massive amounts of energy that can currently not be produced in a carbon-neutral manner. Methane pyrolysis uses a readily available feedstock without direct carbon emissions and energy requirements that are comparable to steam methane reforming.

Methane pyrolysis can be performed as a thermo-catalytic process with solid catalysts, in molten media, or in plasma. All of those were discussed herein, with a special focus on solid catalysts. Various materials were employed in past research. Metallic catalysts were utilised as pure metal and in supported and promoted states. Carbonaceous catalysts were proposed to omit carbon separation. Most authors mention the problematic of rapid deactivation of catalysts. Self-catalytic effects of materials were reported in some studies.

Solid catalysts can be employed in various types of reactors. Large-scale embodiments used for methane decomposition both currently and in the past were presented. This includes promising concepts for future industrial applications. Fluidised bed reactors are among the most promising options. Major advantages of fluidised bed systems are excellent heat and mass transfer and avoidance of reactor blockage, among others. Drawbacks of fluidised beds include mechanical degradation.

The experimental setup of the practical part of this thesis was described in detail. As were the mathematical relations that were employed in the calculations throughout the practical work. Different catalysts were employed to study their activity and potential future use in the decomposition of methane.

Overall, Limestone resulted in poor methane conversion. The initial hydrogen production rate was insufficient, and deactivation of the material reduced it further. Albeit a self-catalytic effect could be observed, the extent is too meagre to bear a significant positive influence. Further research regarding this bed material is therefore likely inexpedient.

Activated carbon faced similar challenges regarding the rapid deactivation and the subsequent inadequate hydrogen yield. Regeneration of the bed material is possible, depending on the reactivating agent it does, however, results in the emission of carbon dioxide and the gasification of significant amounts of carbon. With regard to a carbon emission free future, this is not desirable. At very high temperatures, coagulation of AC particles could be problematic.

Methane pyrolysis with ilmenite as a catalyst did not eventuate in expressive results. The material coagulated at low temperatures and defluidisation was a major issue throughout the trials. Disregarding ilmenite as a whole is – at this point – inappropriate. Dilution of the catalyst with an inert material could

potentially prevent aggregation of the material and stabilise the fluidisation. Future research could employ a more cautious approach with a slowly increasing bed temperature, early treatment with methane, dilution of the catalyst, and adequate fluidisation velocity to obviate the problems that were encountered in this practical work.

Out of all studied catalysts, iron gave the most promising results. The powder was diluted with olivine and a careful approach with low temperatures at the beginning of the pyrolysis process was chosen. Coagulation has been avoided through deposition of carbon on the particle interface. The bed material showed significant signs of autocatalysis. Break-up of iron particulates and the creation of a larger interface does likely boost the reaction as well. Long-term studies of this bed material are needed to examine the longevity of the catalyst. A significant quantity of small grains of carbon and bed material is entrained in the gas flow and discharged. An efficient process to separate the carbon from the bed material must be found.

References

Abánades, A., Rubbia, C., & Salmieri, D. (2013). Thermal cracking of methane into hydrogen for a CO_2-free utilization of natural gas. *International Journal of Hydrogen Energy*, *38*, 8491–8496.

Abánades, A., Ruiz, E., Ferruelo, E. M., Hernández, F., Cabanillas, A., Martínez-Val, J. M., Rubio, J. A., López, C., Gavela, R., Barrera, G., Rubbia, C., Salmieri, D., Rodilla, E., & Gutiérrez, D. (2011). Experimental analysis of direct thermal methane cracking. *International Journal of Hydrogen Energy*, *36*, 12877–12886.

Abánades, V. A., Muñoz, A. J., Martinez, V. P. J. M., Geissler, T., Stoppel, L., & Dietrich, B., et al. (2018): *Patent EP3521241 (A1)*.

Abánades, V. A., Muñoz, A. J., Martínez, V. P. J. M., Geissler, T., Stoppel, L., & Dietrich, B., et al. (2019): *Patent WO2019154732 (A1)*.

Abbas, H. F., & Daud, W. W. (2009). Thermocatalytic decomposition of methane for hydrogen production using activated carbon catalyst: Regeneration and characterization studies. *International Journal of Hydrogen Energy*, *34*, 8034–8045.

Abbas, H. F., & Daud, W. W. (2010). Hydrogen production by methane decomposition: A review. *International Journal of Hydrogen Energy*, *35*, 1160–1190.

Ahmed, S., Aitani, A., Rahman, F., Al-Dawood, A., & Al-Muhaish, F. (2009). Decomposition of hydrocarbons to hydrogen and carbon. *Applied Catalysis A: General*, *359*, 1–24.

Allison, T. (1996). *JANAF Thermochemical Tables, NIST Standard Reference Database 13*: National Institute of Standards and Technology.

Amin, A. M., Croiset, E., & Epling, W. (2011). Review of methane catalytic cracking for hydrogen production. *International Journal of Hydrogen Energy*, *36*, 2904–2935.

Ammendola, P., Chirone, R., Ruoppolo, G., Russo, G., & Solimene, R. (2008). Some issues in modelling methane catalytic decomposition in fluidized bed reactors. *International Journal of Hydrogen Energy*, *33*, 2679–2694.

Ammendola, P., Ruoppolo, G., Chirone, R., & Russo, G. (2006). H_2 production by catalytic methane decomposition in fixed and fluidized bed reactors. In F. Winter (Ed.), *Proceedings of 19th international conference on fluidized bed combustion*.

Anantharaman, A., Cocco, R. A., & Chew, J. W. (2018). Evaluation of correlations for minimum fluidization velocity (U) in gas-solid fluidization. *Powder Technology*, *323*, 454–485.

Ashik, U., Wan Daud, W., & Abbas, H. F. (2015). Production of greenhouse gas free hydrogen by thermocatalytic decomposition of methane – A review. *Renewable and Sustainable Energy Reviews*, *44*, 221–256.

Avdeeva, L. B., Reshetenko, T. V., Ismagilov, Z. R., & Likholobov, V. A. (2002). Iron-containing catalysts of methane decomposition: accumulation of filamentous carbon. *Applied Catalysis A: General*, *228*, 53–63.

Baker, R. (1972). Nucleation and growth of carbon deposits from the nickel catalyzed decomposition of acetylene. *Journal of Catalysis*, *26*, 51–62.

Bartholomew, C. H. (2001). Mechanisms of catalyst deactivation. *Applied Catalysis A: General*, *212*, 17–60.

BASF SE (2021). *BASF Report 2020: Economic, environmental and social performance*.

Bode, A. (2019). *New process for clean hydrogen.* BASF Research Press Conference. Ludwigshafen.

Bromberg, L., Cohn, D. R., Rabinovich, A., & Alexeev, N. (2001). *Hydrogen manufacturing using low current, non-thermal plasma boosted fuel converters*. Proceedings of the Symposium on Energy for the 21st Century: Hydrogen Energy.

Bromberg, L., Cohn, D. R., Rabinovich, A., O'Brie, C., & Hochgreb, S. (1998). Plasma reforming of methane. *Energy & Fuels*, *12*, 11–18.

Cahn, R. W., Eustathopoulos, N., Nicholas, M. G., & Drevet, B. (1999). *Wettability at high temperatures.* Pergamon materials series, 3. Amsterdam: Pergamon.

Chaubey, R., Sahu, S., James, O. O., & Maity, S. (2013). A review on development of industrial processes and emerging techniques for production of hydrogen from renewable and sustainable sources. *Renewable and Sustainable Energy Reviews*, *23*, 443–462.

Chen, L., Qi, Z., Zhang, S., Su, J., & Somorjai, G. A. (2020). Catalytic hydrogen production from methane: A review on recent progress and prospect. *Catalysts*, *10*, 858.

Chesnokov, V. V., & Chichkan, A. S. (2009). Production of hydrogen by methane catalytic decomposition over Ni–Cu–Fe/Al_2O_3 catalyst. *International Journal of Hydrogen Energy*, *34*, 2979–2985.

Cho, W., Lee, S.-H., Ju, W.-S., Baek, Y., & Lee, J. K. (2004). Conversion of natural gas to hydrogen and carbon black by plasma and application of plasma carbon black. *Catalysis Today*, *98*, 633–638.

Corey, P. (2021). Bill Gates-backed startup to build 'turquoise hydrogen' pilot by end of 2022. *S&P Global,* 07.07.2021. https://www.spglobal.com/marketintelligence/en/news-insights/latest-news-headlines/bill-gates-backed-startup-to-build-turquoise-hydrogen-pilot-by-end-of-2022-65354106.

Cornejo, A. (2016): *Patent EP3341328 (A1)*.

Cornejo, A. (2018): *Patent WO2018170543 (A1)*.

Dagle, R. A., Dagle, V., Bearden, M. D., Holladay, J. D., Krause, T. R., & Ahmed, S. (2017). *An overview of natural gas conversion technologies for co-production of hydrogen and value-added solid carbon products*.

Dunker, A., Kumar, S., & Mulawa, P. (2006). Production of hydrogen by thermal decomposition of methane in a fluidized-bed reactor—Effects of catalyst, temperature, and residence time. *International Journal of Hydrogen Energy*, *31*, 473–484.

Ermakova, M., Ermakov, D., & Kuvshinov, G. (2000). Effective catalysts for direct cracking of methane to produce hydrogen and filamentous carbon. *Applied Catalysis A: General*, *201*, 61–70.

Ermakova, M. A., Ermakov, D. Y., Chuvilin, A. L., & Kuvshinov, G. G. (2001). Decomposition of methane over iron catalysts at the range of moderate remperatures: The influence of structure of the catalytic systems and the reaction conditions on the yield of carbon and morphology of carbon filaments. *Journal of Catalysis*, *201*, 183–197.

European Patent Bulletin (13/2021): 3 796 770 - 3 799 551 (2021).

Fan, Z., Weng, W., Zhou, J., Gu, D., & Xiao, W. (2021). Catalytic decomposition of methane to produce hydrogen: A review. *Journal of Energy Chemistry*, *58*, 415–430.

Fidalgo, B., Muradov, N., & Menéndez, J. A. (2012). Effect of H_2S on carbon-catalyzed methane decomposition and CO_2 reforming reactions. *International Journal of Hydrogen Energy*, *37*, 14187–14194.

Galanov, S. I., Zherlitsyn, A. G., Medvedev, Y. V., Sidorova, O. I., & Shiyan, V. P. (2011). Production of a highly dispersed carbon material and hydrogen from natural gas in a microwave reactor with metallic catalysts. *Russian Journal of Applied Chemistry*, *84*, 997–1002.

Geißler, T., Abánades, A., Heinzel, A., Mehravaran, K., Müller, G., Rathnam, R. K., Rubbia, C., Salmieri, D., Stoppel, L., Stückrad, S., Weisenburger, A., Wenninger, H., & Wetzel, T. (2016). Hydrogen production via methane pyrolysis in a liquid metal bubble column reactor with a packed bed. *Chemical Engineering Journal*, *299*, 192–200.

Geißler, T., Plevan, M., Abánades, A., Heinzel, A., Mehravaran, K., Rathnam, R. K., Rubbia, C., Salmieri, D., Stoppel, L., Stückrad, S., Weisenburger, A., Wenninger, H., & Wetzel, T. (2015). Experimental investigation and thermo-chemical modeling of methane pyrolysis in a liquid metal bubble column reactor with a packed bed. *International Journal of Hydrogen Energy*, *40*, 14134–14146.

Grace, J. R., & Hetsroni, G. (1982). Handbook of multiphase systems. *Hetsroni MG Edition, Hemisphere, New York*.

Haar, L., Gallagher, J. S., & Kell, G. S. (1988). *NBS/NRC Wasserdampftafeln: Thermodynamische und Transportgrößen mit Computerprogrammen für Dampf und Wasser in SI-Einheiten*. Berlin, Heidelberg, s.l.: Springer Berlin Heidelberg.

Hardman, N. J. (2017). The new carbon black and its role in the United States manufacturing renaissance. *Reinforced Plastics*, *61*, 145–148.

Hardman, N. J., Taylor, R. W., Hoermann, A. F., Johnson, P. L., Cardinal, C. J. P., & Hanson, R. J. (2016): *Patent US2017073522 (A1)*.

Harp, G. (2019). Technologien zur Produktion von Wasserstoff für die Herstellung synthetischer Kraftstoffe. In W. Maus (Ed.), *Zukünftige Kraftstoffe* (pp. 305–370). Berlin, Heidelberg: Springer Berlin Heidelberg.

Hazer Group Limited (2021). *Commencement of Site Works and Project Update*. Perth, WA.

Heidelberger, M. (2019). *Wasserstoff aus Erdgas ohne CO_2-Emissionen: KIT und Wintershall Dea starten gemeinsame Arbeiten zur klimafreundlichen Methanpyrolyse im industriellen Maßstab*. Presseinformation 141/2019. Karlsruhe.

Hofbauer, H. (1995). *Wirbelschichttechnik*. Wien: Technische Universität Wien, Institut für Verfahrenstechnik, Brennstofftechnik und Umwelttechnik.

Jakobsen, H. A. (2014). Fluidized Bed Reactors. In H. A. Jakobsen (Ed.), *Chemical reactor modeling* (pp. 1005–1056). Cham: Springer International Publishing.

Jang, H. T., & Cha, W. S. (2007). Hydrogen production by the thermocatalytic decomposition of methane in a fluidized bed reactor. *Korean Journal of Chemical Engineering*, *24*, 374–377.

Kang, D., Rahimi, N., Gordon, M. J., Metiu, H., & McFarland, E. W. (2019). Catalytic methane pyrolysis in molten $MnCl_2$-KCl. *Applied Catalysis B: Environmental*, *254*, 659–666.

Kock, A., De Bokx, P., Boellaard, E., Klop, W., & Geus, J. (1985). The formation of filamentous carbon on iron and nickel catalysts II. Mechanism. *Journal of Catalysis*, *96*, 468–480.

Konieczny, A., Mondal, K., Wiltowski, T., & Dydo, P. (2008). Catalyst development for thermocatalytic decomposition of methane to hydrogen. *International Journal of Hydrogen Energy*, *33*, 264–272.

Konno, K., Onoe, K., Takiguchi, Y., & Yamaguchi, T. (2013). Direct preparation of hydrogen and carbon nanotubes by microwave plasma decomposition of methane over Fe/Si activated by biased hydrogen plasma. *Green and Sustainable Chemistry*, *03*, 19–25.

Korolev, Y. D., Frants, O. B., Landl, N. V., Geyman, V. G., Zerlitsyn, A. G., Shiyan, V. P., & Medvedev, Y. V. (2009). Nonself-sustained microwave discharge in a system for hydrocarbon decomposition and generation of carbon nanotubes. *IEEE Transactions on Plasma Science*, *37*, 2298–2302.

Lázaro, M. J., Pinilla, J. L., Suelves, I., & Moliner, R. (2008). Study of the deactivation mechanism of carbon blacks used in methane decomposition. *International Journal of Hydrogen Energy*, *33*, 4104–4111.

Leal Pérez, B. J., Medrano Jiménez, J. A., Bhardwaj, R., Goetheer, E., van Sint Annaland, M., & Gallucci, F. (2021). Methane pyrolysis in a molten gallium bubble column reactor for sustainable hydrogen production: Proof of concept & techno-economic assessment. *International Journal of Hydrogen Energy*, *46*, 4917–4935.

Lee, D. H. (2015). Hydrogen production via the Kværner process and plasma reforming. In V. Subramani, A. Basile, & T. N. Veziroğlu (Eds.), *Hydrogen production and purification* (pp. 349–391). Amsterdam, Boston, Cambridge: Elsevier/WP Woodhead Publishing.

Linstrom, P. (1997). *NIST Chemistry WebBook, NIST Standard Reference Database 69*: National Institute of Standards and Technology.

Lynum, S., Hox, K., Haugsten, K. E., & Langoey, J. (1993): *Patent WO9320153 (A1)*.

Maaß, H. J., Göke, V., Machhammer, O., Guzmann, M., Schneider, C., & Hormuth, W., et al. (2012a): *Patent EP2729404 (A2)*.

Maaß, H. J., Göke, V., Machhammer, O., Guzmann, M., Schneider, C., & Hormuth, W., et al. (2012b): *Patent WO2013004398 (A2)*.

Maaß, H. J., Göke, V., Machhammer, O., Guzmann, M., Schneider, C., & Hormuth, W., et al. (2012c): *Patent US2014127121 (A1)*.

Matsen, J. M. (1996). Scale-up of fluidized bed processes: Principle and practice. *Powder Technology*, *88*, 237–244.

Mauthner, K. (2010). *Entwicklung einer kontinuierlichen Wasserstoff-Carbon Nanotubes Demo-Produktionsanlage*. Graz.

McFarland, E. (2019). Molten-salt methane pyrolysis optimization through in-situ carbon characterization and reactor design. https://arpa-e.energy.gov/sites/default/files/9%2010%20H2%20Performers%20C-Zero_Comprssed.pdf. Accessed 30.06.2021.

McFarland, E. W., Upham, C., Palmer, C., Su, S., Mannini, D., & Rahimi, N., et al. (2019): *Patent US2021061654 (A1)*.

McFarland, E. W., Upham, C., Zeng, J., Palmer, C., Su, S., & Mannini, D., et al. (2018): *Patent US2020283293 (A1)*.

Medrano, J. A., Palo, E., & Gallucci, F. (2020). Konventionelle Verfahren zur Wasserstoffherstellung. In M. Kircher, & T. Schwarz (Eds.), *CO_2 und CO – Nachhaltige Kohlenstoffquellen für die Kreislaufwirtschaft* (pp. 17–37). Berlin, Heidelberg: Springer Berlin Heidelberg.

Medvedev, Y. V., Zherlitsyn, A. G., Gunther, V. E., Galanov, S. I., Shiyan, V. P., & Ryabchikov, A. I., et al. (2005): *Patent RU2005139640 (A)*.

Moliner, R., Suelves, I., Lazaro, M., & Moreno, O. (2005). Thermocatalytic decomposition of methane over activated carbons: influence of textural properties and surface chemistry. *International Journal of Hydrogen Energy*, *30*, 293–300.

Monolith Materials, Inc. (2021). *Monolith Materials Receives Investments from SK Inc. and NextEra Energy Resources*. Lincoln, Nebraska, USA.

Msheik, M., Rodat, S., & Abanades, S. (2021). Methane cracking for hydrogen production: A review of catalytic and molten media pyrolysis. *Energies*, *14*, 3107.

Muradov, N. (2000a). Hydrogen from fossil fuels without CO_2 emissions. In C. E. Grégoire Padró, & F. Lau (Eds.), *Advances in hydrogen energy: Proceedings of an american chemical society symposium on hydrogen production, storage, and utilization, held august 22 - 26, 1999, in New Orleans, Louisiana* (pp. 1–16). New York, NY: Kluwer Academic/Plenum Publishers.

Muradov, N. (2000b). Thermocatalytic CO_2-free production of hydrogen from hydrocarbon fuels. In *Thermocatalytic CO_2-free production of hydrogen from hydrocarbon fuels*.

Muradov, N. (2001a). Catalysis of methane decomposition over elemental carbon. *Catalysis Communications*, *2*, 89–94.

Muradov, N. (2001b). Hydrogen via methane decomposition: an application for decarbonization of fossil fuels. *International Journal of Hydrogen Energy*, *26*, 1165–1175.

Muradov, N. (2002). Thermocatalytic CO_2-free production of hydrogen from hydrocarbon fuels. In *Proceedings of the 2002 U.S. DOE hydrogen program review NREL/CP-610-32405*.

Muradov, N. (2003): *Patent US 6,670,058*.

Muradov, N. (2017). Low to near-zero CO_2 production of hydrogen from fossil fuels: Status and perspectives. *International Journal of Hydrogen Energy*, *42*, 14058–14088.

Muradov, N., Chen, Z., & Smith, F. (2005a). Fossil hydrogen with reduced emission: Modeling thermocatalytic decomposition of methane in a fluidized bed of carbon particles. *International Journal of Hydrogen Energy*, *30*, 1149–1158.

Muradov, N., Smith, F., & T-Raissi, A. (2005b). Catalytic activity of carbons for methane decomposition reaction. *Catalysis Today*, *102-103*, 225–233.

Muradov, N., & Vezirolu, T. (2005). From hydrocarbon to hydrogen? Carbon to hydrogen economy. *International Journal of Hydrogen Energy*, *30*, 225–237.

Palmer, C., Bunyan, E., Gelinas, J., Gordon, M. J., Metiu, H., & McFarland, E. W. (2020). CO_2-free hydrogen production by catalytic pyrolysis of hydrocarbon feedstocks in molten Ni-Bi. *Energy & Fuels*, *34*, 16073–16080.

Palmer, C., Tarazkar, M., Kristoffersen, H. H., Gelinas, J., Gordon, M. J., McFarland, E. W., & Metiu, H. (2019). Methane pyrolysis with a molten Cu–Bi alloy catalyst. *ACS Catalysis*, *9*, 8337–8345.

Parmar, K. R., Pant, K. K., & Roy, S. (2021). Blue hydrogen and carbon nanotube production via direct catalytic decomposition of methane in fluidized bed reactor: Capture and extraction of carbon in the form of CNTs. *Energy Conversion and Management*, *232*, 113893.

Petters, S. (2020). *Decarbonised hydrogen from natural gas: The case for Pyrolysis.* FSR online workshop series on Hydrogen Technology. Florence School of Regulation.

Petters, S., & Tse, K. C. K. (2011): *Patent WO2012068781 (A1)*.

Pinilla, J., Moliner, R., Suelves, I., Lazaro, M., Echegoyen, Y., & Palacios, J. (2007). Production of hydrogen and carbon nanofibers by thermal decomposition of methane using metal catalysts in a fluidized bed reactor. *International Journal of Hydrogen Energy*, *32*, 4821–4829.

Pinilla, J. L., Suelves, I., Lázaro, M. J., Moliner, R., & Palacios, J. M. (2010). Parametric study of the decomposition of methane using a $NiCu/Al_2O_3$ catalyst in a fluidized bed reactor. *International Journal of Hydrogen Energy*, *35*, 9801–9809.

Pinilla, J. L., Utrilla, R., Lázaro, M. J., Moliner, R., Suelves, I., & García, A. B. (2011). Ni- and Fe-based catalysts for hydrogen and carbon nanofilament production by catalytic decomposition of methane in a rotary bed reactor. *Fuel Processing Technology*, *92*, 1480–1488.

Pocock, G., Cornejo, A., & Chua, H. T. (2016): *Patent EP3277623 (A1)*.

Pohlenz, J. B., & Scott, N. H. (1963): *Patent US3284161 (A)*.

Qian, J. X., Chen, T. W., Enakonda, L. R., Da Liu, B., Basset, J.-M., & Zhou, L. (2020). Methane decomposition to pure hydrogen and carbon nano materials: State-of-the-art and future perspectives. *International Journal of Hydrogen Energy*, *45*, 15721–15743.

Rahimi, N., Kang, D., Gelinas, J., Menon, A., Gordon, M. J., Metiu, H., & McFarland, E. W. (2019). Solid carbon production and recovery from high temperature methane pyrolysis in bubble columns containing molten metals and molten salts. *Carbon*, *151*, 181–191.

Rahman, M. S., Croiset, E., & Hudgins, R. R. (2006). Catalytic decomposition of methane for hydrogen production. *Topics in Catalysis*, *37*, 137–145.

Rostrup-Nielsen, J. R. (1982). Sulfur poisoning. In J. L. Figueiredo (Ed.), *Progress in catalyst deactivation* (pp. 209–227). Dordrecht: Springer Netherlands.

Sánchez-Bastardo, N., Schlögl, R., & Ruland, H. (2020). Methane pyrolysis for CO_2-free H_2 production: A green process to overcome renewable energies unsteadiness. *Chemie Ingenieur Technik*, *92*, 1596–1609.

Schneider, S., Bajohr, S., Graf, F., & Kolb, T. (2020). State of the art of hydrogen production via pyrolysis of natural gas. *ChemBioEng Reviews*, *7*, 150–158.

Shah, N., Ma, S., Wang, Y., & Huffman, G. P. (2007). Semi-continuous hydrogen production from catalytic methane decomposition using a fluidized-bed reactor. *International Journal of Hydrogen Energy*, *32*, 3315–3319.

Snoeck, J.-W., Froment, G. F., & Fowles, M. (1997). Kinetic study of the carbon filament formation by methane cracking on a nickel catalyst. *Journal of Catalysis*, *169*, 250–262.

St. John, J. (2021). C-Zero raises $11.5M to scale up 'Turquoise Hydrogen' technology: Breakthrough Energy Ventures and Eni Next back the startup's plan to make low-cost, carbon-free hydrogen from natural gas. *Greentech Media,* 09.02.2021. https://www.greentechmedia.com/articles/read/c-zero-raises-11.5m-to-scale-up-turquoise-hydrogen-technology.

Steinberg, M. (1999). Fossil fuel decarbonization technology for mitigating global warming. *International Journal of Hydrogen Energy*, *24*, 771–777.

Suelves, I., Lazaro, M., Moliner, R., Corbella, B., & Palacios, J. (2005). Hydrogen production by thermo catalytic decomposition of methane on Ni-based catalysts: influence of operating conditions on catalyst deactivation and carbon characteristics. *International Journal of Hydrogen Energy*, *30*, 1555–1567.

Suelves, I., Pinilla, J. L., Lázaro, M. J., & Moliner, R. (2008). Carbonaceous materials as catalysts for decomposition of methane. *Chemical Engineering Journal*, *140*, 432–438.

Suelves, I., Pinilla, J. L., Lázaro, M. J., Moliner, R., & Palacios, J. M. (2009). Effects of reaction conditions on hydrogen production and carbon nanofiber properties generated by methane decomposition in a fixed bed reactor using a NiCuAl catalyst. *Journal of Power Sources*, *192*, 35–42.

Tao, X., Bai, M., Li, X., Long, H., Shang, S., Yin, Y., & Dai, X. (2011). CH_4–CO_2 reforming by plasma – challenges and opportunities. *Progress in Energy and Combustion Science*, *37*, 113–124.

Tardos, G., Mazzone, D., & Pfeffer, R. (1985a). Destabilization of fluidized beds due to agglomeration part I: Theoretical model. *The Canadian Journal of Chemical Engineering*, *63*, 377–383.

Tardos, G., Mazzone, D., & Pfeffer, R. (1985b). Destabilization of fluidized beds due to agglomeration part II: Experimental verification. *The Canadian Journal of Chemical Engineering*, *63*, 384–389.

Timmerberg, S., Kaltschmitt, M., & Finkbeiner, M. (2020). Hydrogen and hydrogen-derived fuels through methane decomposition of natural gas – GHG emissions and costs. *Energy Conversion and Management: X*, *7*, 100043.

TNO (n.d.). EMBER methane pyrolysis technology produces hydrogen without CO_2 emissions. https://www.tno.nl/en/focus-areas/energy-transition/roadmaps/towards-co2-neutral-industry/hydrogen-for-a-sustainable-energy-supply/optimising-production-hydrogen/ember-methane-pyrolysis/. Accessed 30.06.2021.

Tyrer, D. (1931): *Patent US 1,803,221*.

University of Central Florida (2004). *Thermocatalytic CO_2-free production of hydrogen from hydrocarbon fuels*. United States.

Upham, D. C., Agarwal, V., Khechfe, A., Snodgrass, Z. R., Gordon, M. J., Metiu, H., & McFarland, E. W. (2017). Catalytic molten metals for the direct conversion of methane to hydrogen and separable carbon. *Science*, *358*, 917–921.

Vander Wal, R., & Makiesse Nkiawete, M. (2020). Carbons as catalysts in thermo-catalytic hydrocarbon decomposition: A review. *C — Journal of Carbon Research*, *6*, 23.

Veselov, V., Levanyuk, T., Pilinenko, P., & Meshenko, N. (1977). *Scientific basics of hydrocarbon catalytic conversion*. Kiev: Naukova dumka.

Villacampa, J. I., Royo, C., Romeo, E., Montoya, J. A., Del Angel, P., & Monzón, A. (2003). Catalytic decomposition of methane over Ni-Al_2O_3 coprecipitated catalysts. *Applied Catalysis A: General*, *252*, 363–383.

Wang, B., & Xu, G. (2003). Conversion of methane to C_2 hydrocarbons via cold plasma reaction. *Journal of Natural Gas Chemistry*, *12*, 178–182.

Wang, M.-J., Gray, C. A., Reznek, S. A., Mahmud, K., & Kutsovsky, Y. (2003). Carbon black. In R. E. Kirk, & D. F. Othmer (Eds.), *Encyclopedia of chemical technology*. New York, NY: Wiley.

Ward, G. (2020). *Hazer commercial demonstration project investor presentation*.

Watanabe, F., Kaburaki, I., Shimoda, N., Igarashi, A., & Satokawa, S. (2017). Sulfur tolerance of noble metal catalysts for steam methane reforming. *Journal of the Japan Petroleum Institute*, *60*, 137–145.

Werther, J. (2000). Fluidized-bed reactors. In *Ullmann's encyclopedia of industrial chemistry*. Weinheim, Germany: Wiley-VCH Verlag GmbH & Co. KGaA.

Yang, H., Yan, R., Chen, H., Lee, D. H., & Zheng, C. (2007). Characteristics of hemicellulose, cellulose and lignin pyrolysis. *Fuel*, *86*, 1781–1788.

Zadeh, J. M., & Smith, K. J. (1998). Kinetics of CH_4 decomposition on supported cobalt catalysts. *Journal of Catalysis*, *176*, 115–124.

Zavarukhin, S. G., & Kuvshinov, G. G. (2004). The kinetic model of formation of nanofibrous carbon from CH_4–H_2 mixture over a high-loaded nickel catalyst with consideration for the catalyst deactivation. *Applied Catalysis A: General*, *272*, 219–227.

Zhang, T., & Amiridis, M. D. (1998). Hydrogen production via the direct cracking of methane over silica-supported nickel catalysts. *Applied Catalysis A: General*, *167*, 161–172.

Zhang, W., Ge, Q., & Xu, H. (2011). Influences of reaction conditions on methane decomposition over non-supported Ni catalyst. *Journal of Natural Gas Chemistry*, *20*, 339–344.

Zhang, Y., & Smith, K. (2005). A kinetic model of CH_4 decomposition and filamentous carbon formation on supported Co catalysts. *Journal of Catalysis*, *231*, 354–364.

Zherlitsyn, A. G., Medvedev, Y. V., Shiyan, V. P., Korolev, Y. D., & Franz, O. B. (2009): *Patent RU2393988 (C1)*.

Zherlitsyn, A. G., Shiyan, V. P., & Demchenko, P. V. (2016). Microwave plasma torch for processing hydrocarbon gases. *Resource-Efficient Technologies*, *2*, 11–14.

Zherlitsyn, A. G., Shiyan, V. P., & Kanaev, G. G. (2013): *Patent RU2522636 (C1)*.

Notation

Symbols

A	cross sectional area of reactor tube	m^2
a	cross sectional area of holes in distributor plate	m^2
Ar	Archimedes number	-
d	diameter of holes in distributor plate	m
d	diameter of particle	m
f	correction factor	-
g	gravity	m/s^2
H^0	enthalpy at standard conditions	kJ/mol
M	total mass of bed material	kg
M	molar mass	g/mol
m	mass	g
$\dot{m}$	mass flow rate	g/s
N	number of holes	-
n	amount of substance	mol
$\dot{n}$	molar flow rate	mol/s
p	pressure	Pa
$\dot{Q}$	heat flow	W
Re	Reynolds number	-
S	surface area	m^2
s	thickness of distributor plate	m
T	temperature	K *or* °C
t	time	s
U	gas velocity	m/s
V	volume	m^3
X	conversion rate	-
x	molar ratio	-
α	Heat transfer coefficient	$W/(m^2 \cdot K)$
Δ	difference	-
μ	dynamic viscosity	Pa·s
ξ	resistance coefficient	-
ρ	density	kg/m^3
ϕ	shape factor	-

Indices

0	regarding holes in distributor plate
0	downstream distributor plate
b	bed
cal	calibrated
D	upstream distributor plate
dry	dry base
fb	fluidised bed
g	gas
i	place holder for substance
in	at inlet to reactor
loss	lost during reaction
m	median
mf	minimum fluidisation
max	maximum
op	operation
out	outlet of reactor
P	regarding pressure
p	particle
prod	produced during reaction
R	reaction
rel	relative
S	surface equivalent
s	superficial
Sp	sphere
SV	volume/surface area equivalent
t	terminal
tot	total
V	volume equivalent
vap	vaporisation of water

Abbreviations

AC	activated carbon
NG	natural gas
TCD	thermo-catalytic decomposition

List of Tables

List of Figures

Annex

Carbon balance for fluidisation with additional H_2

The molar flow rates are:

$$\dot{n}_{tot,out} = \dot{n}_{CH_4,out} + \dot{n}_{H_2,out} = \dot{n}_{CH_4,out} + \dot{n}_{H_2,prod} + \dot{n}_{H_2,in} \tag{51}$$

$$\dot{n}_{tot,in} = \dot{n}_{CH_4,in} + \dot{n}_{H_2,in} = \dot{n}_{CH_4,out} + \frac{1}{2}\dot{n}_{H_2,prod} + \dot{n}_{H_2,in} \tag{52}$$

Dividing (52) by (51):

$$\frac{\dot{n}_{tot,in}}{\dot{n}_{tot,out}} = x_{CH_4,out} + \frac{1}{2} \cdot \frac{\dot{n}_{H_2,prod}}{\dot{n}_{tot,out}} + \frac{\dot{n}_{H_2,in}}{\dot{n}_{tot,out}} \tag{53}$$

From the definition of the molar ratio in (15), and (51) follows:

$$\dot{n}_{H_2,out} = \dot{n}_{tot,out} \cdot x_{H_2,out} = \dot{n}_{H_2,prod} + \dot{n}_{H_2,in} \tag{54}$$

$$\Rightarrow \quad \dot{n}_{H_2,prod} = \dot{n}_{tot,out} \cdot x_{H_2,out} - \dot{n}_{H_2,in} \tag{55}$$

Using (55) in (53) gives:

$$\frac{\dot{n}_{tot,in}}{\dot{n}_{tot,out}} = x_{CH_4,out} + \frac{1}{2}x_{H_2,out} - \frac{1}{2} \cdot \frac{\dot{n}_{H_2,in}}{\dot{n}_{tot,out}} + \frac{\dot{n}_{H_2,in}}{\dot{n}_{tot,out}} = x_{CH_4,out} + \frac{1}{2}x_{H_2,out} + \frac{1}{2} \cdot \frac{\dot{n}_{H_2,in}}{\dot{n}_{tot,out}} \tag{56}$$

$$\Rightarrow \quad \dot{n}_{tot,in} - \frac{1}{2}\dot{n}_{H_2,in} = \left(x_{CH_4,out} + \frac{1}{2}x_{H_2,out}\right) \cdot \dot{n}_{tot,out} \tag{57}$$

Considering (52) and extending (57) by $^{x_i}/_{x_i}$ leads to:

$$\dot{n}_{CH_4,in} + \frac{1}{2}\dot{n}_{H_2,in} = \left(x_{CH_4,out} + \frac{1}{2}x_{H_2,out}\right) \cdot \dot{n}_{tot,out} \cdot \frac{x_i}{x_i} \tag{58}$$

$$\Rightarrow \quad \dot{n}_{CH_4,in} + \frac{1}{2}\dot{n}_{H_2,in} = \left(x_{CH_4,out} + \frac{1}{2}x_{H_2,out}\right) \cdot \frac{\dot{n}_i}{x_i} \tag{59}$$

$$\Rightarrow \quad \frac{\dot{n}_{CH_4,in} + \frac{1}{2}\dot{n}_{H_2,in}}{x_{CH_4,out} + \frac{1}{2}x_{H_2,out}} \cdot x_i = \dot{n}_i \tag{60}$$

From (51) follows for $\dot{n}_{H_2,out}$:

$$\dot{n}_{H_2,out} = \dot{n}_{H_2,prod} + \dot{n}_{H_2,in} \tag{61}$$

Using (61) in (60) gives:

$$\dot{n}_{H_2,prod} = \frac{\dot{n}_{CH_4,in} + \frac{1}{2}\dot{n}_{H_2,in}}{x_{CH_4,out} + \frac{1}{2}x_{H_2,out}} \cdot x_{H_2,out} - \dot{n}_{H_2,in} \tag{62}$$

Integration of (62) over time:

$$n_{H_2,prod} = \left(\frac{\dot{n}_{CH_4,in} + \frac{1}{2}\dot{n}_{H_2,in}}{x_{CH_4,out} + \frac{1}{2}x_{H_2,out}} \cdot x_{H_2,out} - \dot{n}_{H_2,in} \right) \cdot \Delta t \tag{63}$$

The molar amount of carbon produced is thus:

$$n_C = \frac{1}{2} n_{H_2,prod} \tag{64}$$

Regeneration with CO_2

The chemical reaction is as follows:

$$CO_2 + C \rightarrow 2CO \tag{xx}$$

The molar flow rates are:

$$\dot{n}_{tot,out} = \dot{n}_{CO} + \dot{n}_{CO_2,out} \tag{65}$$

$$\dot{n}_{tot,in} = \dot{n}_{CO_2,in} = \frac{1}{2}\dot{n}_{CO} + \dot{n}_{CO_2,out} \tag{66}$$

Dividing (66) by (65):

$$\frac{\dot{n}_{CO_2,in}}{\dot{n}_{tot,out}} = \frac{1}{2}x_{CO} + x_{CO_2} \tag{67}$$

$$\Rightarrow \quad \dot{n}_{tot,out} = \frac{1}{\frac{1}{2}x_{CO} + x_{CO_2}} \cdot \dot{n}_{CO_2,in} \tag{68}$$

Dividing (65) by itself:

$$1 = x_{CO} + x_{CO_2} \tag{69}$$

The right side of (67) can thus be written as:

$$\frac{1}{2}x_{CO} + x_{CO_2} = 1 - \frac{1}{2}x_{CO} \tag{70}$$

Extending the left side of (68) with ${}^{x_i}/_{x_i}$:

$$\dot{n}_{tot,out} \cdot \frac{x_i}{x_i} = \dot{n}_{tot,out} \cdot \frac{\dot{n}_i}{\dot{n}_{tot,out}} \cdot \frac{1}{x_i} = \frac{\dot{n}_i}{x_i} \tag{71}$$

Using (71) and (70) in (68) gives:

$$\dot{n}_i = \frac{1}{1-\frac{1}{2}x_{CO}} \cdot x_i \cdot \dot{n}_{CO_2,in} \tag{72}$$

Integration over time:

$$n_i = \frac{1}{1-\frac{1}{2}x_{CO}} \cdot x_i \cdot \dot{n}_{CO_2,in} \cdot \Delta t \tag{73}$$

The amount of carbon used in the process is then:

$$n_C = \frac{1}{2} n_{CO} \tag{74}$$

H_2O regeneration

The chemical reaction is the following:

$$H_2O + C \rightarrow H_2 + CO \tag{xxi}$$

Water–gas shift reaction:

$$H_2O + CO \rightarrow H_2 + CO_2 \tag{xxii}$$

Total:

$$2H_2O + C \rightarrow 2H_2 + CO_2 \tag{xxiii}$$

The inlet gas is nitrogen which is saturated with water. Albeit the flow rate of nitrogen and inlet steam is known, it is not possible to estimate the amount of unconverted water.

The gas flow rates are the following:

$$\dot{n}_{tot,out,dry} = \dot{n}_{N_2} + \dot{n}_{CO} + \dot{n}_{CO_2} + \dot{n}_{H_2} \tag{75}$$

$$\dot{n}_{tot,in} = \dot{n}_{N_2} + \dot{n}_{H_2O} = \dot{n}_{N_2} + \dot{n}_{CO} + 2\dot{n}_{CO_2} + \dot{n}_{H_2} \tag{76}$$

Subtracting (76) from (75):

$$\dot{n}_{tot,in} = \dot{n}_{tot,out,dry} + \dot{n}_{CO_2} \tag{77}$$

Introducing the definition of the molar ratio for N_2 and CO_2:

$$x_{N_2} = \frac{\dot{n}_{N_2}}{\dot{n}_{tot,out,dry}} \quad \Rightarrow \quad \dot{n}_{tot,out,dry} = \frac{\dot{n}_{N_2}}{x_{N_2}} \tag{78}$$

$$x_{CO_2} = \frac{\dot{n}_{CO_2}}{\dot{n}_{tot,out,dry}} \quad \Rightarrow \quad \dot{n}_{CO_2} = x_{CO_2} \cdot \dot{n}_{tot,out,dry} = x_{CO_2} \cdot \frac{\dot{n}_{N_2}}{x_{N_2}} \tag{79}$$

Using (79) and (78) in (77):

$$\dot{n}_{tot,in} = \frac{\dot{n}_{N_2}}{x_{N_2}} + x_{CO_2} \cdot \frac{\dot{n}_{N_2}}{x_{N_2}} = \frac{\dot{n}_{N_2}}{x_{N_2}} \cdot \left(1 + x_{CO_2}\right) \tag{80}$$

Division of (76) by (75):

$$\frac{\dot{n}_{tot,in}}{\dot{n}_{tot,out,dry}} = x_{N_2} + x_{CO} + 2x_{CO_2} + x_{H_2} \tag{81}$$

$$\Rightarrow \quad \dot{n}_{tot,out,dry} = \frac{1}{x_{N_2} + x_{CO} + 2x_{CO_2} + x_{H_2}} \cdot \dot{n}_{tot,in} \tag{82}$$

Dividing (75) by itself:

$$1 = x_{N_2} + x_{CO} + x_{CO_2} + x_{H_2} \tag{83}$$

$$\Rightarrow \quad x_{N_2} = 1 - \left(x_{CO} + x_{CO_2} + x_{H_2}\right) \tag{84}$$

The right side of (81), using (84), can be rewritten as:

$$x_{N_2} + x_{CO} + 2x_{CO_2} + x_{H_2} = 1 + x_{CO_2} \tag{85}$$

Extending the left side of (82) with $^{x_i}/_{x_i}$ leads to:

$$\dot{n}_{tot,out,dry} \cdot \frac{x_i}{x_i} = \dot{n}_{tot,out,dry} \cdot \frac{\dot{n}_i}{\dot{n}_{tot,out,dry}} \cdot \frac{1}{x_i} = \frac{\dot{n}_i}{x_i} \tag{86}$$

Combination of (85) and (86), considering (82), gives:

$$\dot{n}_i = \frac{1}{1 + x_{CO_2}} \cdot x_i \cdot \dot{n}_{tot,in} = \frac{x_i}{x_{N_2}} \cdot \dot{n}_{N_2} \tag{87}$$

Integration over time leads to:

$$n_i = \frac{x_i}{1 - \left(x_{CO} + x_{CO_2} + x_{H_2}\right)} \cdot n_{N_2} \cdot \Delta t \tag{88}$$

Finally, the amount of carbon oxidised in this process is

$$n_C = n_{CO} + n_{CO_2} \tag{89}$$

Thermal decomposition of Limestone

The total flow rate of exhaust gas can be written as:

$$\dot{n}_{tot,out} = \dot{n}_{N_2} + \dot{n}_{CO_2} \tag{90}$$

Dividing (90) by itself returns:

$$1 = x_{N_2} + x_{CO_2} \tag{91}$$

Applying (15) gives:

$$\dot{n}_{tot,out} = \frac{\dot{n}_{N_2}}{x_{N_2}} = \frac{\dot{n}_{CO_2}}{x_{CO_2}} \tag{92}$$

Which can directly be rearranged to:

$$\dot{n}_{CO_2} = \frac{x_{CO_2}}{x_{N_2}} \cdot \dot{n}_{N_2} \tag{93}$$

Employing (91) and integration over time leads to:

$$n_{CO_2} = \frac{x_{CO_2}}{1 - x_{CO_2}} \cdot \dot{n}_{N_2} \cdot \Delta t \tag{94}$$

Reduction of Ilmenite

For each mole of produced water, the mass is reduced by the weight of one mole of oxygen. Consequently, the following formula is the base of this calculation:

$$n_O = n_{H_2O} \tag{95}$$

Gaseous water is condensed before the gas measurement unit, so the total dry off-gas stream is composed as:

$$\dot{n}_{tot,out,dry} = \dot{n}_{N_2} + \dot{n}_{H_2,out} \tag{96}$$

Only a part of the inlet hydrogen is converted to water. The gas stream from the perspective of hydrogen can therefore be written as:

$$\dot{n}_{H_2,in} = \dot{n}_{H_2O} + \dot{n}_{H_2,out} \tag{97}$$

Introducing the general definition for mole fractions:

$$x_i = \frac{\dot{n}_i}{\dot{n}_{tot}} \quad \Rightarrow \quad \dot{n}_{tot} = \frac{\dot{n}_i}{x_i} \tag{98}$$

Leads to:

$$\dot{n}_{tot,out,dry} = \frac{\dot{n}_{N_2}}{x_{N_2}} = \frac{\dot{n}_{H_2,out}}{x_{H_2,out}} \tag{99}$$

Rearranging (99) gives:

$$\dot{n}_{H_2,out} = \frac{x_{H_2,out}}{x_{N_2}} \cdot \dot{n}_{N_2} \tag{100}$$

Rearranging (97) and inserting (100) gives:

$$\dot{n}_{H_2O} = \dot{n}_{H_2,in} - \dot{n}_{H_2,out} = \dot{n}_{H_2,in} - \frac{x_{H_2,out}}{x_{N_2}} \cdot \dot{n}_{N_2} \tag{101}$$

Integration over time and considering (95) finally leads to:

$$n_O = \left(\dot{n}_{H_2,in} - \frac{x_{H_2,out}}{x_{N_2}} \cdot \dot{n}_{N_2} \right) \cdot \Delta t \tag{102}$$

Which can easily be converted to the loss in mass:

$$m_{loss} = m_O = n_O \cdot M_O \tag{103}$$